# Airborne DOAS Measurements over the South African Highveld

Stephen Paul Broccardo
9507287J

Supervisors:

**Prof. S. Piketh**
and
**Prof. C. Curtis**

A thesis submitted to the

**School of Geography, Archaeology and Environmental Studies**
**University of the Witwatersrand, Johannesburg**

in fulfillment of the requirements of the degree of Doctor of Philosophy

# Declaration

I declare that this thesis is my own unaided work, submitted in fulfillment of the requirements of the degree of Doctor of Philosophy in the School of Geography, Archaeology and Environmental Studies at the University of the Witwatersrand, Johannesburg. It has not been submitted previously for any degree or examination at any other university.

Stephen Paul Broccardo

____ day of _____ 2015

# Abstract

An imaging DOAS instrument, along with in situ trace-gas and aerosol instrumentation was deployed on board a research aircraft over the Highveld region of South Africa, to make regional-scale measurements of nitrogen dioxide ($NO_2$). The presence of a "hotspot" of $NO_2$ over the Highveld is confirmed. Case-study estimates of $NO_2$ emission flux were made downwind of a power station (10 tons.hr$^{-1}$), a petrochemical plant (36 tons.hr$^{-1}$) and the entire Highveld region (395 tons.hr$^{-1}$).

Vertical profile measurements were used to develop scenarios for a radiative transfer sensitivity study. From this, suitable air-mass factors for the DOAS measurements were determined. Comparisons between the airborne DOAS and satellite instruments show a good agreement where the spatial scales of the satellite ground pixels and the features in the two-dimensional trace-gas distribution are matched.

A long-term record of satellite data was analysed. Analysis of radiative transfer revealed a possible artefact in the adjacent positive and negative trends evident on the Highveld. A correction to the satellite record for a seasonal bias was made, and found to be important over biomass burning regions in Angola and Zambia.

Spatial features in a seasonal model of the satellite record are shown to correspond with known urban, industrial and biomass burning sources in the region. Signatures of soil emissions are also detected.

# Dedication

*To my family.*

# Preface

The Highveld region of South Africa has been identified from satellite measurements as a global "hotspot" of atmospheric nitrogen dioxide ($NO_2$). The Highveld is interesting since this area of high $NO_2$ is geographically isolated from any nearby anthropogenic sources, and transport of $NO_2$ from the Highveld has been shown to travel across the Indian Ocean and reach Australia. The present study was comissioned by Eskom, South Africa's state-owned electricity utility to further investigate this phenomenon.

Chapter 1 reviews some basic chemistry and physics, introduces some of the features of the Highveld study area, and describes the primary analytical technique employed by satellite instruments and the airborne instrument: differential optical absorption spectroscopy (DOAS). A review of the heritage of satellite instruments is given and some of the results that have come from their datasets.

A description of the techniques and instrumentation used for the aircraft measurements and analysis of the satellite datasets is given in Chapter 2. Chapter 3 discusses results from the aircraft measurements: vertical profiles measured by flying an ascending or descending spiral, and horizontal (geographical) distributions of $NO_2$ measured by the DOAS instrument.

Chapter 4 examines a 9-year record of measurements from the OMI satellite instrument over the Highveld and the sub-continent. Chapter 5 offers some conclusions.

Elements of this work have been published in the journal Atmospheric Chemistry and Physics by Heue *et al.* (2008*a*). It has also been presented at conferences: ASAAQ 2007 in Hong Kong, SASAS 2008 in Pretoria, IGAC 2008 in Annecy, IGARRS 2009 in Cape Town, AGU Fall Meeting 2010 in San Francisco and the Fifth DOAS Workshop held in Mainz in 2011.

Thanks should go first and foremost to my mother Louise and my late father Umberto for their unfailing support for my exploits (some crazier than others). My supervisors, Stuart Piketh for supporting this project and others

through thick and thin, and Christopher Curtis for stepping in at the eleventh hour. Klaus-Peter Heue (now at the German Aerospace Centre), David Walter (now at Max Planck Institute for Chemistry), Kristy Langerman (at Eskom Generation Environmental Management) and Christian Mayer (TU Dresden) for making our field campaigns possible. The pilots and crew at Orsmond Aviation without whom our flight campaigns wouldn't get off the ground, Steve Edwards (at the time from the South African Weather Service) for his dry but capable manner of keeping the magic smoke on the inside. Ulrich Platt from the Institut für Umweltphysik in Heidelberg for hosting my visit in 2008 and for supplying the iDOAS instrument. Alexander Kokhanovsky at Eumetsat and Andreas Richter at IUP Bremen for advice on radiative transfer modelling. Jeffrey Reid at the US Navy Research Laboratory in Monterey for friendship and pragmatism, and the loan of a PCASP instrument for one of the flight campaigns. Thierry Elias at LMD Paris for discussions about aerosol scattering and more. A special mention for Roelof Burger, for friendship, interesting chats, and assistance beyond the call of duty. Beyond the present work, others who have lent a hand or given a push over the years: the students of the Wits CRG, Sasha Smirnov at NASA Goddard Space Flight Center and Isabelle Ansorge at University of Cape Town.

# Contents

**Declaration** i

**Abstract** ii

**Dedication** iii

**Preface** iv

**Glossary** viii

**Acronyms** ix

**1 Introduction and Literature Survey** 1

1.1 Tropospheric $NO_x$ Chemistry . . . . . 3

1.1.1 Nitrogen oxides . . . . . 3

1.2 Features of the Atmosphere over the Highveld . . . . . 4

1.3 DOAS . . . . . 6

1.3.1 Air-mass Factor . . . . . 9

1.4 Radiative Transfer and Aerosol Scattering . . . . . 11

1.5 Satellite Instruments . . . . . 14

1.5.1 GOME . . . . . 14

1.5.2 SCIAMACHY . . . . . 17

1.5.3 OMI . . . . . 21

1.5.4 GOME-2 . . . . . 23
1.5.5 TROPOMI . . . . . 24
1.6 Applications of Satellite Trace-gas Measurements . . . . . 24
1.6.1 Top-down Emissions and Lifetime Estimates . . . . . 24
1.6.2 Long-term Trend Detection . . . . . 25
1.6.3 Intercontinental Transport . . . . . 26
1.6.4 Lightning and soil $NO_x$ detection . . . . . 27
1.7 Satellite Validation . . . . . 28
1.8 Airborne DOAS . . . . . 29

**2 Methods** **33**
2.1 Aircraft Measurements . . . . . 33
2.1.1 Position and state instrumentation . . . . . 33
2.1.2 In-situ measurements . . . . . 34
2.1.3 Airborne DOAS . . . . . 35
2.2 Radiative Transfer Modelling . . . . . 39
2.3 Satellite Data . . . . . 40
2.3.1 Level-2 Data . . . . . 40
2.3.2 Level-3 Data . . . . . 41

**3 Aircraft Measurements** **43**
3.1 Vertical Profiles . . . . . 44
3.2 Radiative Transfer Modelling . . . . . 54
3.3 Regional Mapping of $NO_2$ . . . . . 61
3.4 Satellite Comparisons . . . . . 67

**4 Satellite Climatology** **91**

**5 Conclusions** **123**

**A Table of Julian Days** **127**

# Glossary

**Albedo** The fraction of incoming radiation that is reflected by a surface.

**Aura** A NASA satellite which carries the OMI instrument as well as the High Resolution Dynamic Limb Sounder (HRDLS), the Tropospheric Emission Spectrometer (TES) and the Microwave Limb Sounder (MLS).

**Eskom** the South African state-owned electricity utility company.

**GEOS-CHEM** A global 3-d chemical transport model driven by meteorological fields from the NASA Goddard Earth Observing System.

**GOMECAT** A cloud retrieval algorithm from the GOME project.

**GOMETRAN** The radiative transfer model developed for the GOME project.

**Highveld** the high-lying plateau in the interior of South Africa, where Johannesburg is situated.

**Level 1b** Satellite products consisting of calibrated and geo-located spectral radiances.

**Level 2** Geophysical products derived from the satellite Level 1b data, at native spatial resolution and actual measurement times.

**Level 3** Daily geophysical satellite products, re-gridded onto a regular global grid.

**Sasol** a South African petrochemicals company.

**SCIATRAN** The radiative transfer model developed for the SCIAMACHY project.

**SLIMCAT** An off-line 3-d chemical transport model.

# Acronyms

**AERONET** Aerosol Robotic Network.

**AMAXDOAS** Airborne Multi-Axis DOAS.

**AMF** Air-Mass Factor.

**AMSL** above mean sea level.

**AOD** Aerosol optical depth.

**AOT** Aerosol optical thickness.

**CARIBIC** Civil Aircraft for the Regular Investigation of the atmosphere Based on an Instrument Container.

**CCD** Charge-Coupled Device.

**DJF** December, January, February.

**DOAS** Differential Optical Absorption Spectrometry.

**DOMINO** Derivation of OMI tropospheric $NO_2$.

**ECD** Emission Control Device.

**ECMWF** European Centre for Medium-Range Weather Forecasting.

**EDGAR** Emission Database for Global Atmospheric Research.

**EEF** extinction efficiency factor.

**ENVISAT** Environmental Satellite.

**ERS-2** second European Remote Sensing.

**ESA** European Space Agency.

**FLEXPART** Flexible Particle dispersion model.

**FRESCO** Fast Retrieval Scheme for Clouds from the Oxygen A-Band.

**FSSP** Forward-Scattering Spectrometer Probe.

**GEIA** Global Emission Inventory Activity.

**GOME** Global Ozone Monitoring Experiment.

**GOME-2** Global Ozone Monitoring Experiment 2.

**GPS** Global Positioning System.

**HALOE** Halogen Occultation Experiment.

**iDOAS** Imaging DOAS.

**IFOV** instantaneous field-of-view.

**JJA** June, July, August.

**LIS** Lightning Imaging Sensor.

**MAM** March, April, May.

**MAXDOAS** Multi-Axis DOAS.

**Metop-A** Meteorological Operational Satellite.

**MODIS** Moderate Resolution Imaging Spectroradiometer.

**MOZART-2** Model for Ozone And Related chemical Tracers.

**NASA** National Aeronautics and Space Administration.

**NCEP** National Centers for Environmental Prediction.

**OMI** Ozone Monitoring Instrument.

**PBL** Planetary Boundary Layer.

**PC** Personal Computer.

**PCASP** Passive-Cavity Aerosol Spectrometer Probe.

**ROI** region of interest.

**RTE** Radiative Transfer Equation.

**RTM** Radiative Transfer Model.

**SAFARI-92** South African Fire-Atmosphere Research Initiative.

**SAWS** South African Weather Service.

**SCD** Slant Column Density.

**SCIAMACHY** SCanning Imaging Absorption spectroMeter for Atmospheric CHartographY.

**SON** September, October, November.

**SQL** Structured Query Language.

**SZA** Solar Zenith Angle.

**TEMIS** Tropospheric Emission Monitoring Internet Service.

**TOMS** Total Ozone Mapping Spectrometer.

**TRMM** Tropical Rainfall Monitoring Mission.

**TROPOMI** Tropospheric Ozone Monitoring Instrument.

**VCD** Vertical Column Density.

**VMR** volume mixing ratio.

# Chapter 1

# Introduction and Literature Survey

The Highveld region of South Africa is a high-altitude plateau in the interior of the country (Figure 1). The region is home to the Johannesburg–Pretoria conurbation and the adjoining industrial towns of Ekuruleni to the east and Vanderbijlpark and Vereeniging to the south. The latter two towns, along with Sasolburg enclose the area known as the Vaal Triangle. Sasolburg is named after the petrochemicals company which owns the refinery in that town. The Vaal Triangle is also home to a steelmill (including two blast furnaces, three 170 ton basic oxygen furnaces and three 155 ton arc furnaces), and a nearby coal-fired power station of 3700 MW generating capacity.

To the east of Johannesburg, Sasol also operates a coal-to-fuel (Fisher-Tropsch process) synfuel refinery in Secunda, a facility which also generates its own electricity from coal. Secunda is situated in a region often referred to as the Eastern Highveld or the Mpumalanga Highveld. The Eastern Highveld is also home to eleven more coal-fired power stations operated by Eskom, South Africa's government-owned electricity utility, with further total generating capacity of 29700 MW. The Eastern Highveld is also home to several steelmills. In between the industries described are coal mines to supply the fuel, a small town about every hundred kilometers, and mostly farmland or grassland. A larger scale map of the Highveld is shown in Figure 1.7 on page 15. Eskom's thirteenth coal-fired power station (4080 MW capacity) is adjacent to the town of Lephalale, to the north of Johannesburg. Surrounding Lephalale is grassland in all directions for several hundred kilometres.

Satellite observations highlight the Highveld as a region with a higher than expected concentration of $NO_2$ (Martin *et al.* 2002, Toenges-Schuller *et al.* 2006), and with an increasing trend of $NO_2$ (Richter *et al.* 2005, van der A *et al.* 2008). Analysis of a year of ground-based monitoring station data (Collett *et al.* 2010) indicates that most of this $NO_2$ is from tall-stack in-

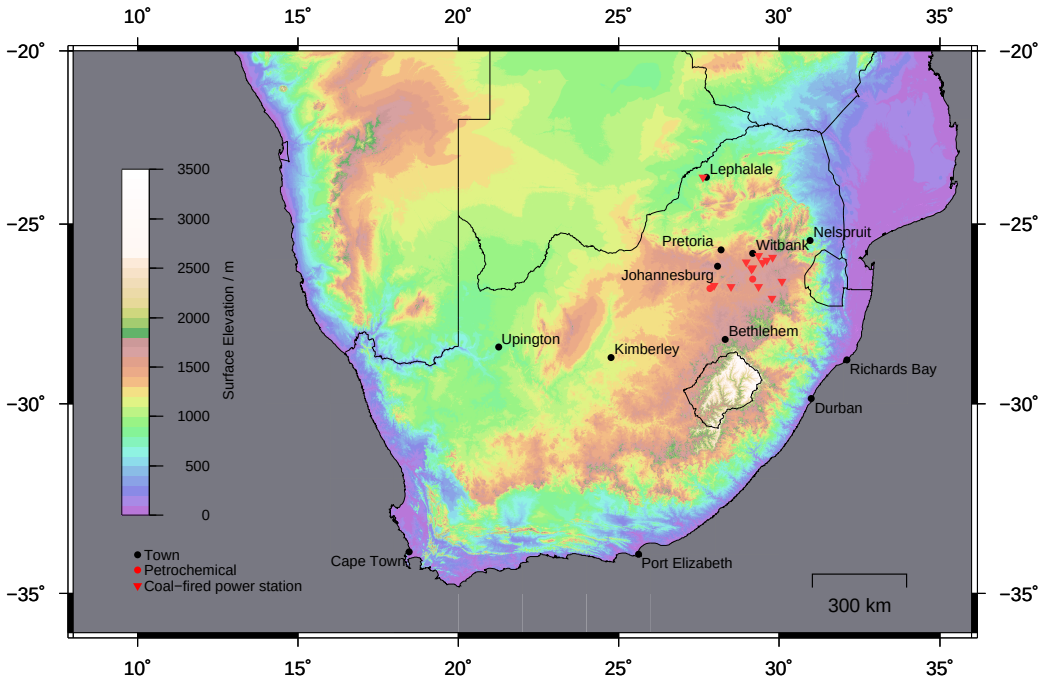


Figure 1.1: A topographic map of South Africa with some major towns indicated

dustrial emissions. An analysis of satellite and ground-based measurements indicates that the urban conurbation of greater Johannesburg is also a significant source (Lourens *et al.* 2012).

The present study was commissioned to make a closer investigation of the Highveld $NO_2$ "hotspot". The following research questions are investigated:

1. Can source apportionment be done on a regional scale using high-resolution measurements of $NO_2$ vertical column densitites?

2. Can plume observations by airborne Differential Optical Absorption Spectrometry (DOAS) be used to determine emission fluxes and reaction rates?

3. Are satellite measurements of $NO_2$ over the Highveld subject to systematic biases, and what are the likely sources of such biases?

4. What features can be identified in the satellite record, associated with known sources of $NO_2$?

## 1.1 Tropospheric $NO_x$ Chemistry

### 1.1.1 Nitrogen oxides

Nitrogen oxides and their interactions with ozone and other atmospheric species play a fundamental role in tropospheric chemistry (Seinfeld and Pandis 2006). Photolysis of $NO_2$ results in the formation of ozone by the following reactions:

$$NO_2 + h\nu \rightarrow NO + O \tag{1.1}$$

$$O + O_2 + M \rightarrow O_3 + M \tag{1.2}$$

where $h\nu$ represents a photon (of wavelength less than 424 nanometres, to ensure that it has sufficient energy). Ozone reacts with NO to re-generate $NO_2$:

$$O_3 + NO \rightarrow NO_2 + O_2 \tag{1.3}$$

Reactions 1.1, 1.2 and 1.3 define a photochemical stationary state, where the ratio of NO to $NO_2$ is constant. This ratio is called the Leighton ratio (Seinfeld and Pandis 2006):

$$L = \frac{[NO]}{[NO_2]} = \frac{J_{NO_2}}{k_{1.3}[O_3]} \tag{1.4}$$

where $k_{1.3}$ is the reaction constant of reaction 1.3, and $J_{NO_2}$ is the photolysis frequency of $NO_2$. Since the reactions 1.1, 1.2 and 1.3 are very fast, the two species NO and $NO_2$ are often referred to as $NO_x$.

Removal of $NO_x$ from the atmosphere occurs by conversion to $HNO_3$. During the day $NO_2$ reacts with $OH$ to form $HNO_3$ (Seinfeld and Pandis 2006):

$$NO_2 + OH + M \rightarrow HNO_3 + M \tag{1.5}$$

At night $NO_3$ is formed by reaction of $NO_2$ and $O_3$, which forms $N_2O_5$ on reaction with another $NO_2$ molecule. During the day $NO_3$ rapidly photodissociates, hence these reactions are predominant at night:

$$NO_2 + O_3 \rightarrow NO_3 + O_2 \tag{1.6}$$

$$NO_3 + NO_2 + M \rightleftharpoons N_2O_5 + M \tag{1.7}$$

with the equilibrium in reaction 1.7 shifting further to the right as temperature decreases.

$N_2O_5$ reacts heterogeneously on aerosols or water droplets to form $HNO_3$ which is removed by wet or dry deposition (Seinfeld and Pandis 2006):

$$N_2O_5 + H_2O \rightarrow 2HNO_3 \tag{1.8}$$

$NO_x$ instrumentation used in the present study is equipped with a molybenum catalyst. The purpose of this catalyst is purportedly to convert $NO_2$ to NO, the latter being the species that the instrument measures by chemiluminescence. However, this is not the case; in order to achieve selective conversion a photolytic converter is needed (Hains *et al.* 2010, Schaub *et al.* 2007, Schumann 2012). The molybednum catalyst will convert most reactive nitrogen, commonly called $NO_y$, which includes nitric acid, nitrous acid, peroxyacetyl nitrate, nitrate radicals, dinitrogen pentoxide, and alykl nitrates (Seinfeld and Pandis 2006), hence the measurement reported by the instrument is not a true $NO_2$ concentration.

## 1.2 Features of the Atmosphere over the Highveld

The atmosphere above the southern African sub-continent forms part of the decending arm of the Hadley circulation. Subsidence of air within this global-scale circulation system leads to temperature inversions or layers of absolute stability. Analysis of radiosonde data has identified absolutely stable layers over the whole sub-continent around 850, 700, 500, and 300 hPa, illustrated in Figure 1.2. They occur on about 50 percent of days throughout the year and about 80 percent of days in the winter (Cosijn and Tyson 1996, Swap and Tyson 1999). These layers control vertical transport of aerosols and trace gases through their presence or absence, and as such exert a large influence over the vertical distribution of these species (Campbell 2003).

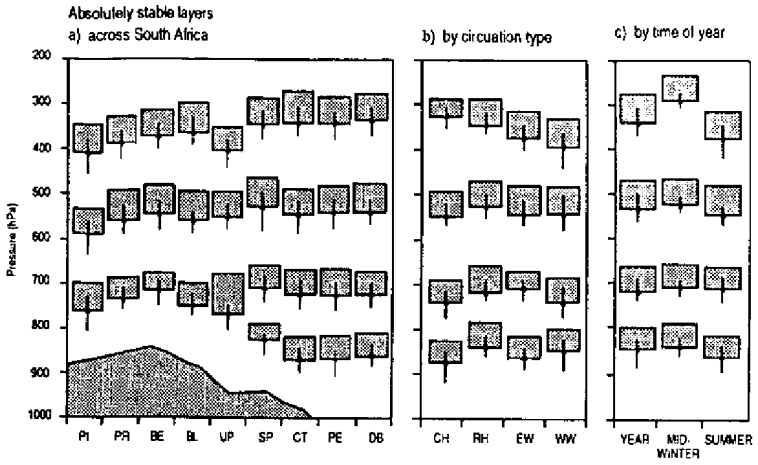


Figure 1.2: Position and depth of absolutely stable layers in the atmosphere over the Southern African sub-continent. They are classified by position in the left-hand sub-figure: PI Pietersburg (Polokwane), PR Pretoria, BE Bethlehem, BL Bloemfontein, UP Upington, SP Springbok, CT Cape Town, PE Port Elisabeth, DB Durban. In the centre figure they are classified by synoptic circulation type: CH Continental High, RH Ridging High, EW Easterly Wave, WW Westerly Wave. In they right-hand sub-figure, they are classified by season (after Cosijn and Tyson (1996).)

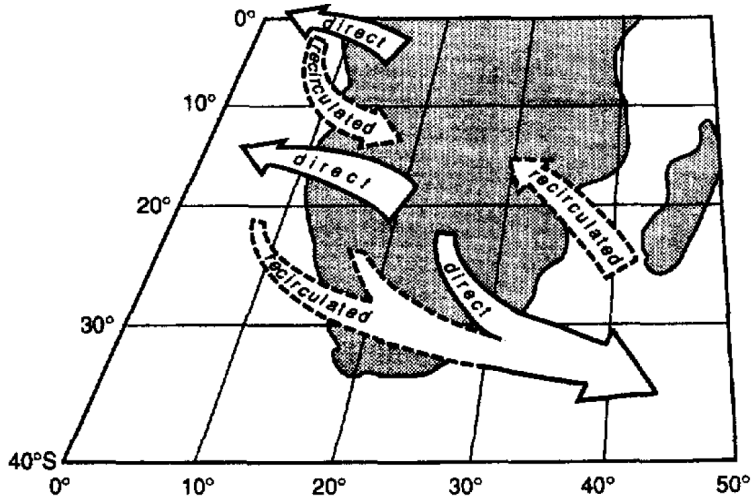


Figure 1.3: A conceptual view of outflow and recirculation of air from the southern African sub-continent, after Tyson and DAbreton (1998).

Tyson *et al.* (1996) generalise the work of Garstang *et al.* (1996), which was focussed on the South African Fire-Atmosphere Research Initiative (SAFARI-92) field campaign, and classifies circulation types based on synoptic charts at 850 hPa and 500 hPa for a period of five years. Periods of unchanging synoptic conditions are identified and trajectories analysed over ten-day periods. Large-scale recirculation of air is found to occur over the sub-continent. Two major transport paths leaving the sub-continent are identified: a plume travelling to the west over Angola, and a plume travelling to the east over Kwazulu-Natal (Figure 1.3). The Kwazulu-Natal plume is found to be the predominant transport pathway based on frequency of occurence. Observational evidence of re-circulation is presented by Piketh *et al.* (2002), based on aerosol samples collected at Mt. Ben McDhui in the Eastern Cape.

## 1.3 DOAS

Differential Optical Absorption Spectrometry (DOAS) is a remote sensing technique based on light absorption in the ultraviolet to visible wavelength range (Platt and Stutz 2008). DOAS has also been applied to near-infrared measurements (Buchwitz *et al.* 2000). The technique takes advantage of fine-scale absorption structures of specific molecules to measure integrated concentration along a light path. The absorption is related to concentration using the Beer-Lambert-Bougier law:

$$I(\lambda) = I_0(\lambda) \exp(-L\sigma(\lambda)c) \tag{1.9}$$

where $I(\lambda)$ is the observed light intensity as a function of wavelength, after the light has passed through a layer of thickness $L$ and $I_0(\lambda)$ is the initial intensity emitted by the radiation source. The concentration of the species being measured is denoted by $c$, and $\sigma(\lambda)$ is the absorption cross-section of the species as a function of wavelength $\lambda$.

Optical density is defined to be:

$$\tau(\lambda) = \ln\left(\frac{I_0(\lambda)}{I(\lambda)}\right) = \sigma(\lambda)cL \tag{1.10}$$

Equation 1.9 is an oversimplification of the processes that take place in atmospheric absorption of a light beam. Other processes taking place in the real atmosphere that will have an influence on the DOAS retrieval (Platt and Stutz 2008) are:

1. Raleigh scattering: this is not an absorption process, but rather the scattering of light by air molecules; however for the purposes of a DOAS retrieval it is treated as an absorption. The pseudo-absorption cross-section is written as

   $$\sigma_R(\lambda) \approx \sigma_{R0}\lambda^{-4} \tag{1.11}$$

   where $\sigma_{R0} \approx 4.4 \times 10^{-16} cm^2 nm^4$ for air.

   The Raleigh extinction coefficient is given by

   $$\epsilon_R(\lambda) = \sigma_R(\lambda)c_{air} \tag{1.12}$$

   where $c_{air}$ is the concentration of air molecules ($2.4 \times 10^{19} cm^{-1}$ at $20^\circ$ and 1 atmosphere).

2. Mie scattering: this is scattering of light by aerosol particles. Similarly to Raleigh scattering this is treated as an absorption with the extinction coefficient:

   $$\epsilon_M(\lambda) = \epsilon_{M0}\lambda^{-n} \tag{1.13}$$

   where $n$ is between 1 and 4.

3. Ring effect:

   This is inelastic Raman scattering that manifests as a filling in of solar Fraunhofer lines. The effect is named after the discoverer (Grainger and Ring 1962). It is treated as a pseudo-absorption in the DOAS retrieval (Vountas *et al.* 1998).

Accounting for Raleigh and Mie extinction coefficients in equation 1.9 gives a more accurate model of absorption:

$$I(\lambda) = I_0(\lambda) \exp(-L(\sigma(\lambda)c + \epsilon_R(\lambda) + \epsilon_M(\lambda))) \tag{1.14}$$

Since the atmosphere has multiple trace gases absorbing at various wavelengths, we need to extend equation 1.14 to account for these; also considering the length of the light path:

$$I(\lambda, L) = I_0(\lambda) \exp\left( - \int_0^L \Big[ \sum_i \sigma_i(\lambda) c_i(l) + \epsilon_R(\lambda, l) + \epsilon_M(\lambda, l) \Big] dl \right) \tag{1.15}$$

where $\sigma_i(\lambda)$ and $c_i(l)$ are the absorption cross section and concentration of the $i$th trace gas. The optical density is now written as:

$$\tau = \ln\Big(\frac{I_0(\lambda)}{I(\lambda)}\Big) = \sigma(\lambda) \int_0^L c(l) dl \tag{1.16}$$

and the quantity

$$S = \int_0^L c(l) dl \tag{1.17}$$

is defined as the Slant Column Density (SCD).

In the real atmosphere the total absorption is difficult to model, and the original intensity $I_0$ is therefore unknown. For this reason, only fine-scale absorption structures are used for the DOAS retrieval. This is illustrated in Figure 1.4. The fine-scale (differential) absorption that the DOAS retrieval uses to determine the concentration is shown as $\tau'$. The total absorption $\tau_{total}$ is unknown.

In practice the DOAS retrieval is implemented using a Levenberg-Marquhard non-linear least squares fitting algorithm (Kraus 2006). The retrieval

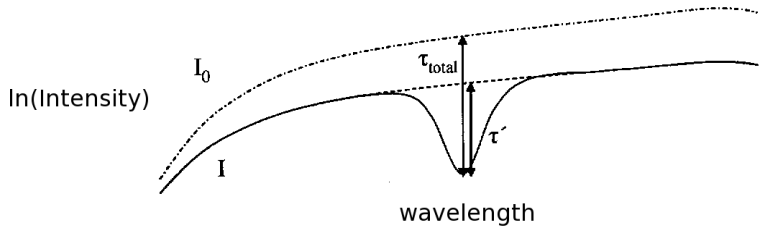


Figure 1.4: The difference between the original intensity $I_0$ and the measured intensity $I$ is unknown. The DOAS retrieval uses the fine-scale differential absorption $\tau'$ to determine the slant column density (after Heue (2005)).

calculates the slant column density, which is dependent on the light path through the atmosphere. In order to convert this to the more useful vertical column density, an Air-Mass Factor (AMF) needs to be determined. This is discussed further in Section 1.3.1.

### 1.3.1 Air-mass Factor

The DOAS retrieval results in a slant column, defined above. The slant columns are usually converted to Vertical Column Density (VCD), which are defined:

$$V = \int_0^z c(z)dz \tag{1.18}$$

and are more useful quantities to interpret. In order to perform this conversion, the Air-Mass Factor (AMF) is introduced:

$$A = S/V \tag{1.19}$$

Simplistically, the AMF is found to depend on Solar Zenith Angle (SZA), the angle between the sun and the zenith measured in the azimuthal plane; viewing angle, the angle at which the instrument optics are pointed, which may be defined relative to the vertical or horizontal; and the relative azimuth angle, the angle between the azimuthal planes of the instrument and the sun. SZA is illustrated in Figure 1.5.

Referring to Figure 1.5, air-mass factor clearly will depend on the ratio of L to Z, the length of the light path through a trace-gas layer to the thickness of the layer. Geometrically, this ratio is $cos(SZA)$. The length of the light path is also influenced by scattering events, surface albedo, and the vertical

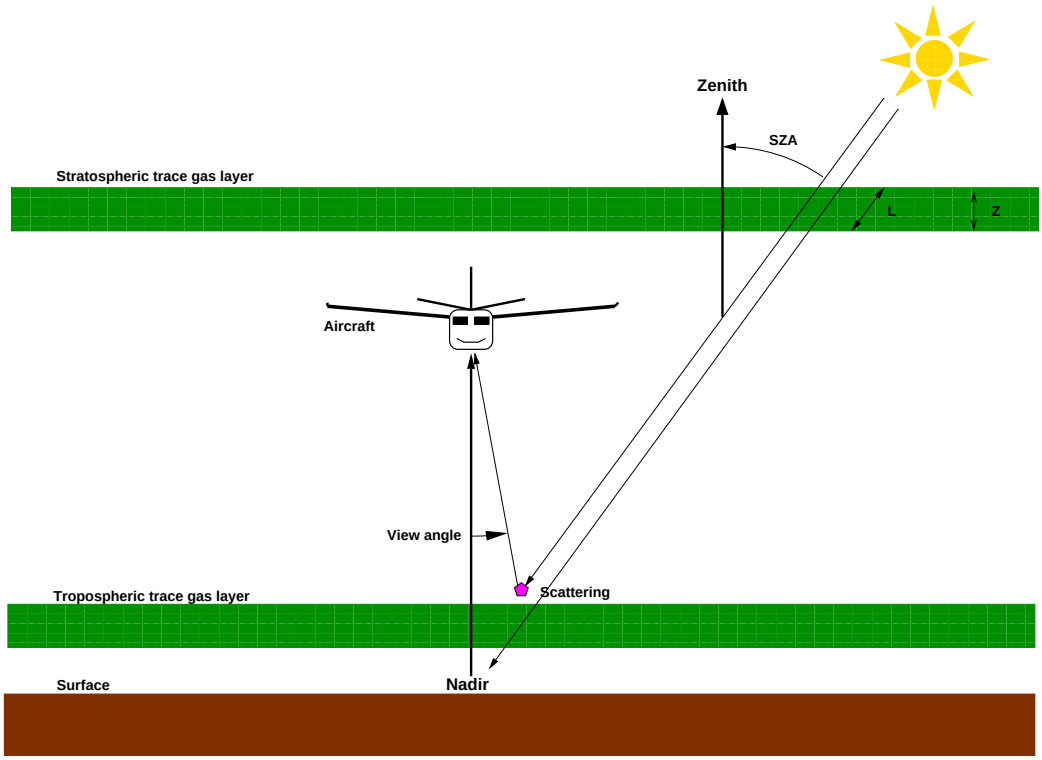


Figure 1.5: The definition of solar zenith angle and viewing angle in the context of an aircraft platform are illustrated. The nadir point is the point on the ground directly beneath the aircraft, similarly the nadir direction is looking straight down from the aircraft. The zenith is the normal to the earth's surface (after Dix (2007))

profile of the absorber. This influence is calculated using a Radiative Transfer Model (RTM).

The influence of aerosol vertical profile and optical thickness on the air-mass factor is examined through a comprehensive sensitivity study presented by Leitao *et al.* (2010). The main factors influencing the air-mass factor were found to be the relative positions of the trace-gas and the aerosols in the vertical column, the single-scattering albedo, the optical depth of the aerosol layer, and the surface Albedo.

## 1.4 Radiative Transfer and Aerosol Scattering

The science of radiative transfer studies the propagation of radiant energy (light) through a medium such as the atmosphere. Some of the processes which influence this propagation are:

1. absorption
2. scattering, discussed below
3. emission

The Radiative Transfer Equation (RTE) describes the relationship between radiance (also called intensity of radiation) and these three processes. In the UV-visible range of wavelengths, emission may be ignored and the RTE is (Dix 2007):

$$\frac{dI(\lambda)}{dl} = \underbrace{-I(\lambda)\cdot[\epsilon_a(\lambda)+\epsilon_s(\lambda)]}_{1} + \underbrace{\epsilon_s(\lambda)\int_0^{\pi}\int_0^{2\pi} I(\lambda,\theta,\phi)\cdot\frac{P(\theta,\phi)}{4\pi}\mathrm{d}\phi\cdot sin(\theta)\mathrm{d}\theta}_{2} \tag{1.20}$$

where $I_\lambda$ is the radiance as a function of wavelength, $l$ is distance along a light path, $\epsilon_a(\lambda)$ is absorption cross-section, $\epsilon_s(\lambda)$ is scattering cross section; so part 1 of the equation describes radiation scattered or absorbed out of the beam. Part 2 of the equation describes light that is scattered into the direction of propagation of the beam, where $P(\theta,\phi)$ is a dimensionless scattering parameter.

Radiative transfer affects the path taken through the atmosphere by photons measured by the DOAS instrument, and hence the sensitivity of the measurement to absorbers at various positions in the atmosphere. The radiative transfer equation is solved using a radiative transfer model, in the present work SCIATRAN (Rozanov *et al.* 2005) is used.

Elastic scattering leads to a change of direction of the photon, and can take place through the interaction of a photon with a scattering centre such as a molecule (Raleigh scattering), or an aerosol particle (Mie scattering). The aerosol loading in the atmosphere is often expressed as Aerosol optical thickness (AOT) or Aerosol optical depth (AOD), which is a quantity that can be measured by space- and ground-based remote sensing instruments. By analogy to absorption by trace gases, AOT is expressed as:

$$AOT = \ln\left(\frac{I_0(\lambda)}{I(\lambda)}\right) = \int_0^\infty \beta(z)\mathrm{d}z \tag{1.21}$$

where $\beta(z)$, the aerosol extinction coefficient, is the sum of scattering and absorption. The extinction coefficient is related to the aerosol characteristics by (Sayer *et al.* 2012):

$$\beta_\lambda = \int_0^\infty \pi r^2 Q_{ext}(r, \lambda, m) N(r)\mathrm{d}r \tag{1.22}$$

where $r$ is the aerosol particle radius, $N(r)$ is the number of aerosols of a given size, and $Q_{ext}(r, \lambda, m)$ is the extinction efficiency factor (EEF), a function of particle size, wavelength, and particle refractive index.

The direction of the photon after the scattering event is described as a probability distribution: the scattering phase function (Thomas and Stamnes 1999). Scattering phase function depends on the shape, size, and optical properties of the scattering centre. Some examples of scattering phase functions are shown in Figure 1.6.

The scattering phase function is sometimes conveniently modelled by an empirical analytical function, such as the one-parameter Henyey-Greenstein phase function:

$$P(cos\Theta)) = \frac{1 - g^2}{(1 + g^2 - 2 \cdot g \cdot cos\Theta)^{\frac{3}{2}}} \tag{1.23}$$

where $\Theta$ is the scattering angle and $g$ the asymmetry parameter.

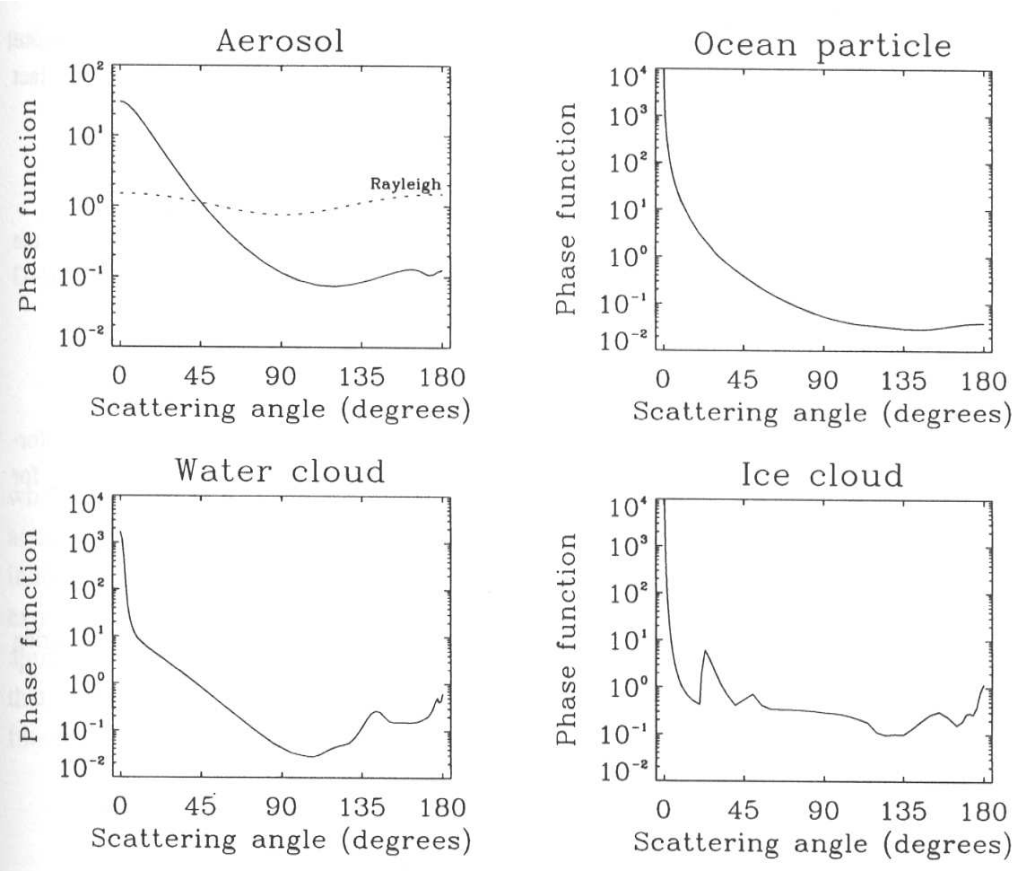


Figure 1.6: Some examples of scattering phase functions (after Thomas and Stamnes (1999)).

## 1.5 Satellite Instruments

$NO_2$ in the earth's atmosphere is measured from satellites by means of a DOAS retrieval on measurements of backscattered solar radiation. The retrieval of tropospheric vertical column amounts is typically done in stages: a spectral fit to determine the slant column amount, the subtraction of the stratospheric component from the total column, and a radiative transfer calculation to determine the influence of the light path through the atmosphere.

The first and last steps of the retrieval are described in Sections 1.3 and 1.3.1 above. The stratospheric component is derived either from satellite measurements in areas where the tropospheric column is known to be small (i.e. over remote ocean areas, relying on the zonal invariance of stratospheric $NO_2$ concentrations), or from a global chemistry-transport model.

Satellite measurements of tropospheric $NO_2$ using a DOAS retrieval date back to the GOME instrument on the ERS-2 satellite. Since then SCanning Imaging Absorption spectroMeter for Atmospheric CHartographY (SCIAMACHY), Ozone Monitoring Instrument (OMI), and Global Ozone Monitoring Experiment 2 (GOME-2) have continued the measurements, with each generation of satellite instrument bringing improvements in spatial resolution or spectral range (Martin 2008). There is a growing sophistication in the treatment of the errors arising during the retrieval procedure. These improvements, as well as improvements in spatial resolution depicted in Figure 1.7, make the measurements of increasing relevance to investigations of air quality. Future sensors with higher spatial resolution such as Tropospheric Ozone Monitoring Instrument (TROPOMI), due for launch in 2016 (Veefkind *et al.* 2012), and geostationary sensors will continue this trend.

### 1.5.1 GOME

The Global Ozone Monitoring Experiment (GOME) was launched in April 1995 on the second European Remote Sensing (ERS-2) satellite. The ERS-2 satellite orbit parameters are summarised in Table 1.1 on page 18.

GOME is a passive spectrometer measuring in the wavelength range of 237 – 794 nm, with a spectral resolution between 0.2 and 0.33 nm. On-board spectral calibration is done using a Pt-Ne-Cr discharge lamp (Burrows *et al.* 2000). The instrument includes a diffuser plate to make a daily direct measurement of solar irradiance; however it is found that this introduces a structure in the residual which changes according to the angle of incidence

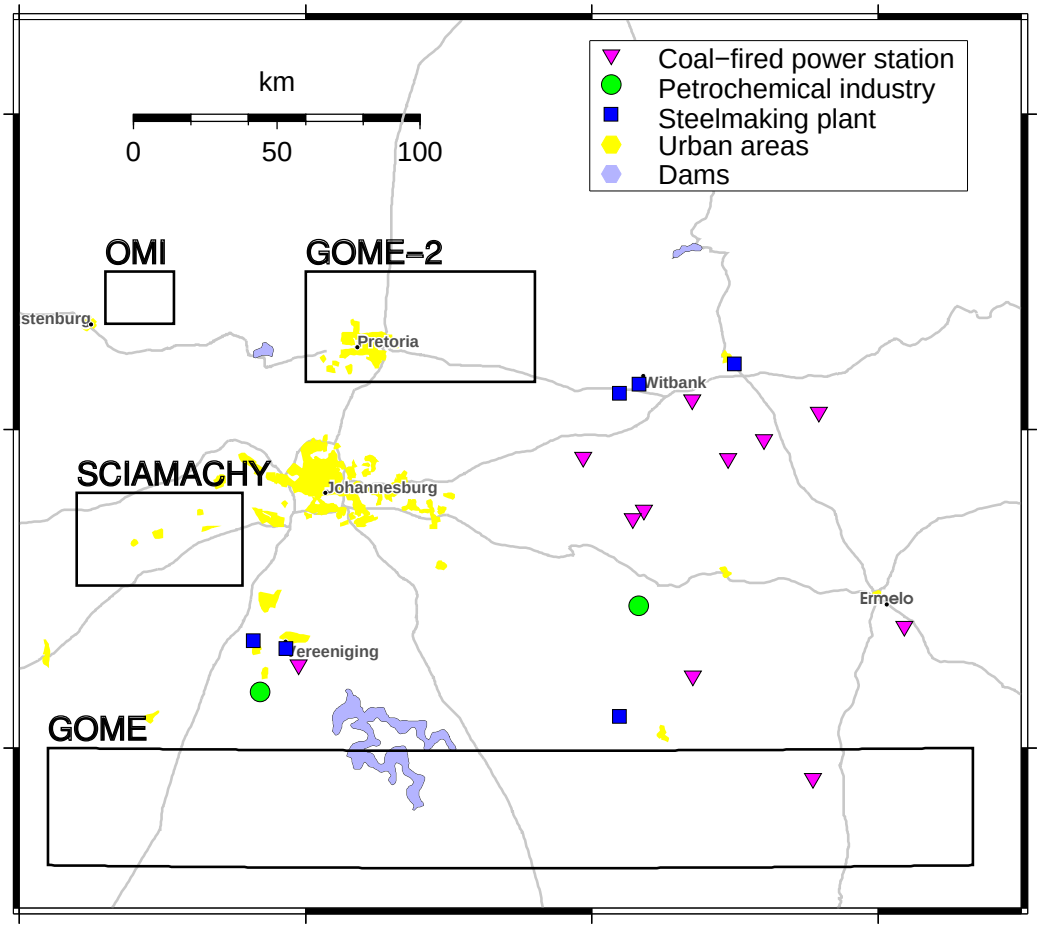


Figure 1.7: A comparison of the nadir ground-pixel sizes of the satellite remote-sensing instruments used for tropospheric trace-gas measurements. The pixels are overlaid on a map of the Highveld.

of the solar radiation on the diffuser plate, and hence according to the time of year.

The nadir pixel size of GOME is 320 km by 40 km; this is illustrated along with the other satellite nadir pixel sizes in Figure 1.7 on page 15. Global measurements were made until 2003, when the tape recorder on the satellite failed (Martin 2008).

Tropospheric $NO_2$ retrievals from GOME measurements are presented by several investigators. The four-step procedure used by Richter and Burrows (2002) is typical of global satellite retrievals: 1) Retrieve the $NO_2$ slant column using a DOAS fit between 425 – 450 nm, 2) Estimate the stratospheric contribution from a measurement over the Pacific Ocean at the same latitude, 3) Subtract the stratospheric contribution from the slant column to derive a tropospheric slant column, 4) Convert the tropospheric slant column to a vertical column, using an air-mass factor that is calculated using a RTM, based on a modelled atmosphere.

Uncertainties arise in all of the steps described. Systematic errors in the DOAS retrieval are small compared to other sources, on the order of $1 \times 10^{15}$ molecules.cm$^{-2}$. A larger error might arise from the temperature dependance of the $NO_2$ absorption cross-section. Richter and Burrows (2002) use a cross-section measured at 241 K (appropriate for the stratosphere); however temperatures in the boundary layer are much higher. This leads to approximately a twenty percent underestimation of the tropospheric $NO_2$ column. The diffuser-plate problem is tackled by choosing one extraterrestrial solar spectrum for all spectral fits.

The stratospheric contribution to the total column is assumed to be zonally invariant. This is valid at low latitudes, however in winter and spring there are large zonal gradients in stratospheric $NO_2$ in the polar regions. Errors are estimated to be on the order of $1 \times 10^{15}$ molecules.cm$^{-2}$. Step three is justified, since the ERS-2 satellite is in a sun-synchronous orbit, and a given latitude is always measured at the same local time, and hence at the same solar zenith angle. It is therefore possible to subtract the stratospheric contribution to the total column without using an AMF.

The tropospheric AMF is calculated using the GOMETRAN radiative transfer model, assuming a uniform model atmosphere with clear skies, a surface albedo of 0.05, a maritime aerosol model, and a constant mixing ratio of $NO_2$ in the lowest 1.5km of the atmosphere. Cloud screening is done based on the GOME operational cloud data product, pixels with a cloud fraction greater than 0.1 are rejected. Determination of the AMF is the largest uncertainty in

calculating the tropospheric $NO_2$ column. A change in surface albedo from 0.02 to 0.08 can lead to a change in AMF of fourty percent. The position within the atmospheric column, and single-scattering albedo of aerosols also have a large influence on the air-mass factor. Clouds within the pixel will introduce even larger errors. The large ground pixel size of GOME means that there may be significant variation in cloud cover within a pixel, even when the cloud cover is below the threshold value of 0.1. An approximate correction for cloud cover is performed using an intensity-weighting approach.

Martin *et al.* (2002) present a more sophisticated analysis, addressing some of the error sources described above. An $NO_2$ absorption spectrum measured at 293 K, which is more appropriate for the troposphere, is used. Observations of stratospheric $NO_2$ from the Halogen Occultation Experiment (HALOE) are used to estimate the bias introduced by the zonal invariance assumption. The GEOS-CHEM global chemistry-transport model is used to estimate tropospheric concentration profiles of $NO_2$. These profiles, along with surface albedo derived from GOME observations, are used to calculate air-mass factors using a radiative transfer model. Cloud fraction, optical thickness, and cloud-top pressure are determined using the GOMECAT retrieval algorithm, and incorporated into the air-mass factor calculation. In this study, an enhancement of observed $NO_2$ columns compared to the model over the Highveld are noted.

### 1.5.2 SCIAMACHY

The SCanning Imaging Absorption spectroMeter for Atmospheric CHartographY (SCIAMACHY) instrument flies on the Environmental Satellite (ENVISAT) satellite. ENVISAT was launched in March 2002 by the European Space Agency (ESA) (Gottwald *et al.* 2006). It is the largest satellite built by ESA, being 26 metres long and weighing 8140 kg. ENVISAT flies in a polar orbit; the orbital parameters are summarised in Table 1.1. SCIAMACHY stopped operating in early 2012.

The SCIAMACHY instrument is a passive scanning imaging spectrometer, measuring the wavelength ranges from 214 – 1773 nm, 1934 – 2044 nm and 2259 – 2386 nm with eight measurement channels. By using two scanning mirrors, the instrument is able to measure scattered sunlight from the atmosphere in both nadir and limb viewing geometries. SCIAMACHY is able to measure the solar spectrum by directly observing the sun when the satellite crosses the sub-solar point of its orbit, and to make solar and lunar occultation measurements in the limb viewing geometry (Bovensmann *et*

*al.* 1999). Operationally, SCIAMACHY alternates between nadir and limb viewing, hence viewing the same volume of air in both geometries within a short time (Figure 1.8).

The viewing geometries of the SCIAMACHY instrument are illustrated in Figure 1.9. The instantaneous field-of-view (IFOV) is 1.8° by 0.045°. The nadir swath is approximately 64° across track, with a ground pixel size of 25km x 0.6km based on the IFOV. Actual ground pixel sizes are larger, owing to the integration times used for collection of spectral data. In the limb viewing geometry, the tangent point with the earth is 3280km ahead of the satellite in the flight direction. The IFOV gives a pixel size of 105km x 2.5km in the limb geometry (Bovensmann *et al.* 1999, Noël *et al.* 2002). The nadir ground-pixel of SCIAMACHY is compared with that of the various satellite remote-sensing instruments in Figure 1.7 on page 15.

In order to maintain radiometric accuracy throughout the life of the instrument two calibration sources are carried on-board: a tungsten-halogen white light source and a neon-filled platinum-chromium cathode lamp as a spectral line source (Bovensmann *et al.* 1999).

Measurements of tropospheric $NO_2$ by SCIAMACHY are presented by Sioris *et al.* (2004) and by Richter *et al.* (2005) in the context of a time-series analysis. The retrieval follows a methodology similar to that described in Section 1.5.1 for GOME and a good match between the two instruments is found during the time that they operated concurrently. The stratospheric component of the measured column is determined from the SLIMCAT 3-d chemical transport model. Cloud screening is performed using the Fast Retrieval Scheme for Clouds from the Oxygen A-Band (FRESCO) algorithm based on a threshold of 0.2. Monthly average AMF are calculated using the SCIATRAN radiative transfer model, with the vertical profile of $NO_2$ taken from the Model for Ozone And Related chemical Tracers (MOZART-

Table 1.1: Satellite orbit parameters for satellites carrying high-resolution UV-visible spectrometers

| | ERS-2 | ENVISAT | Aura | METOP-A & B |
|---|---|---|---|---|
| Instrument | GOME | SCIAMACHY | OMI | GOME-2 |
| Mean altitude | 785 km | 799.8 km | 709 km | 817 km |
| Orbital period | 100 minutes | 100.6 minutes | 98.8 minutes | 101 minutes |
| Inclination | 98.52 ° | 98.55°± 0.01° | 98° | 98.7° |
| Repeat cycle | 35 days | 35 days | 16 days | 29 days |

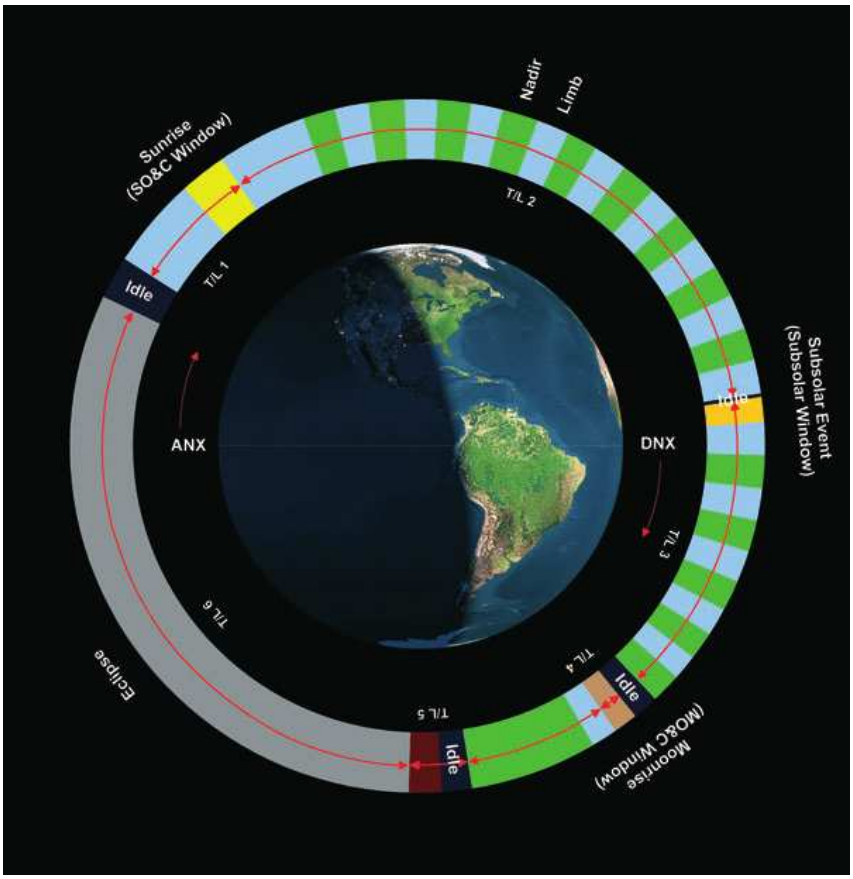


Figure 1.8: Orbit sequence of a typical SCIAMACHY orbit. The orbit's measurements will start with a sun occultation measurement of the sunrise, then alternating nadir and limb scattering measurements until the sub-solar point. At this point a direct solar spectrum measurement will be made through the sub-solar calibration window. Alternating limb/nadir measurements will continue for the remainder of the illuminated part of the orbit. If possible a moon-occultation measurement is made of the moon rise (after Gottwald *et al.* (2006)).

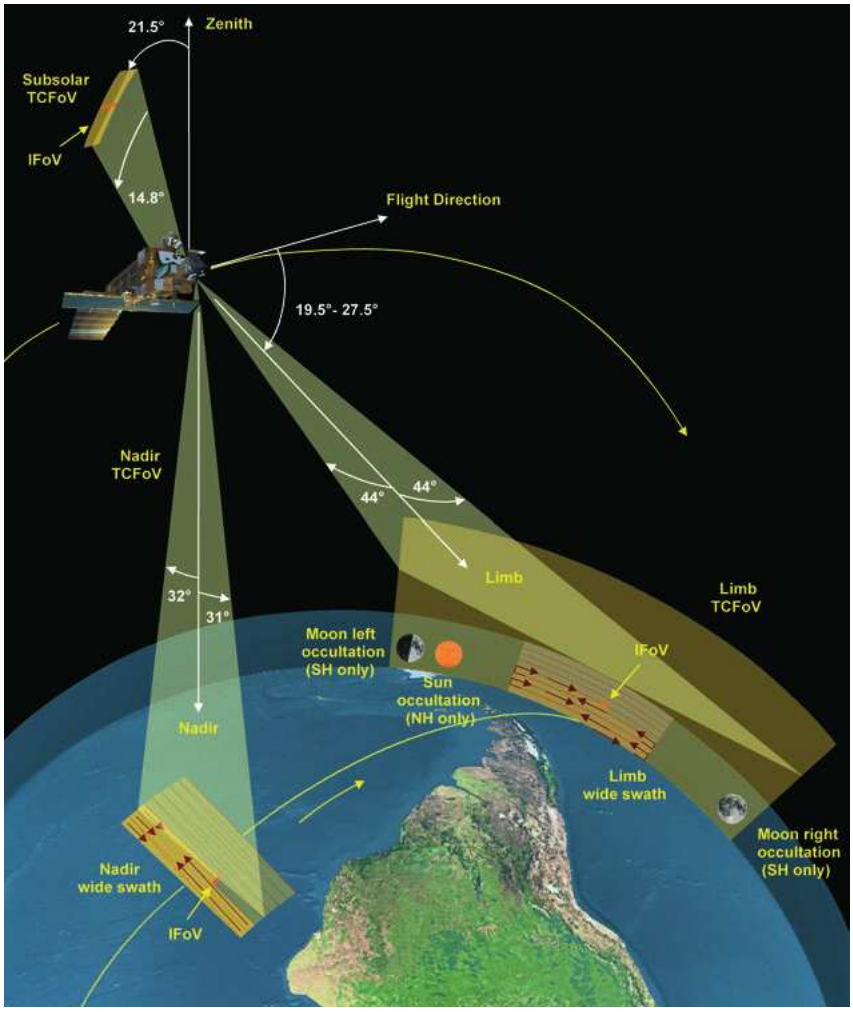


Figure 1.9: SCIAMACHY field of view: the instrument is able to observe the atmosphere in both nadir and limb geometries. There is also a sub-solar calibration window allowing direct measurements of the sun at the orbit's sub-solar point (after Gottwald *et al.* (2006)).

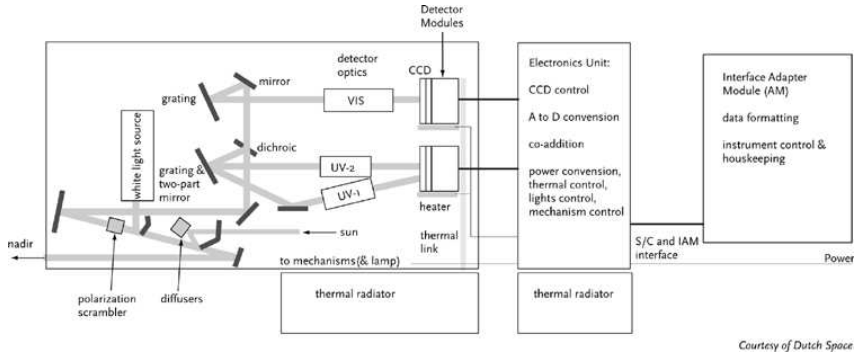


Figure 1.10: A schematic of OMI's systems (after Levelt *et al.* (2006)).

2) chemistry-transport model.

Vertical profile measurements of $NO_2$ retrieved from SCIAMACHY limb measurements are presented by Bracher *et al.* (2005) and Kühl *et al.* (2008).

### 1.5.3 OMI

The Ozone Monitoring Instrument (OMI) flies on the National Aeronautics and Space Administration (NASA) Aura satellite which was launched in December 2002. Aura's orbital parameters are summarised in Table 1.1 on page 18.

The OMI instrument is a nadir-viewing passive "pushbroom" imaging spectrometer. It uses two spectrographs to measure a wavelength range from 270 – 500 nm (Figure 1.10). The integration time of approximately two seconds gives a pixel size in the flight direction of 13 km, across-track pixels on the Charge-Coupled Device (CCD) are binned to give a maximum resolution in "zoomed in" mode, of 12 km (Figure 1.11). Operationally the across-track resolution is 24 km at nadir, broadening to approximately 150 km towards the edges of the swath. This is compared to other satellite sensor pixels in Figure 1.7 on page 15. The viewing telescope's 114° field-of-view gives a swath of 2600km (illustrated in Figure 1.12), giving almost daily global coverage (Levelt *et al.* 2006).

OMI has a solar-viewing aperture which is used for making a direct measurement of the solar irradiance once per orbit. In addition to this it has a white light source and LED spectral sources for in-flight calibration.

Retrievals of tropospheric $NO_2$ from OMI are done using a DOAS algorithm (Bucsela *et al.* 2006). $SO_2$ is retrieved using a band-residual difference al-

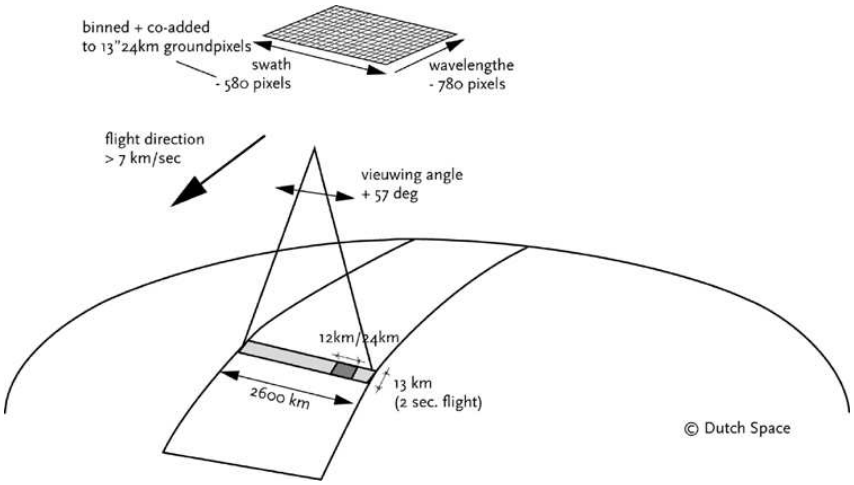


Figure 1.11: OMI measurement principle (after Levelt *et al.* (2006)).

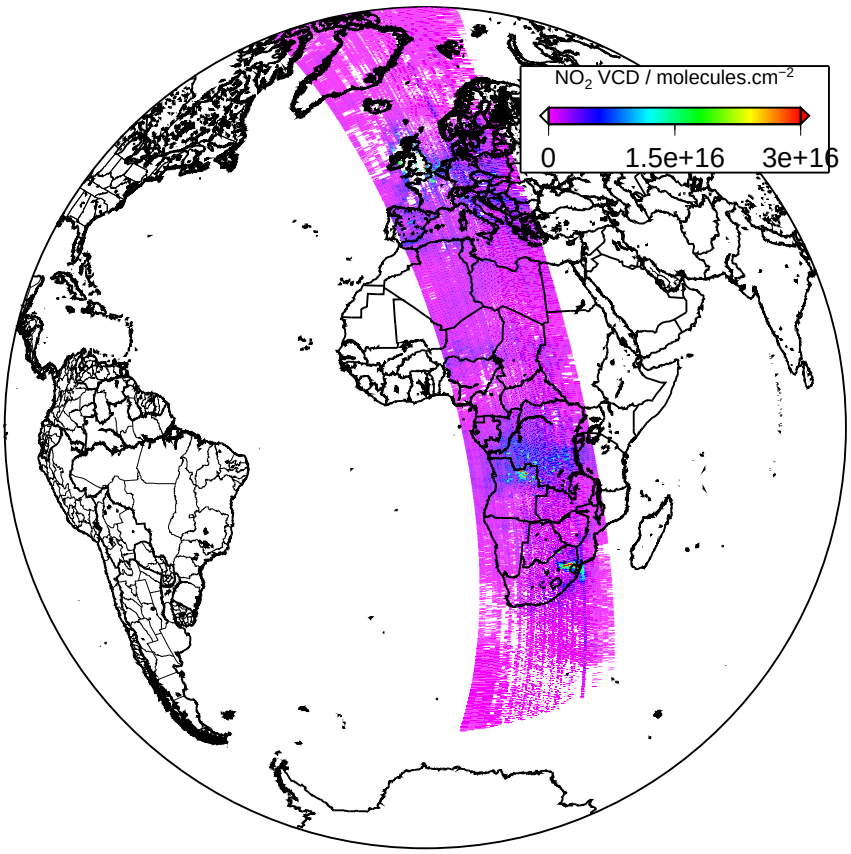


Figure 1.12: An example from 31 July 2008: tropospheric $NO_2$ measured by OMI during one orbit of Aura (after Broccardo *et al.* (2008)).

gorithm (Krotkov *et al.* 2006). Ozone column, ozone profile, BrO column, OClO column, HCHO column and cloud-top pressure are some of the other products retrieved from OMI measurements.

There are two global OMI $NO_2$ products available: the NASA standard product, and Derivation of OMI tropospheric $NO_2$ (DOMINO), of which there are two versions, 1.02 and 2.0. The standard product and DOMINO products share the slant column retrieval but differ in their treatment of the stratospheric contribution and the air-mass factor (Hains *et al.* 2010, Boersma *et al.* 2011). These differences lead to seasonally dependant differences in tropospheric $NO_2$. Over North America the DOMINO Version 1.02 $NO_2$ product is found to be 42 percent larger in winter and 22 percent smaller in summer compared to the NASA standard product (Lamsal *et al.* 2010).

DOMINO Version 2.0 improves on Version 1.02 with improved air-mass factors through better radiative transfer modelling based on higher resolution descriptions of surface pressure and albedo, and improved *a priori* vertical profiles of $NO_2$. Some improvements are also made in corrections for a bias resulting from measurement noise and differing wavelength calibration across the instrument swath (Boersma *et al.* 2011). Current versions of the NASA and DOMINO products give very similar results (Duncan *et al.* 2013).

As of 25 June 2007, OMI suffers from a so-called "row anomaly", which affects certain rows of pixels on the CCD detector (KNMI 2012) making the spectra measured by these rows unusable. The affected rows change over time, Level 1b and Level 2 data are flagged appropriately.

### 1.5.4 GOME-2

The Global Ozone Monitoring Experiment 2 (GOME-2) instruments are on board the ESA Meteorological Operational Satellite (Metop-A) and Metop-B satellites. These satellites were launched in October 2006, and September 2012 respectively. The satellites' orbit parameters are presented in Table 1.1 on page 18.

The scan width is 1920km, ground-pixel size is 80km by 40km. The instruments provide daily global coverage, with Level 2 data available within 3 hours via the Eumetcast system.

The DOMINO Version 2.0 product based on GOME-2 observations is available from Tropospheric Emission Monitoring Internet Service (TEMIS).

### 1.5.5 TROPOMI

The Tropospheric Ozone Monitoring Instrument (TROPOMI) instrument is planned to continue the heritage of satellite instruments from 2016 (Veefkind *et al.* 2012). It is planned for flight on the ESA Sentinel-5 Precursor satellite. TROPOMI includes a number of technical improvements over OMI including smaller ground-pixel size and a larger spectral range including bands in the near- and shortwave-infrared wavelengths. This should allow simultaneous retrievals of total column quantities of $O_3$, $NO_2$, CO, $CH_4$, $SO_2$, aerosols, $H_2O$, BrO, CHOCHO and OClO.

## 1.6 Applications of Satellite Trace-gas Measurements

### 1.6.1 Top-down Emissions and Lifetime Estimates

The detection of $NO_2$ "hotpots" on a global scale has been one of the successes of the satellite trace-gas measurement programs. The short lifetime of $NO_2$ in the troposphere means that areas of enhanced $NO_2$ in satellite images are close to the source. Martin (2003) derive a "top-down" emission inventory by quantifying the relationship between surface emissions and vertical columns using the GEOS-CHEM global chemistry-transport model. The calculated emissions for the Highveld are higher than the Global Emission Inventory Activity (GEIA) and Emission Database for Global Atmospheric Research (EDGAR) emissions inventories by up to 35 percent.

A novel technique is employed by Beirle *et al.* (2011) to simultaneously derive emissions estimates and $NO_2$ lifetime from megacities. OMI observations are classified according to wind direction from the European Centre for Medium-Range Weather Forecasting (ECMWF) model. $NO_2$ column densities are integrated in the across-wind direction, and a function based on a first-order reaction rate for $NO_2$ loss is fitted. From this procedure $NO_2$ lifetimes of between 2.3 to 6.4 hours are found, which is in good agreement with other estimates (Spicer 1982). Emission rates are found to agree reasonably well with the EDGAR inventory, for selected locations.

(Duncan *et al.* 2013) evaluates the impact of the installation of Emission Control Device (ECD) on a top-down inventory of emissions from power stations. In this study, a top-down inventory is derived without the use of a chemistry-transport model, significantly simplifying the technique. The

response of the satellite $NO_2$ measurement to changes in emissions is found to be inconsistent between different power stations, however there is some consistency in the response if the change in emissions is large.

### 1.6.2 Long-term Trend Detection

A time-series analysis of GOME data from 1996 to 2002 is presented by Richter *et al.* (2005). Global GOME tropospheric $NO_2$ data is re-gridded on a 0.5° by 0.5° grid, and the annual mean for each grid cell is calculated. A linear regression is perfomed for each grid cell. An ambiguous trend in the GOME measurements is detected over the South African Highveld, with an area of increasing tropospheric $NO_2$ immediately adjacent to an area showing a negative trend.

The monthly mean tropospheric $NO_2$ over east central China shows a clear annual cycle with a maximum in the winter season. This is attributed to a longer $NO_x$ lifetime in the winter boundary layer, different meteorological conditions and possible higher emissions in winter. The increase in the winter maximum is more pronounced than the increase in the mid-summer minimum over the nine year time period. The increase in the $NO_2$ measured by the satellite accelerated from a 4% increase between 1996–1997 to a 12% increase between 2001–2002.

van der A *et al.* (2008) use a multi-variate regression on GOME and SCIAMACHY data from 1996 to 2006, to determine long-term trends and seasonal variability of $NO_2$ globally. GOME data is re-gridded onto a one-degree grid by area-weighting, while the higher resolution SCIAMACHY data is downgraded to the grid resolution using a 3-grid cell convolution. The month of the seasonal maximum is determined from the regression parameters. A heuristic algorithm is used to classify the dominant $NO_2$ source in each grid cell into anthropogenic, soil, biomass-burning or lightning. A statistically significant positive trend is found over a part of the Highveld, with a significant negative trend in the surrounding areas to the south and east. The dominant source over the Highveld is found to be anthopogenic, with some areas where lightning dominates found to the south-east, and a large area of dominant soil emissions over the western half of South Africa and into Namibia.

Trends in the GOME and SCIAMACHY monthly average $NO_2$ over India, and several regions within India, are examined by Ghude *et al.* (2008). The method used to account for the difference in spatial resolution between the

two satellites is not described. The regions are defined based on areas with high average December values of $NO_2$ observations, and an increasing linear trend is found in all the regions examined. A harmonic expansion is used to account for seasonal variations, which also accounts for changes in the seasonal amplitude with time. Four of the five sub-regions defined also show increases in seasonal amplitude, with increases in the peak $NO_2$ and decreases in the minimum $NO_2$ observed.

Hilboll *et al.* (2013) devise a method to account for differences in spatial resolution between different satellite instruments.

The complete archive of SCIAMACHY measurements between August 2002 and March 2012 are used by Schneider *et al.* (2015) to examine global trends in $NO_2$ over large urban areas. Level 3 data on a 0.25 degree grid is used, and a harmonic expansion is used to model seasonality. Johannesburg is found to have a significant negative trend in $NO_2$ vertical column densities.

### 1.6.3 Intercontinental Transport

A case study of $NO_2$ and aerosols from forest fires in Canada observed by GOME and Total Ozone Mapping Spectrometer (TOMS) crossing the Atlantic Ocean to Greenland and Europe is presented by Spichtinger *et al.* (2001). The satellite observations are compared with a model study using Flexible Particle dispersion model (FLEXPART) of the same event.

In a similar vein, Wenig *et al.* (2003) present a case study of $NO_2$ from the Highveld, where a sub-tropical high pressure allowed the re-circulation and accumulation of pollution. A low pressure system approaching from the West led to lifting of the $NO_2$ to higher altitudes ahead of the cold front. This would allow the GOME sensor to more easily detect the $NO_2$. The strong winds at high altitude associated with the frontal system led to rapid transport across the Indian Ocean towards Australia.

A model run using FLEXPART shows a good spatial correlation with the GOME observations. Lightning Imaging Sensor (LIS) data shows that there was some lightning activity in the regions of enhanced $NO_2$ observed by GOME. This introduces some uncertainty as to the origin of the observed $NO_2$. However, the Highveld plume is further west from the region of the lightning, and the quantity of $NO_2$ produced by the lightning is estimated to be small, hence the authors attribute the origin of the plume transported across the Indian Ocean to be the Highveld.

Stohl *et al.* (2003) take a similar approach to the analysis of an example of

intercontinental transport of $NO_2$ across the North Atlantic Ocean, taking only about a day to cover this distance. The high windspeeds necessary for this rapid transport are associated with rapid cyclogenesis: a meteorological "bomb". In this case, similarly to Wenig *et al.* (2003), vertical transport of $NO_2$ to higher altitudes allows the satellite sensor to more easily detect it. Using a sophisticated analysis of the meteorology, and exhaustive analysis of possible lightning $NO_x$ production, the authors unambiguously attribute the $NO_2$ observed to anthropogenic sources.

An algorithm is used by Zien *et al.* (2014) to detect long-range transport events in daily GOME-2 $NO_2$ data. These events are usually linked to the passage of frontal systems, and using non-cloud-screened data reveals that these events are more common than what was previously thought.

### 1.6.4 Lightning and soil $NO_x$ detection

Soil and lightning $NO_x$ are studied by Jaeglé (2004) using GOME measurements during the year 2000. Seasonal pulses in $NO_2$ observed in several locations around west Africa are compared in time and space with rainfall, fire and lightning measurements from Tropical Rainfall Monitoring Mission (TRMM), and attributed to soil emissions. An inverse modelling technique is used to estimate source strengths.

A ten-year dataset of GOME and SCIAMACHY from 1996 – 2006 is examined by van der A *et al.* (2008). Monthly mean $NO_2$ TVCD on a global 1° by 1° grid is fitted with a seasonal model. A significant positive trend in $NO_2$ column densities over the Highveld is found. A negative trend is found over most of the sub-continent, to the east and to the south of the Highveld, for both of which it is suggested the cause is a reduction in biomass burning activity due to de-forestation. Other possible causes suggested are changes in surface albedo, aerosols and cloudiness or meteorological conditions. Seasonal variation, using the month of peak $NO_2$ as an indicator, is compared with global model results to identify the dominant source of emissions in each grid cell. Emissions are categorised as being anthropogenic, or from biomass burning, soil or lightning.

Ghude *et al.* (2010) analyse vertical $NO_2$ column trends from OMI over three sparsely-populated areas in India. Accumulated rainfall over the same areas is estimated from TRMM. A time-series correlation of $NO_2$ columns with rainfall in each area shows a pulse of $NO_2$ following rainfall events. Biomass burning and nearby point sources are ruled out using the Moderate Res-

olution Imaging Spectroradiometer (MODIS) fire-count data and prevailing wind direction from the National Centers for Environmental Prediction (NCEP) re-analyis. The authors attribute the enhanced $NO_2$ column densities to soil $NO_x$ emissions following rainfall associated with the start of the Monsoon.

A systematic study of $NO_x$ produced by lightning is presented by Beirle *et al.* (2010). Data from the World-Wide Lightning Location Network (WWLLN), the LIS/OTD, and SCIAMACHY are used to estimate the $NO_x$ produced per lightning flash.

## 1.7 Satellite Validation

An evaluation of GOME tropospheric columns using in-situ aircraft measurements of $NO_2$ and HCHO is presented by Martin (2004).

Hains *et al.* (2010) use ground-based Multi-Axis DOAS (MAXDOAS), ground-based lidar, ground-based and airborne in-situ vertical profiles of $NO_2$ to validate OMI tropospheric $NO_2$ products over Europe and North America. The DOMINO Version 1.02 product is shown to correlate better than the standard product, with the standard product showing a bias towards underestimation. Measured vertical profiles of $NO_2$, and improved surface albedos are used to calculate an improved air-mass factor for OMI, which results in an improvement in the correlation between retrieved OMI $NO_2$ and the basket of measured vertical columns.

The PANDORA instrument is a ground-based, direct-solar viewing, high-resolution spectrometer: $NO_2$ column amounts are retrieved using a DOAS retrieval (Herman *et al.* 2009). Josipovic *et al.* (2013) examine $NO_2$ column measurements from a PANDORA instrument co-located with a ground-based in-situ monitor, as well as OMI $NO_2$ vertical column measurements. Column densities are compared with surface measurements using a Planetary Boundary Layer (PBL) height correction factor. The PANDORA measurements, converted to representative surface concentrations, are found to agree with the in-situ surface measurements within the expected uncertainty. OMI $NO_2$ column measurements are found to exhibit greater-than-expected discrepancies with the surface data.

Lin *et al.* (2014) develop and improved tropospheric AMF for OMI over China, and evaluate OMI tropospheric $NO_2$ products and their improved VCD with co-located ground-based MAXDOAS measurements.

## 1.8 Airborne DOAS

A validation of SCIAMACHY tropospheric $NO_2$ is presented by Heue *et al.* (2005) using an Airborne Multi-Axis DOAS (AMAXDOAS). The AMAXDOAS instrument uses eight telescopes coupled to optical fibres to bring light from four upward-looking and four downward-looking viewing directions to two imaging spectrographs. A direct comparison of the AMAXDOAS measurements over the Alps, the Po River Valley in Italy and the Mediterranean shows a good correlation with the satellite retrieval.

Emission flux measurements of $SO_2$ from power plants using an airborne DOAS instrument are presented by Melamed *et al.* (2008). Zenith and nadir viewing geometries are enabled using a rotating mirror. A quartz fibre is used to transmit the light, via collimating optics and a Schott UG11 filter to a spectrograph. The filter decreases the intensity of light in the visible range, allowing a long enough integration time to gather light in the UV wavelengths without saturating the detector. Air-mass factors are calculated using a combination of radiative transfer modelling and enhancements in $O_4$ differential slant-column density. The sum of the nadir and zenith vertical columns are used to calculate the emission flux: the aircraft was determined to be flying within the planetary boundary layer by concurrent enhancements in measured in-situ $SO_2$. Uncertainties in the calculated fluxes are up to 52 percent, however in general good agreement is found with in-stack measurements.

Kazahaya *et al.* (2008) perform tomographic reconstruction of $SO_2$ concentrations in a volcanic plume from a helicopter-borne DOAS instrument. Combined with wind speed, the emission flux from the volcano is calculated. Three upward-looking telescopes at different angles are used, with the helicopter flying beneath the plume. No air-mass factor calculations are performed in this study.

The imaging capability and the possibility of using an airborne Imaging DOAS (iDOAS) instrument to determine emission flux from a large point source is demonstrated by (Heue *et al.* 2008*a*), using data from the flight on 5 October 2006 described in Section 3.3 of the present work. An image of the $NO_2$ plume from Majuba power station is shown in Figure 1.13a. This image is overlaid on a Google Earth image in Figure 1.13b. Time-series of CCD lines representing positions across the DOAS swath upwind and downwind of the power station are shown in Figure 1.14a. The $NO_2$ flux is calculated for each CCD line using wind speed from a nearby weather station. Calculated fluxes are shown in Figure 1.14b; a clear linear increase in $NO_2$ flux

downwind of the power station is visible.

Dix *et al.* (2009) present the configuration of, and measurements of trace gases from the DOAS instrument on board Civil Aircraft for the Regular Investigation of the atmosphere Based on an Instrument Container (CARIBIC) aircraft. These are passenger aircraft flying on intercontinental flights, which carry a container fitted with scientific instruments. The CARIBIC project allows measurements to be made over long distances, and long term: DOAS measurements started in 2005. Three telescopes at different elevation angles are mounted in a pylon on the aircraft. Entrance optics consist of quartz lenses and prisms, and a Schott UG5 filter to reduce the intensity of light in the visible wavelengths. Quartz fibres couple the entrance optics to a separate temperature-controlled spectrograph for each elevation angle.

Measurements of HCHO, HONO, $NO_2$, BrO, $O_3$ and $O_4$ are made. (Dix *et al.* 2009) present the first measurements of HONO in a deep convective cloud, and measurements of BrO, $NO_2$ and $O_3$ in regions of tropopause folding. Heue *et al.* (2010) and Heue *et al.* (2011) present observations of volcanic $SO_2$ and BrO plumes by CARIBIC DOAS and GOME-2 satellite measurements. Observations by CARIBIC DOAS of lightning $NO_x$, HONO and HCHO at the parts-per-trillion level in a convective cloud are presented by Heue *et al.* (2014). These observations are possible because of the enhancement in the light path by cloud-droplet multiple scattering.

Baidar *et al.* (2013) present the most recent development of airborne multi-axis DOAS. The CU-AMAXDOAS (Colorado University Airborne Multi-Axis DOAS) described features motion compensation to decouple the instrument field of view from changes in aircraft attitude, and allows measurements of solar scattered light at viewing angles from nadir to zenith to be made in flight. Measurements of boundary layer $NO_2$ and aerosol optical depth from the CU-AMAXDOAS are shown to be in good agreement with ground-based in-situ $NO_2$ and Aerosol Robotic Network (AERONET) measurements.

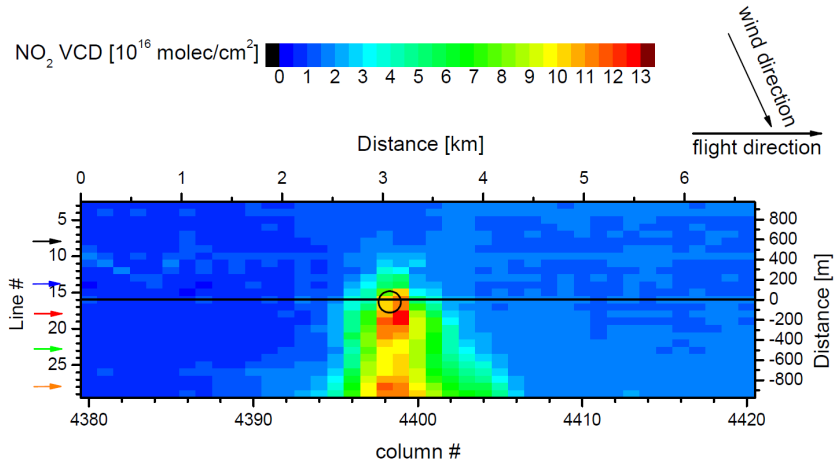


(a)

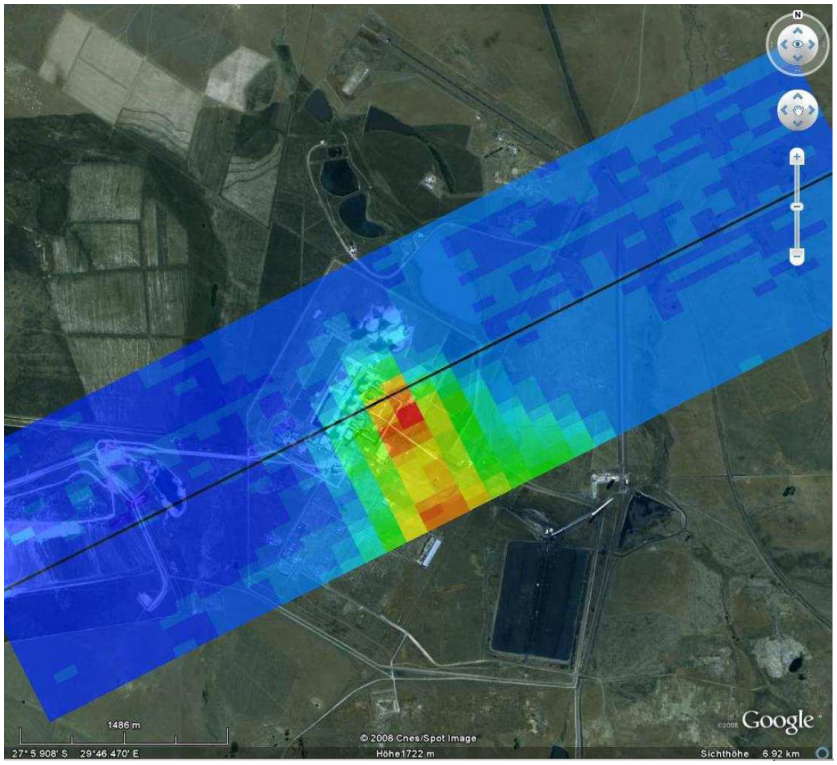


(b)

Figure 1.13: (a) High spatial resolution of the airborne iDOAS instrument demonstrated overhead Majuba power station on 5 October 2006 (b) $NO_2$ column densities overlaid on a satellite image (after Heue *et al.* (2008*b*)).

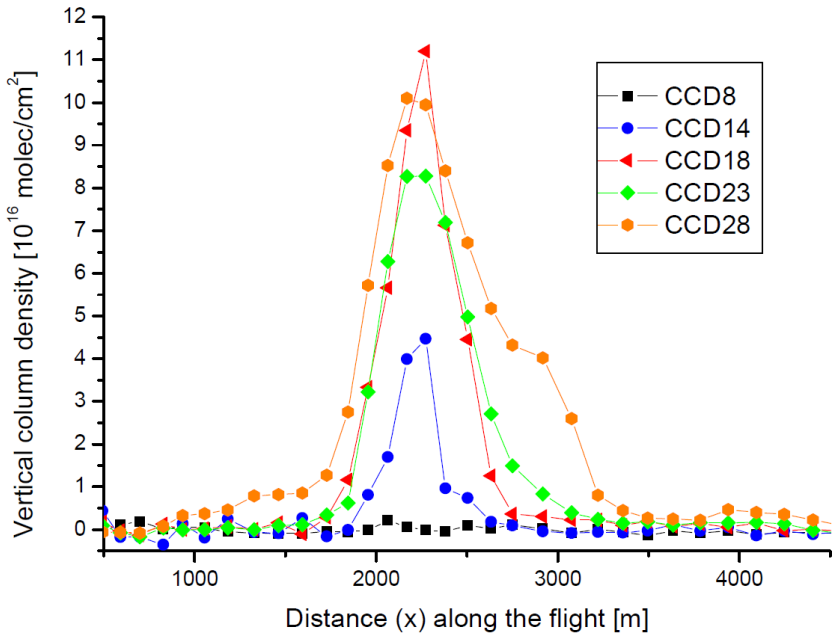


(a)

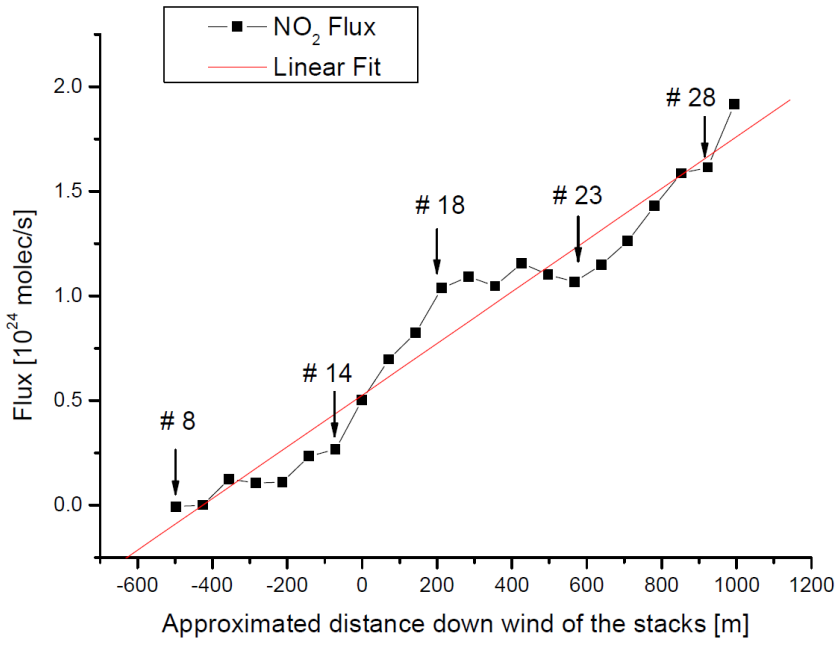


(b)

Figure 1.14: (a) $NO_2$ VCD for each CCD line. Line colours correspond to the arrows on the left of Figure 1.13a: the black line is upwind of the stack, blue is deemed to be approximately 60m upwind, red, green and orange are progressively further downwind (b) The $NO_2$ flux calculated at approximate distances downwind from Majuba. CCD line numbers are indicated, corresponding to the coloured lines in (a) (after Heue *et al.* (2008*b*))

# Chapter 2

# Methods

## 2.1 Aircraft Measurements

The aircraft used for the present study was a Rockwell Aerocommander 690A belonging to the South African Weather Service (SAWS), based at Bethlehem airfield. Flight measurement campaigns were held during 2006 and 2007, the standard flight altitude of 18000 to 20000 feet (approximately 5500 to 6000 metres) above mean sea level (AMSL) during both of these campaigns was substantially above the mixed-layer height. Two flight strategies were used: 1. regional mapping 2. satellite tracking. Regional mapping flights were performed by flying a grid pattern over the area of interest, bearing in mind the complexities of the airspace around greater Johannesburg. The general approach to satellite tracking was to ferry at low altitude to a position along the predicted satellite track, perform a spiral vertical profile from approximately 1500 feet (460m) above ground to the cruise altitude of 19000 or 20000 feet (5800 to 6100 metres), before following the satellite track as far as the aircraft's endurance would allow. A second spiral vertical profile was performed while descending to 1500 feet above ground, before either returning to Bethlehem or re-fuelling at some other airfield.

### 2.1.1 Position and state instrumentation

Ambient air temperature, static pressure, dynamic pressure and dewpoint were measured by instrumentation mounted on the aircraft nose boom (Figure 2.1). The instruments are specified in Table 2.1. Measurements from these instruments, as well as position and time from the Global Positioning System (GPS) were logged on the data acquisition system. This data

Figure 2.1: The aircraft nose-boom with instrumentation (from left to right): FSSP probe in pod, King liquid water probe, dewpoint (in vertical pylon in the centre of the nose), pitot tube for dynamic pressure measurements, Rosemount 102 temperature probe, PCASP probe in pod.

acquisition system was a custom built system that was supplied with the aircraft.

### 2.1.2 In-situ measurements

In-situ measurements of $NO_y$, aerosol number concentration and temperature were binned into vertical intervals of 50m for $NO_y$ and aerosols, and 20m for temperature. These were plotted against altitude for the times that the aircraft was performing the vertical profiles and are presented in Section 3.1.

#### In-situ $NO_y$

A Thermo Scientific $NO_x$ analyser was plumbed into the aircraft's air sampling inlet (illustrated in Figure 2.2). The instrument can be seen in Figure 2.3. A pump in the luggage area aft of the cabin's rear pressure bulkhead

Table 2.1: Instrumentation to measure state parameters in flight

| Parameter | Manufacturer | Model |
|---|---|---|
| Temperature | Rosemount | 102 AU1AF (de-iced) |
| Static Pressure | Rosemount | 1201F A1B2B |
| Dynamic Pressure | Rosemount | 1221F2 VL18B2A |
| Dewpoint | Vaisala | DMP248 |
| GPS | ESD | DTS1 |

was used to draw air through the $NO_x$ analyser. The critical orifice inside the instrument was removed and a mass-flow controller was used to fix the flow-rate inside the instrument at five litres per minute. The $NO_x$ instrument was calibrated before each flight using a Thermo Scientific calibrator, zero air generator and calibration gas. The instrument's voltage outputs for NO and $NO_x$ were logged on the data acquisition system using an appropriate scaling factor to convert the analogue voltage output to concentration. Since the $NO_x$ analyser uses a standard molybdenum catalyst rather than a photolytic converter, the instrument was in fact measuring not $NO_2$ but rather a portion of $NO_y$.

#### In-situ aerosol measurement

A Particle Measurement Systems (PMS) Passive-Cavity Aerosol Spectrometer Probe (PCASP) was mounted on the nose-boom of the aircraft (Figure 2.1). Number concentration and size spectrum between 0.1 and 2.5 microns diameter is calculated by the instrument based on a single-scattering assumption and logged on the data logging computer at one Hertz frequency. In addition a PMS Forward-Scattering Spectrometer Probe (FSSP) was flown on the nose boom, however this probe is suited for the measurement of cloud droplets and hence is not relevant to the present study.

### 2.1.3 Airborne DOAS

An Imaging DOAS (iDOAS) instrument was mounted on the seat rails of the aircraft. The instrument is shown in Figure 2.3. A quartz window mounted in the aircraft's camera-hole allowed a nadir-viewing pushbroom geometry, illustrated in Figure 2.4.

The iDOAS instrument is based on an Acton 300i Czerny-Turner imaging

Figure 2.2: The air sampling inlet on the roof of the aircraft.

spectrograph, and an Andor DU-420BU CCD camera. Mirror-based entrance optics produced a swath width of 28°; however the size of the window in the aircraft floor reduced the effective swath to 24°. The spectrograph was enclosed in an insulated box with thermostatic temperature control. The temperature of the spectrograph was held at 30°C. The camera temperature was held at -20°C using its internal thermoelectric cooler. A Personal Computer (PC) with custom software was used for controlling the camera and logging data. Spectra were matched to positions from the GPS system by their timestamps. The instrument is further described by Heue *et al.* (2006).

CCD pixels were binned in post-processing to create 27 viewing directions across the swath. Each viewing angle has a different instrument function, which was determined from laboratory measurements of a mercury-vapour lamp's emission lines. Dark current was subtracted from the measured spectra for each viewing direction. Spectral calibration was performed on the ground using the mercury-vapour lamp, and in the air using solar Fraunhofer lines.

For each viewing direction, a solar Fraunhofer reference spectrum (Kurucz *et al.* 1984), and reference spectra for $NO_2$ (Vandaele *et al.* 1998), $O_3$ (Bogumil

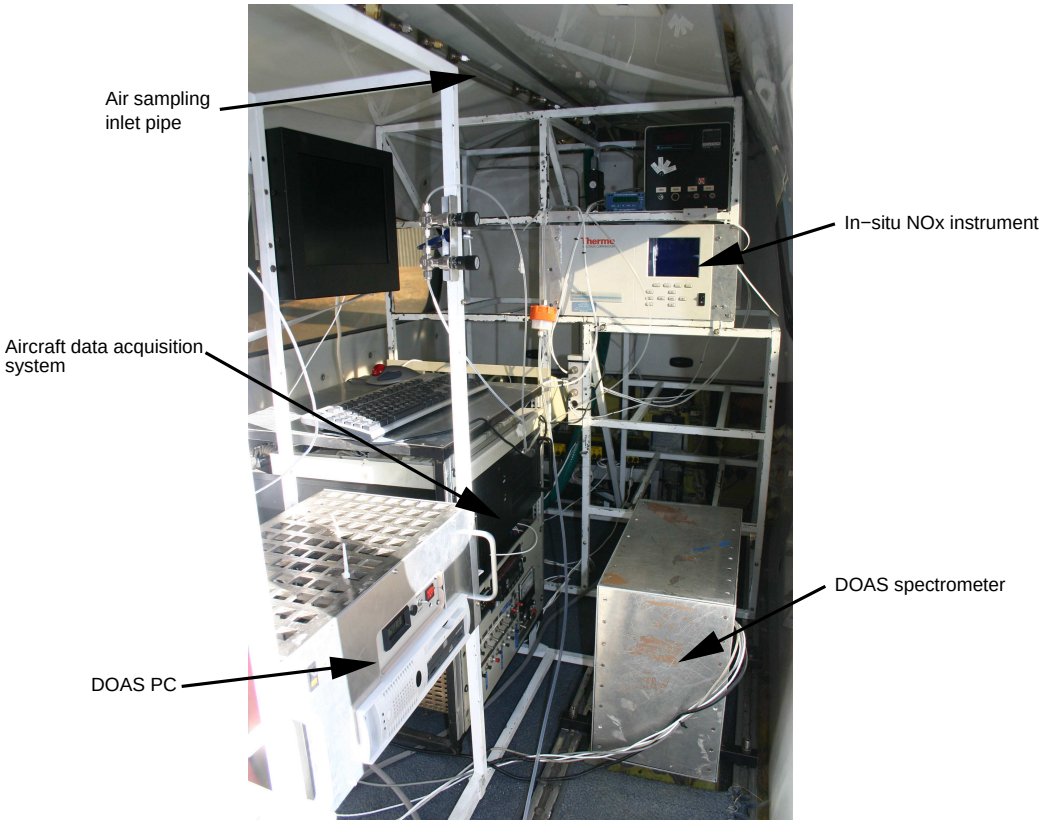


Figure 2.3: The interior of the aircraft cabin showing the DOAS spectrograph and PC, the $NO_x$ instrument, and the aircraft data acquisition system.

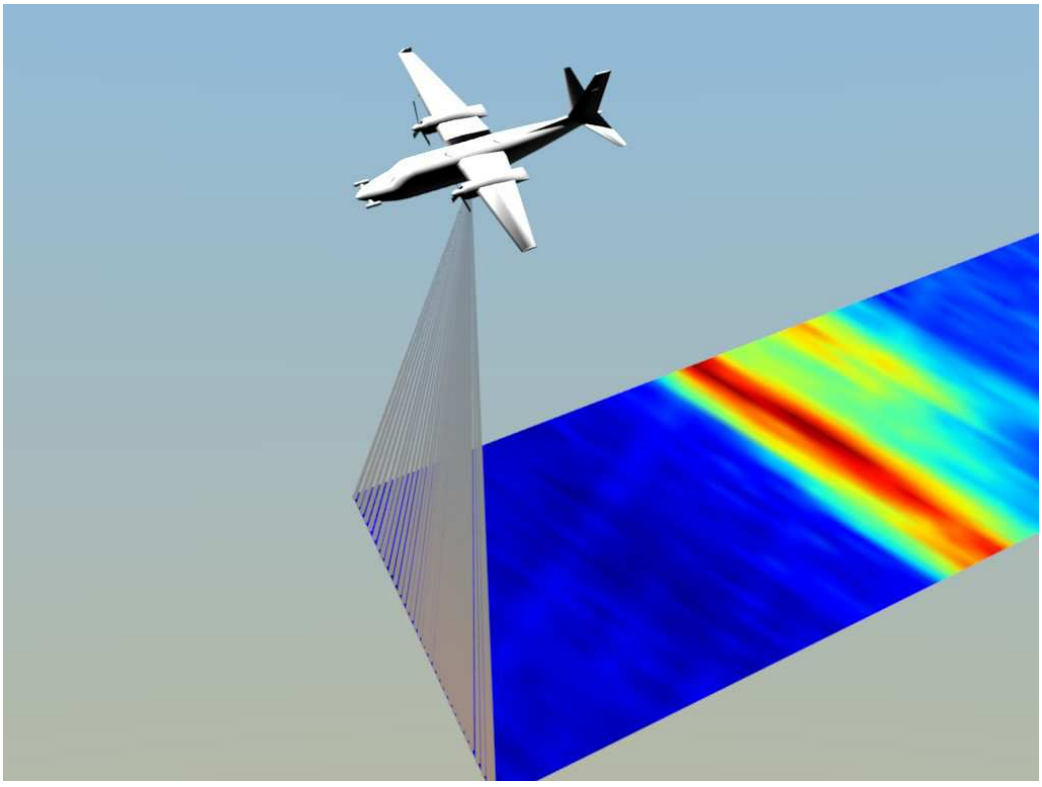

Figure 2.4: Schematic illustration of the aircraft and DOAS pushbroom-imaging geometry.

*et al.* 2003), $O_4$ (Greenblatt *et al.* 1990), and $H_2O$ (Rothman *et al.* 1998) were convolved with each of the instrument functions. A Ring spectrum was calculated from the Fraunhofer reference spectrum (Bussemer 1993). A DOAS retrieval was performed using WinDOAS for the above species using a wavelength range from 432 to 464 nm.

In the present work, the imaging ability of the airborne DOAS, demonstrated by (Heue *et al.* 2008*b*) was not exploited. Only the nadir pixel is used for all of the analysis presented in Chapter 3.

For the calculation of fluxes, presented in Section 3.3, the method described by Heue *et al.* (2008*b*) is used:

$$\Phi = \int VCD(x) \cdot v_w \cdot sin(\alpha) \cdot \mathrm{d}x \tag{2.1}$$

where $\Phi$ is the flux, $v_w$ is the wind speed, $\alpha$ is the angle between the wind direction and the flight direction and $x$ is distance along the flight direction.

## 2.2 Radiative Transfer Modelling

In order to evaluate the impact of different aerosol and trace gas vertical profiles on the $NO_2$ AMF, several scenarios were devised based on the shapes of the measured vertical profiles of trace-gas and aerosols. Air-mass factors were calculated at 430nm wavelength for each scenario using the SCIATRAN radiative transfer model version 2.2.2 (Rozanov *et al.* 2005). The first group of scenarios assume a well-mixed PBL, with a constant $NO_2$ mixing ratio and aerosol number density between the surface and the top of the PBL. The second group assume an exponential decrease in these two quantites, with a scale height of 600m. Profiles with an elevated layer of $NO_2$ and aerosols, above the PBL block or exponential profile, between 2200m and 2400m above ground were devised. In addition to this, four scenarios with the height of the ground at 1500m AMSL (approximating what is found over the Highveld) were modelled.

Volume mixing ratios (VMRs) were calculated to ensure that all the scenarios have the same $NO_2$ vertical column density of $2{\times}10^{16}$ molecules.cm$^{-2}$. OMI Level-2 data shown in Figures 3.14, 3.15 on pages 69 and 70, and similar figures from other days indicate that this is a reasonable choice of column density to use for a modelling exercise. Level-3 data timeseries in Figure 4.16 on page 111, similarly show that this is a reasonable choice.

A naïve model of aerosols was used. The profile shape of aerosol number concentration is assumed to be the same as that of $NO_2$ (except for Scenario 8, where the profile shapes of aerosols and trace-gas are different), and the simplifying assumption was made that there is no change in aerosol optical properties, and hence extinction efficiency factor, with altitude. Aerosols were assumed to be perfectly reflecting, the necessary correction algorithm for conservative scattering was enabled in the model. These assumptions resulted in a profile shape of aerosol extinction coefficient similar to the trace-gas profile shape. The aerosol extinction coefficient was calculated to give an aerosol optical thickness of 0.5 for the first ten scenarios. The results from these scenarios are used in Section 3.2. In order to evaluate the effect of a change in aerosol loading, scenarios 14, 15, 19 and 20, are based on the shapes of scenarios 4, 5, 9, and 10 respectively, but use an aerosol optical thickness of 0.75. Similarly, scenarios 24, 25, 29 and 30 use an aerosol optical thickness of 1.0, while maintaining the profile shapes of scenarios 4, 5, 9 and 10. Results from these additional scenarios are presented in Chapter 4. For all the scenarios, a Henyey-Greenstein parameterisation with an asymmetry factor of 0.7 is used for the aerosol scattering phase function.

A range of solar zenith angles between 35° and 60° were modelled, as well as view angles of zero (nadir) and 10°. An altitude grid from zero to ten kilometres in steps of two hundred metres was used. For aircraft air-mass factors, instrument altitude was set at 6000m and for satellite tropospheric air-mass factors, it was set to 10000m (i.e. the top of the altitude grid). Calculations were repeated for surface albedos of 0.02, 0.05, and 0.10, with the surface assumed to be a Lambertian reflector. The azimuth angle for all calculations was 39°; no effect was expected given the Lambertian surface reflector assumption, nor found from using an azimuth angle of 219°, as would be the case if the aircraft flew on a reciprocal heading.

## 2.3 Satellite Data

### 2.3.1 Level-2 Data

OMI DOMINO Version 2.0, Level-2 data were obtained from the TEMIS website for direct comparison with the airborne DOAS. A PostGIS (www.postgis.org) database was used to store tropospheric vertical column densities and easily allow spatial matching with the aircraft data. GOME-2 (Richter 2008) and SCIAMACHY (Beirle 2008) data were obtained and treated in a similar fashion. With the satellite and aircraft data captured in the database,

a simple spatial Structured Query Language (SQL) query will match the aircraft-measured column density with the satellite measurement at aircraft nadir. For example, for 9 August 2007:

```
SELECT a.time,o.time,a.no2scd,o.tropvcd
FROM aircraft a, domino o WHERE
ST_Within(a.latlon, o.corners) AND
EXTRACT(DAY FROM o.time)=9 AND
EXTRACT(DAY FROM a.time)=9
```

### 2.3.2 Level-3 Data

NASA standard product OMI Tropospheric $NO_2$ Level-3 daily data was downloaded from the NASA web site for the time period between 1 January 2005 and 31 December 2013. This product (OMNO2d) was released on 10 January 2013. The spatial resolution of the data is 0.25°, re-gridded from the Level-2 data by averaging all good-quality data within each grid cell.

A non-linear fitting algorithm was used to fit a polynomial of the form:

$$y = \beta_0 + \beta_1 x + \beta_2 \sin(\frac{\pi x}{182.5} + \beta_3) \tag{2.2}$$

to the nine-year time-series of daily measurements in each spatial pixel of the data, where $y$ is the tropospheric $NO_2$ column density and $x$ is the day number in the time-series. The $\beta_0$ parameter will be the $NO_2$ Level-3 VCD at the start of the analysis (i.e. the y-intercept), $\beta_1$ will be the linear trend. The $\beta_2$ parameter is the amplitude of seasonal variation, while $\beta_3$ is a time-shifting parameter, that is converted into a Julian day of the seasonal peak for interpretation. Maps of the $\beta$ parameters were produced and are shown in Chapter 4. A similar model is fitted to monthly average data on a 1° global grid by van der A *et al.* (2008). Other studies such as Ghude *et al.* (2008) have used a harmonic expansion to account for seasonal effects.

Mean, maximum, minimum, and the fraction of days with valid measurements during the time-series were calculated for the whole nine-year period, and also for each season. The seasons used for these calculations were March, April, May (MAM), June, July, August (JJA), September, October, November (SON) and December, January, February (DJF). Maps were produced of each of these calculated values.

Regions of interest (ROIs) were selected based on inspection of the maps, and spatial means were calculated within each sub-region for each day. A

polynomial was fitted to the daily spatial mean data. Monthly mean values were calculated from the daily spatial means within each ROI. Time-series plots of the daily spatial mean, polynomial fit, and monthly mean data were made.

Recognizing that some areas have high seasonal variation in $NO_2$ VCD as well as high seasonal variation in cloud cover, a mean was calculated from satellite measurements, where missing daily values are replaced with a value derived from the polynomial fit of the seasonal model. This is effectively a non-linear interpolation between days where data is available. Maps of the corrected mean, and of the difference between the ordinary mean and the corrected mean were produced.

# Chapter 3

# Aircraft Measurements

Vertical profile measurements of $NO_2$ and aerosols are presented. From the features identified in these profiles, some representative vertical profiles are devised, and a sensitivity study of air-mass factor with respect to vertical profile shape was performed using the SCIATRAN radiative transfer model. Since the $NO_x$ instrument was fitted with a molybdenum catalyst, the measurements are not suitable for direct comparison with satellite vertical column measurements.

Airborne DOAS results from five flights are presented (Table 3.1). The flight on 5 October 2006 provides a general overview of plume dispersion over the Highveld on this day. Four flights from the 2007 campaign were planned to follow satellite tracks, allowing a direct comparison to be made.

Table 3.1: Details of Flights over the Highveld

| Date | Strategy |
|---|---|
| 5 October 2006 | Regional mapping |
| 9 August 2007 | Satellite tracking |
| 11 August 2007 | Satellite tracking |
| 14 August 2007 | Satellite tracking |
| 18 August 2007 | Satellite tracking |

## 3.1 Vertical Profiles

The vertical profile of aerosols and trace gases exerts an influence over radiative transfer through the atmosphere, and hence on the Air-Mass Factor (AMF) used to convert slant column to vertical column densities. Measured vertical profiles of aerosol number concentration and size spectra, $NO_y$ and temperature from the flights conducted in 2007 are presented. Details of the instrumentation are given in Section 2.1.2. These measured profiles are used to develop representative idealised vertical profiles, which are used to estimate the sensitivity of the AMF to variations in the vertical profile of trace gases and aerosols by Radiative Transfer Model (RTM).

A campaign summary of particle size spectra is presented in Figure 3.1. The size spectrum plots in this figure are reproduced in subsequent figures. The first (ascending) profile of each flight is coloured cyan, the second (descending) profile is in orange. The rectangular bracket to the left of each spectrum plot indicates the altitude interval that it represents. Inspection of this figure indicates that the aerosol size distribution during the campaign can be approximated by a bimodal log-normal distribution with modes at particle diameters of 0.1 microns and 2.0 microns. One can surmise that the aerosol population conforms to the model used for the MODIS collection 5 dark-target land retrieval (Levy *et al.* 2009). It appears that this is the case at all altitudes measured. For the RTM scenarios the simplifying assumption of a constant extinction efficiency factor (EEF) is made, implying that the extinction coefficient will be proportional to aerosol number concentration.

Vertical profiles were performed at the start and end of the satellite-tracking leg of the flight on 9 August 2007. The first vertical profile was done in a climbing holding pattern from approximately 1500 feet (460m) above ground to 20000 feet AMSL (6096m) at a position approximately 50km north-east of Bethlehem, in the direction of the town of Warden. This position was chosen since it was on the track of the Aura satellite, which carries the OMI instrument. The profile was started at 12:01 UTC and complete at 12:25 UTC. Data from the climb directly after takeoff from Bethlehem is used to extend the profile lower than the start of this manoeuver. Partial failure of the data logging system early in this flight means that $NO_y$ data are not available for this lower portion. Profiles of aerosol number concentration, $NO_y$, and ambient temperature are shown in Figure 3.2a. Number concentration and $NO_y$ is averaged over altitude bins of 50m, temperature over altitude bins of 20m. In addition, Figure 3.2a shows average particle size spectra for the altitude intervals 1650–2000m and 2300–2600m.

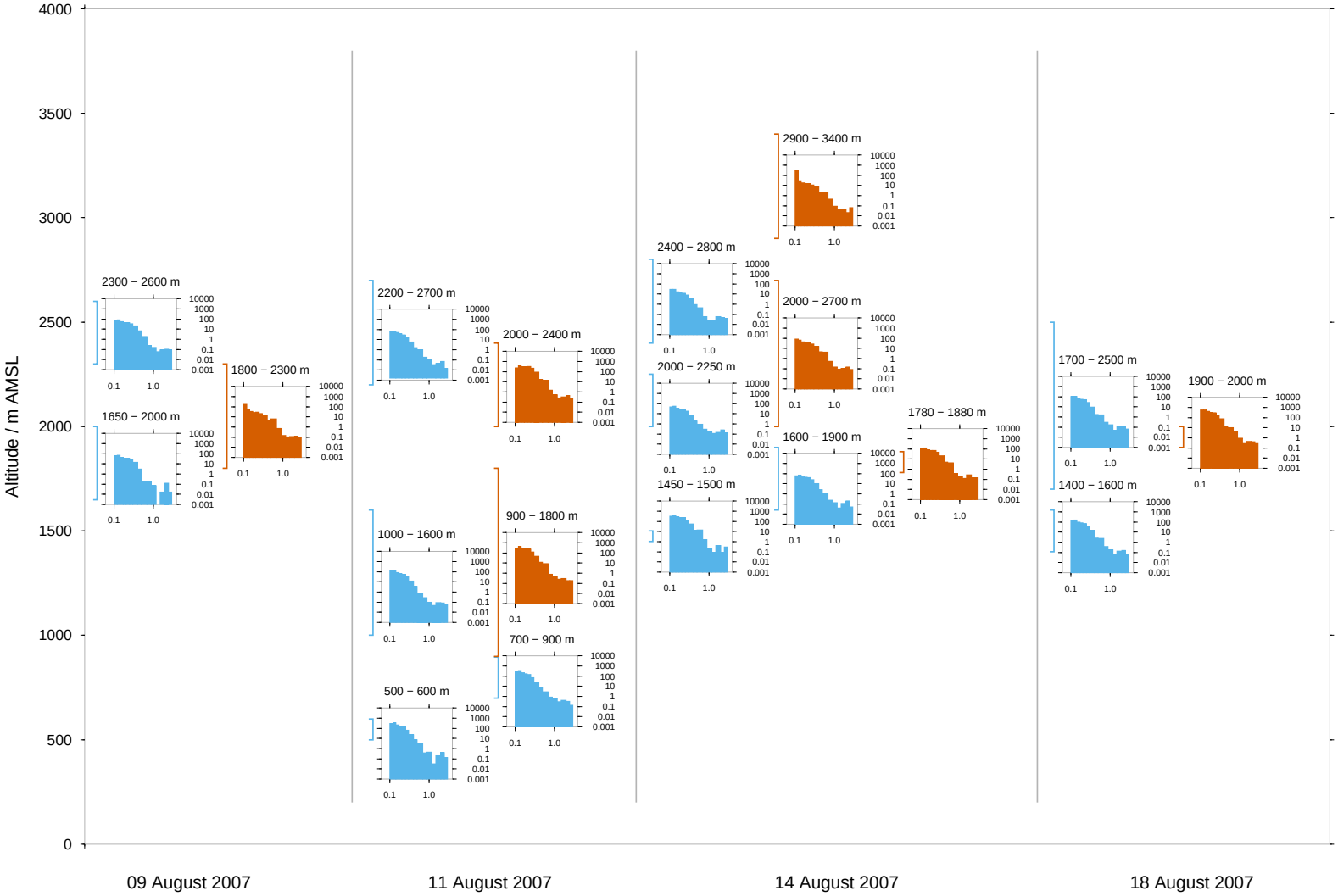


Figure 3.1: A summary of aerosol size spectra from the eight vertical profiles. Size spectrum plots from subsequent figures are reproduced here. Ascending profiles are coloured cyan, descending profiles orange. The rectangular bracket to the left of each size spectrum plot indicates the altitude interval that it represents.

The vertical profile of aerosols appears to consist of an elevated layer of enhanced aerosol number concentration between 2300–2500 metres superimposed on a linearly decreasing profile between the surface and 2700 metres. The temperature profile has three inversions: around 2350m, 2650m and 3600m.

The second profile of aerosol number concentration, $NO_y$ and temperature was measured in a descending holding pattern at a position approximately 40km west of Bela-Bela (formerly known as Warmbaths, also along the Aura track), starting from the cruise altitude of 20000 feet AMSL and descending to 1500 feet above ground. The profile was started at 13:18 UTC and completed at 13:48 UTC. Similar height-bin averaging was performed on the measurements for this profile. This profile is plotted in in Figure 3.2b, The particle size spectrum for the altitude interval from 1800–2300m is presented; above this altitude the PCASP instrument experienced a failure.

The temperature profile has an inversion at 2500m. Aerosol number concentration below this altitude appears to be constant with decreasing altitude. The $NO_y$ profile could be approximiated by a block of constant concentration of about 2 ppb with a layer of enhancement up to 2.5 ppb centred at 2800m, above the inversion.

On 11 August 2007 the flight was planned to track the Aura satellite. The first vertical profile was flown overhead Richards Bay, while climbing from approximately 500m to 6000m above sea level. The profile was started at 11:01 UTC and finished at 11:40 UTC. Profiles of aerosol number concentration, $NO_y$, and ambient temperature are shown in Figure 3.3a. Vertical averaging is in size bins similar to the profiles from 9 August: PCASP number concentration and $NO_y$ are averaged in 50m bins, temperature into 20m bins.

The temperature profile has an consistent decrease in temperature with altitude, with a number of shallow inversions: around 950m, 1800m, 2450m and 2700m. Particle concentration appears to consist of an approximately exponential profile of decreasing number concentration with height, with several layers of enhancement corresponding to inversion layers in the temperature profile. The $NO_y$ profile closely follows the aerosol profile, with enhanced concentrations below the temperature inversions at 950m, 2450m and 2700m.

The second vertical profile was flown overhead Nelspruit, while descending from approximately 6000m AMSL to the surface, before landing at Nelspruit. The profile was started at 12:40 UTC and finished at 13:20 UTC. Profiles of aerosol number concentration, $NO_y$, and ambient temperature are shown

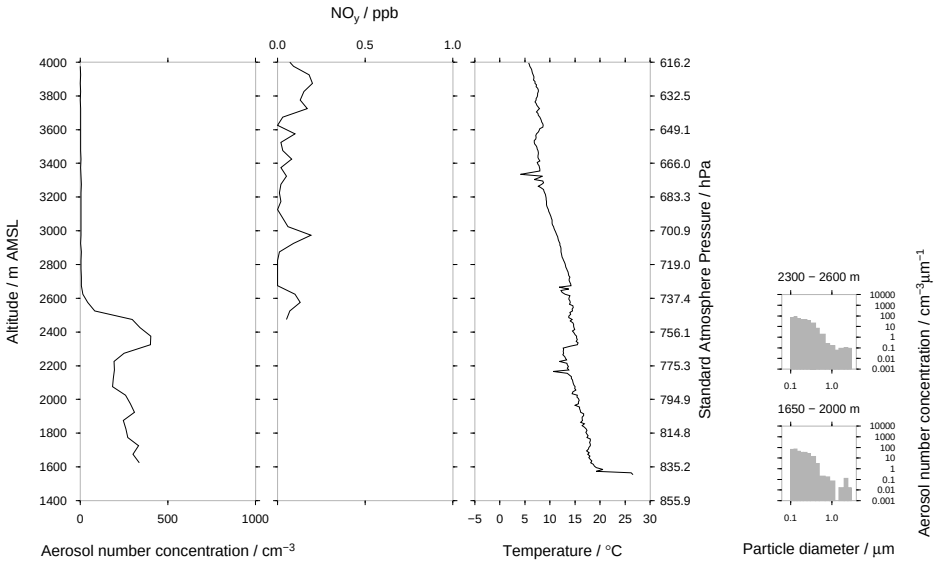


(a) First vertical profile on 9 August 2007, at a position 50km north-east of Bethlehem between 12:01 and 12:25 UTC.

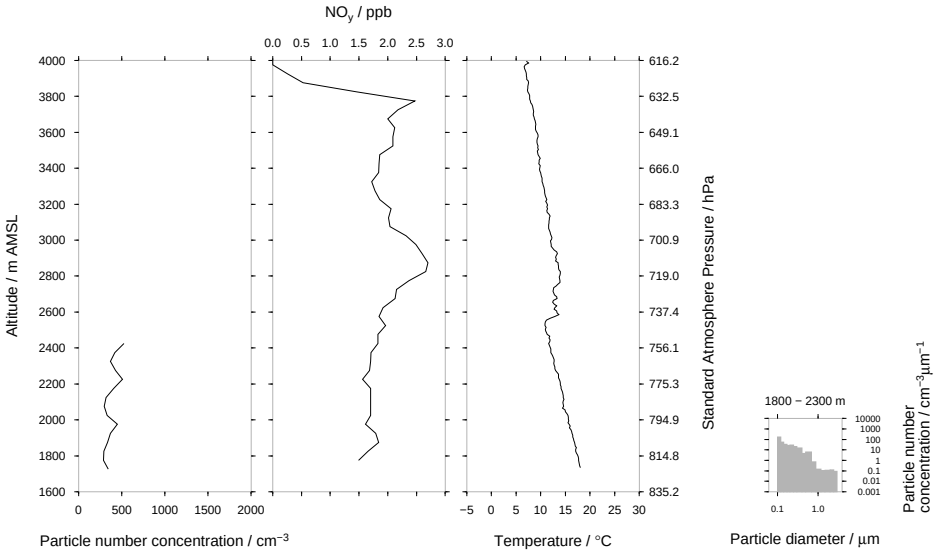


(b) Second vertical profile on 9 August 2007 at a position 40km west of the town of Bela-Bela (Warmbaths) between 13:18 and 13:48 UTC.

Figure 3.2: Plotted against altitude from left to right: Total aerosol number concentration, in-situ $NO_y$ concentration averaged over 50m intervals and ambient temperature averaged over 20m intervals for the vertical profiles on 9 August 2007. Particle size spectra for altitude intervals of interest are plotted on the far right.

in Figure 3.3b. Extremely high values of aerosol number concentration, and values of $NO_y$ up to 35 ppb were measured while descending through smoke plumes from nearby forest fires. A photograph of the upper plume taken from the aircraft is shown in Figure 3.4.

The temperature profile has inversions at 3650m, 2800m and 1800m. The enhanced $NO_y$ and aerosol concentrations in the larger forest fire plume appear to be trapped underneath the inversion at 2800m. The aerosol and trace-gas plumes appear at slightly different heights. This could be as a result of the slower time response of the trace-gas instrument, bearing in mind that the aircraft was descending during this profile. There is a layer of enhanced $NO_y$ and aerosols around 2200m, these were from a second forest-fire plume. Below the inversion at 1800m, $NO_y$ and aerosol concentration is approximately constant.

The flight plan on 14 August 2007 was to track the ENVISAT satellite, to compare the aircraft measurements with SCIAMACHY in the nadir-viewing mode. The first vertical profile was flown at a position approximately 20km south-west of Barberton, while climbing from approximately 500m above ground to 6000m above sea level. The profile was started at 07:15 and complete at 07:52 UTC. Profiles of aerosol number concentration and $NO_y$ are averaged into 50m altitude bins, and ambient temperature in 20m altitude bins, and plotted in Figure 3.5a.

The temperature profile has a deep inversion layer between 2600–2800m below which the aerosols and trace-gases appear to be trapped. There appear to be several enhancements in the trace-gas profile that are more prominent than any corresponding enhancement in the particle number concentration. Both of these quantities show an approximately linear decrease with height. The slight increase in particle number concentration around 2500m may correspond with the $NO_y$ enhancement around 2900m, although given that the aircraft was ascending at 500 feet/min (150 m/min) this would mean that there is more than two minutes difference in response time between the PCASP and the $NO_x$ instrument.

The second vertical profile was flown overhead the town of Estcourt, while descending from approximately 6000m AMSL to 500m above ground. The descent was started at 08:38 and completed at 09:08 UTC. Profiles of aerosol number concentration, $NO_y$, and ambient temperature are shown in Figure 3.5b. The same altitude bins were used for averaging the second profile. The PCASP instrument had failed above 3200m. There are temperature inversions at 3500m, 3050m, 2850m and 1900m. A layer of elevated aerosol number concentration appears to be trapped between the inversions at 3050m

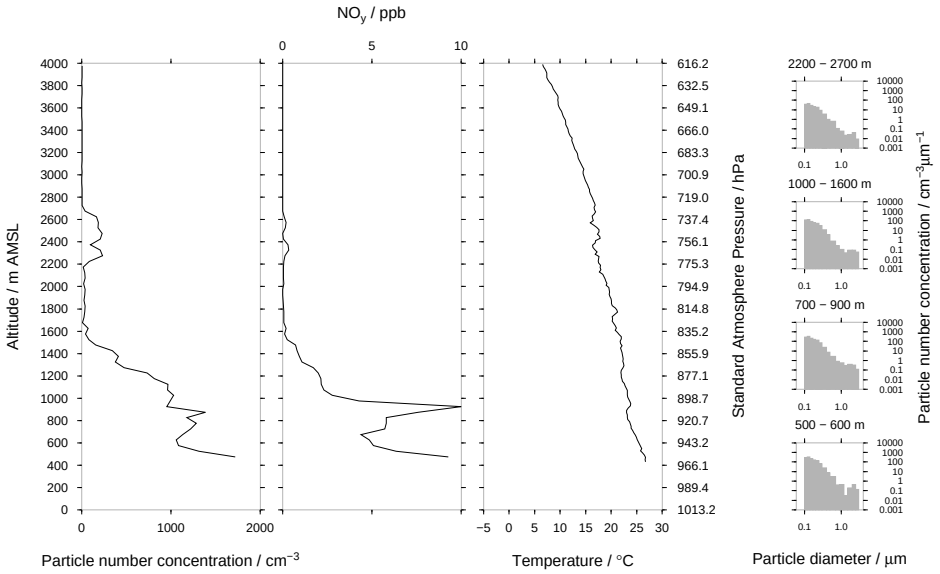


(a) First vertical profile on 11 August 2007 overhead Richards Bay, between 11:01 and 11:40 UTC.

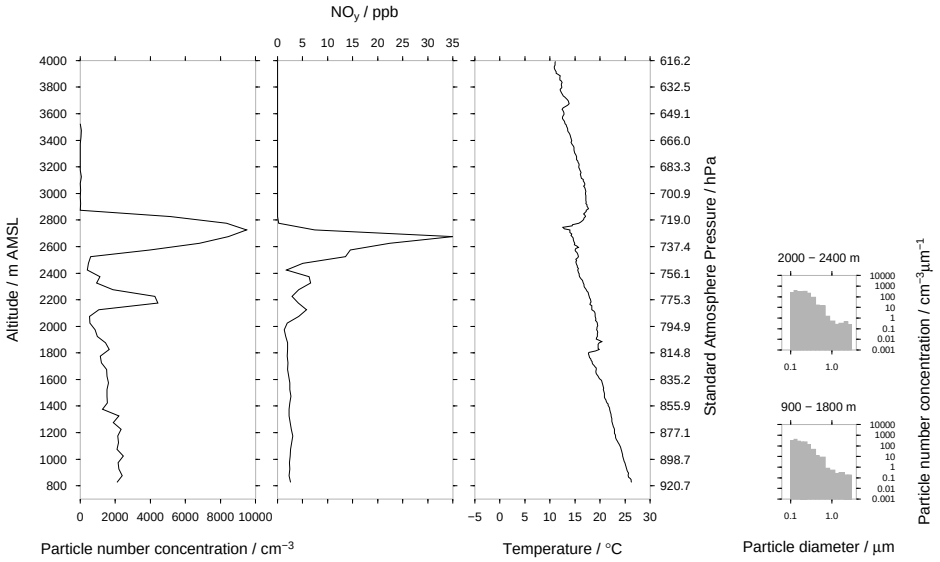


(b) Second vertical profile on 11 August 2007 overhead Nelspruit, between 12:40 and 13:20 UTC. The descent through the forest-fire plume is evident in the particle concentration and $NO_y$ measurements between 2900 m and 2500 m AMSL

Figure 3.3: Plotted against altitude from left to right: PCASP number concentration, in-situ $NO_y$ concentration and ambient temperature on 11 August 2007. Aerosol particle size spectra for altitude intervals of interest are plotted on the far right.

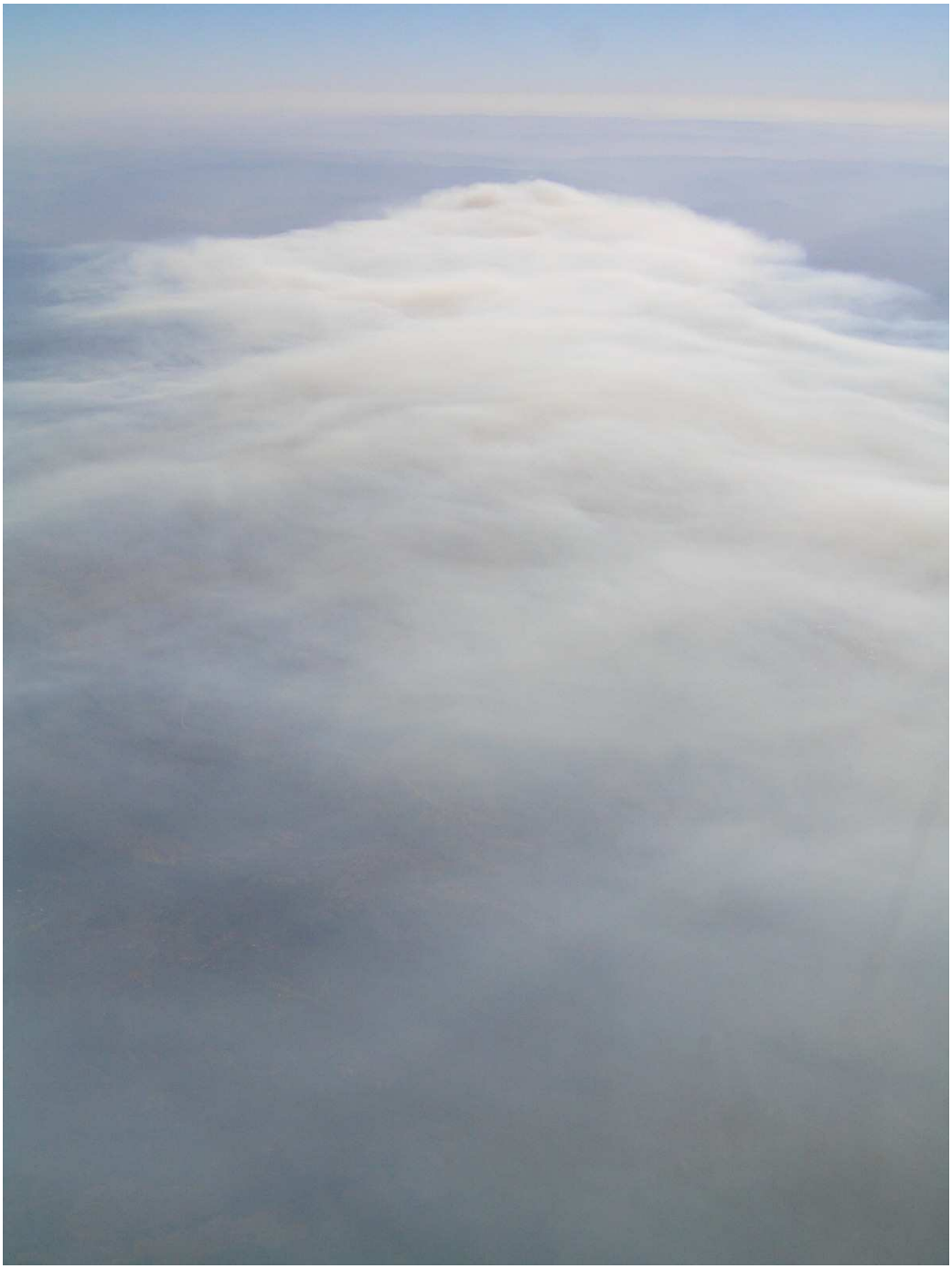

Figure 3.4: A photograph of a large forest fire plume overhead Nelspruit taken from the aircraft on 11 August 2007.

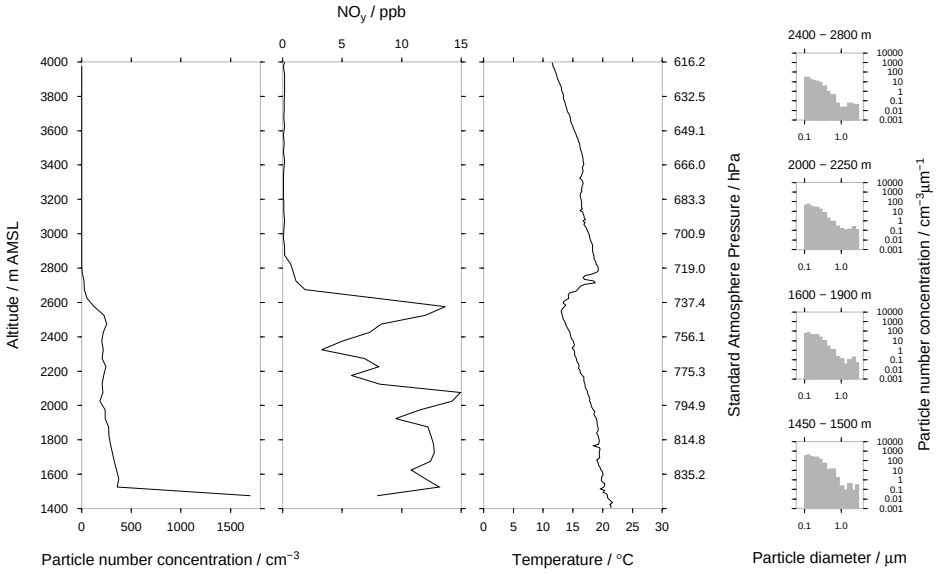


(a) First vertical profile on 14 August 2007 approximately 20km south-west of Barberton, between 07:15 and 07:52 UTC.

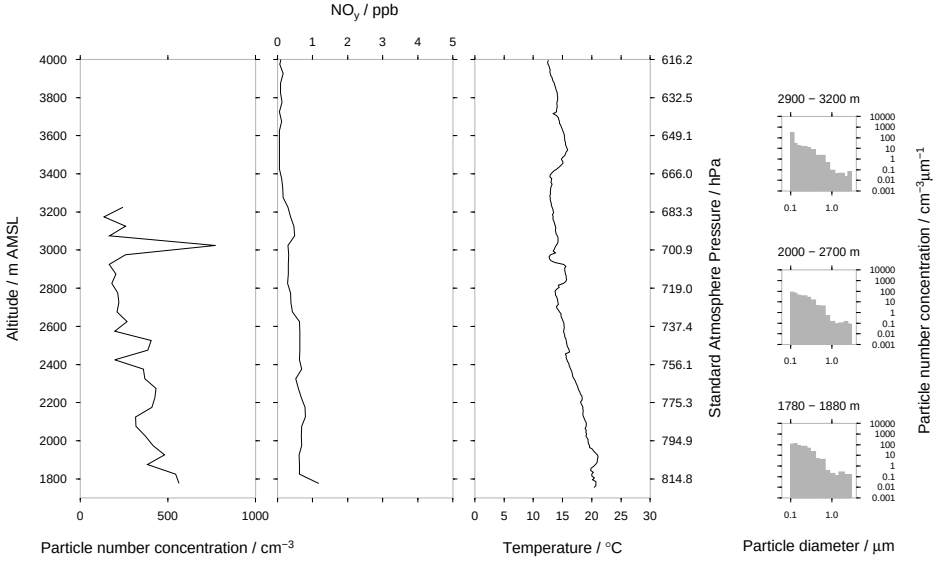


(b) Second vertical profile on 14 August 2007 measured while descending overhead Estcourt, between 08:38 and 09:08 UTC. Above approximately 3400m in this profile the PCASP displays an artefact of extremely high number concentrations.

Figure 3.5: Plotted against altitude from left to right: PCASP number concentration, in-situ $NO_y$ concentration and temperature for the vertical profiles on 14 August 2007. On the far right, particle size spectra for altitude intervals of interest are plotted.

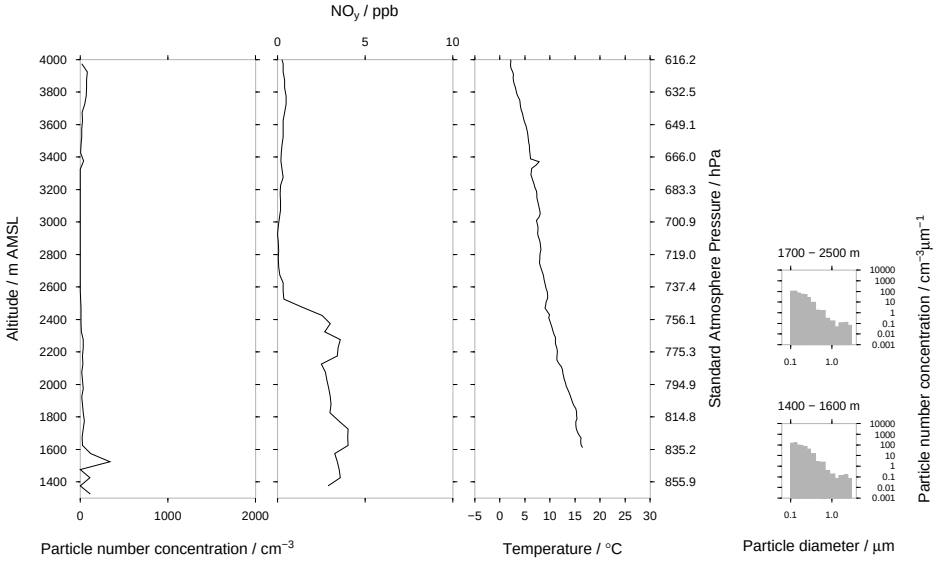


(a) First vertical profile on 18 August 2007 approximately 40km south of Vryheid, between 11:55 and 12:30 UTC.

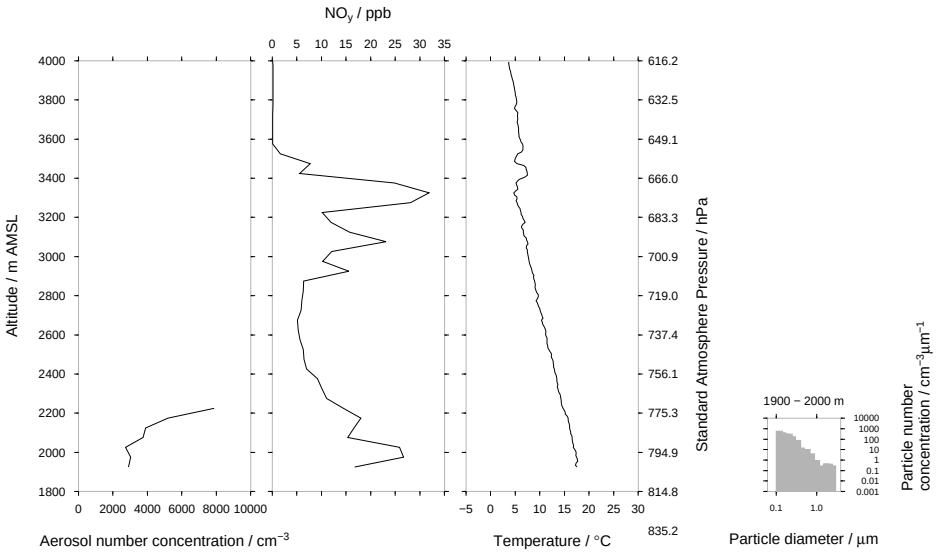


(b) Second vertical profile on 18 August 2007 measured while descending approximately 10 km south of Middelburg, between 13:07 and 13:35 UTC. The particle number concentration between 3800m and 2200m displays an excursion to extremely high values rendering these measurements worthless.

Figure 3.6: Plotted against altitude from left to right: PCASP number concentration, in-situ $NO_y$ concentration and ambient temperature for the vertical profiles on 18 August 2007. Average particle size spectra for vertical intervals of interest are plotted on the far right of the figures.

and 2850m, there does not appear to be a corresponding increase in $NO_y$.

On 18 August 2007, the flight was planned to once again track the Aura satellite. The first vertical profile was flown at a position approximately 40km south of Vryheid, while climbing from approximately 500m above ground to 6000m above sea level. The profile was started at 11:55 UTC and finished at 12:30 UTC. Profiles of aerosol number concentration, $NO_y$, and ambient temperature are shown in Figure 3.5a. The former two parameters are averaged over 50m altitude bins, the latter over 20m altitude bins.

There appears to be an instrument problem below approximately 1600m, with the temperature fixed at 26° C over an altitude range greater than 1000m. There is a small temperature inversion around 3400m with a corresponding layer of slighly increased aerosol and $NO_y$ concentration. Above 1650m, the aerosol counts are very low however the layer of $NO_y$ extends from the surface up to 2500m. The $NO_y$ profile shape appears to be box shaped, with a constant concentration up to the top of the layer.

The second vertical profile was flown at a position approximately 10km south of Middelburg, while descending from approximately 6000m AMSL to 500m above ground. The descent was started at 13:07 UTC and completed at 13:35 UTC. Profiles of aerosol number concentration, $NO_y$, and ambient temperature are shown in Figure 3.5b. Similar vertical averaging was employed.

The temperature profile has a inversions at 3500m and 3400m. Below the lower of these inversions, there is a layer of high $NO_y$ concentration, with peak concentration around 30ppb. There are two more layers below this one, also with enhanced $NO_y$ concentration. The remainder of the trace-gas profile appears to be an exponential decrease with height. The PCASP experienced a failure above 2200m.

The vertical profiles can be characterized by a few different shapes: 1. exponentially decreasing profile with height 2. block-shaped profile up to a certain height 3. linearly decreasing profile with height 4. elevated layers of high trace-gas and aerosol concentration. Combinations of these shapes have been used to design a number of scenarios for radiative transfer modelling.

Table 3.2: The Radiative Transfer Scenarios

| Scenario | $NO_2$ Profile Shape | Aerosol Profile Shape | Surface Elevation |
|---|---|---|---|
| 1 | 1.5 km block | 1.5 km block | 0 km |
| 2 | 3 km block | 3 km block | 0 km |
| 3 | 1.5 km block + EL | 1.5 km + EL | 0 km |
| 4 | 1.5 km block | 1.5 km block | 1.5 km |
| 5 | 1.5 km block + EL | 1.5 km block + EL | 1.5 km |
| 6 | Exponential | Exponential | 0 km |
| 7 | Exponential + EL | Exponential + EL | 0 km |
| 8 | Exponential | Exponential + EL | 0 km |
| 9 | Exponential | Exponential | 1.5 km |
| 10 | Exponential + EL | Exponential + EL | 1.5 km |

## 3.2 Radiative Transfer Modelling

Table 3.2 gives a summary of the initial ten radiative transfer modelling scenarios that were devised for interpretation of the airborne DOAS data. All of the scenarios have a $NO_2$ VCD of 2 $\times 10^{16}$ molecules.cm$^{-2}$ and an aerosol optical thickness of 0.5. The elevated layers (designated in the table as EL) are situated between 2.2 km and 2.4 km above the surface. Exponential profile shapes have a constant scale height of 600m.

The first group of scenarios (Scenarios 1 to 5, shown in Figure 3.7) have a constant $NO_2$ VMR in an altitude block up to 1500m above the surface in the case of Scenarios 1, 3, 4 and 5, and up to 3000m above the surface for Scenario 2. This might occur on a day with an unstable, well mixed PBL. Scenario 1's $NO_2$ VMR is $5.63\times10^{-9}$ and that of Scenario 2 is $3.02\times10^{-9}$. Owing to the exponential decrease in atmospheric pressure and hence total molecules per volume with altitude, the contribution to the integrated column made by elevated trace gases at a given mixing ratio is less. This is why the VMR in Scenario 2 is more than half that of Scenario 1. Since aerosols are measured as a number concentration, no such altitude effect occurs and the extinction coefficient for Scenario 1 (0.333 km$^{-2}$) is twice that of Scenario 2 (0.166 km$^{-1}$).

Sensitivity of the air-mass factor to changes in solar zenith angle and surface albedo for these scenarios is shown Figure 3.7. There is a general trend of increasing air-mass factor with increases in surface albedo and solar zenith angle across all of the block-profile scenarios. These effects are to be expected:

as the surface becomes more reflective, more light is reflected back to the sensor, and hence the measurement becomes more sensitive. Increasing air-mass factor with solar zenith angle is to be expected based on a simple geometric consideration. Changes in air-mass factor with view angle of up to five percent were also found, but for clarity are not depicted in the figure.

Examining Scenarios 1 and 2, an increase in air-mass factor of up to 31 percent with a doubling of PBL height is found. At a surface albedo of 0.02 and solar zenith angle of 35°, the change in air-mass factor increases from 0.93 under Scenario 1 to 1.22 under Scenario 2, an increase of 31 percent. At a SZA of 60°, air-mass factors are 1.26 and 1.57 for Scenarios 1 and 2; an increase of 29 percent. With a higher surface albedo of 0.10 the change in air-mass factor at 35° SZA is from 1.49 to 1.71, approximately 15 percent increase. At 60° SZA, the air-mass factor increases from 1.78 to 2.04, a 14 percent increase. These increases in air-mass factor with increasing boundary layer depth are consistent with increases reported by Leitao *et al.* (2010). Relative changes in air-mass factor with increasing surface albedo are consistent across changes in SZA.

Scenario 3 is similar to Scenario 1, with the addition of an elevated layer of $NO_2$ and aerosols between 2200 and 2400 metres. The VMR and aerosol number concentration (and hence extinction coefficient) in the elevated layer was assumed to be one fifth of that in the lower block of the profile. This results in an $NO_2$ VMR of $5.50\times10^{-9}$ and an extinction coefficient of 0.332 $km^{-1}$ in the lower block. VMR and extinction coefficients in the elevated layer are $1.37\times10^{-9}$ and 0.066 $km^{-1}$ respectively.

Addition of an elevated layer to the block profile of $NO_2$ and aerosols leads to a dramatic reduction of the air-mass factor. At a surface albedo and SZA of 0.02 and 35° respectively, the air-mass factor decreases from 0.93 for Scenario 1 to 0.39 for Scenario 3, a decrease of 58 percent. At a higher solar zenith angle of 60°, the change in air-mass factor is from 1.26 for Scenario 1 to 0.52 for Scenario 3, a 59 percent decrease. With a more reflective surface (albedo 0.10), the change in air-mass factor is from 1.49 to 0.76 (49 percent decrease) at low SZA. This is to be expected: a more reflective surface will make the scattering in the elevated layer less important. At a solar zenith angle of 60°, air-mass factor changes from 1.78 under Scenario 1 to 0.82 under Scenario 3, a decrease of 54 percent. Under Scenario 3 the sensitivity of the air-mass factor to changing solar zenith angle decreases with increasing surface albedo.

Scenarios 4 and 5 are similar to Scenarios 1 and 3, respectively, however the terrain elevation is set at 1500m. Surface $NO_2$ VMR for Scenario 4 is $6.53\times10^{-9}$ and for Scenario 5, $6.38\times10^{-9}$. Comparing Scenarios 1 and 4, a

general increase in air-mass factor is found with increasing terrain elevation. At low SZA (35°) and low surface albedo (0.02), air-mass factor increases from 0.93 to 1.10 (18 percent) when the terrain height is increased to 1500m. At 60° solar zenith angle the change in air-mass factor with the change in surface elevation is from 1.26 to 1.45 (15 percent). With a higher surface albedo of 0.10, the change in air-mass factor is from 1.49 to 1.66 at SZA 35° (11 percent increase), and from 1.78 to 1.99 at an SZA of 60° (12 percent increase).

Air-mass factors for Scenario 5 are greater than those for Scenario 3. At low surface albedo (0.02) and low solar zenith angle (35°), air-mass factor increases from 0.39 under Scenario 3 to 1.02 under Scenario 5, an increase of 162 percent. Still at low surface albedo but at 60° SZA, air-mass factor increases from 0.52 to 1.39 with the surface elevation change from Scenario 3 to 5, again a dramatic increase of 167 percent. With surface albedo set to 0.10, at SZA of 35° the air-mass factor increases from 0.76 to 1.60 (111 percent) when moving from Scenario 3 to Scenario 5. At high solar zenith angle and high surface albedo the air-mass factor increases from 0.82 to 1.94 (137 percent) when moving from Scenario 3 to Scenario 5

Comparing Scenarios 4 and 5, the decrease in air-mass factor brought about by an elevated layer is less dramatic when the terrain elevation is higher. At 35° solar zenith angle and surface albedo 0.02, the air-mass factor decreases by seven percent from 1.10 to 1.02. With a higher solar zenith angle of 60°, the decrease is from 1.45 to 1.39 (4 percent). With a higher surface albedo of 0.10, decreases in air-mass factor of 4 percent (from 1.66 to 1.60) at low SZA, and 3 percent (from 1.99 to 1.94) at 60° SZA are found.

Scenarios 6 and 7, depicted in Figure 3.8, have an exponentially decreasing profile of $NO_2$ and extinction coefficient with a scale height of 600m. This might occur on a day with a more stable PBL, concentrating the $NO_2$ and aerosols close to surface sources. Scenario 7 differs with the addition of an elevated layer, between 2200 and 2400 metres, of enhanced $NO_2$ and aerosol extinction. The enhancements of $NO_2$ and aerosol extinction over the exponential profile are set at 1.37e-9 and 0.066 $km^{-1}$ respectively, similar to the layer in Scenario 3. Surface $NO_2$ mixing ratio for both of these scenarios is $8.62\times10^{-9}$. The expected decrease in the surface concentration required to maintain the $NO_2$ column at $2\times10^{16}$ molecules.$cm^{-2}$ resulting from the addition of the elevated layer is neglible.

Scenario 6 is unusual in that no sensitivity of air-mass factor to surface albedo is found. Increasing the terrain elevation to 1500m (Scenario 9), while keeping a similar exponential profile restores the effects seen with the

box profiles. Comparing Scenarios 1 and 6 shows that the effect of a change in profile shape depends on the surface albedo. With a surface albedo of 0.02, air-mass factor increases by 53 percent from 0.93 to 1.42 at 35° SZA and by 36 percent from 1.26 to 1.71 at 60° SZA. Increasing the surface albedo to 0.10 reverses the trend, with decreases in air-mass factor from 1.49 to 1.42 (5 percent) at 35° SZA and from 1.78 to 1.71 (4 percent) at 60° SZA.

Comparing Scenarios 6 and 7 with surface albedo of 0.02, a general decrease in air-mass factor with the addition of the elevated layer. With a higher surface albedo of 0.10 air-mass factors tend to increase when the elevated layer is introduced into the model.

Scenario 8 has the exponentially-decreasing $NO_2$ profile from Scenario 6 and the aerosol extinction profile of Scenario 7 (exponential decrease with an elevated layer). Comparing Scenarios 7 and 8 with Scenario 6, the changes in air-mass factor between the pure exponential profile and that with the elevated layer would appear to be influenced more by the aerosols in the elevated layer than by the trace gas in the layer.

Scenarios 9 and 10 are similar to Scenarios 6 and 7; however the terrain elevation is set at 1500m. Surface $NO_2$ VMR for both scenarios is $16.1\times10^{-9}$. The presence of an elevated layer changes the AMF, most significantly with a low surface albedo and low SZA, by up to 50 percent. Increasing the terrain height with an exponential profile of $NO_2$ and aerosols in general increases the air-mass factor. Comparing Scenario 6 and 9, the change is dependent on the surface albedo with a decrease in air-mass factor at low surface albedo and an increase at high surface albedo.

A general increase in air-mass factor with terrain elevation is evident between Scenarios 7 and 10, both of which are an exponential profile of $NO_2$ and aerosols with an elevated layer between 2200m and 2400m above the surface. At a surface albedo of 0.02 and SZA of 35°, the air-mass factor increases by 103 percent from 1.09 to 2.21 with the increased terrain elevation of Scenario 10. With a higher SZA of 60°, the increase from 1.41 to 1.96 (39 percent) is less dramatic. A higher surface albedo of 0.10 results in increases of 65 percent (1.62 to 2.67) and 32 percent (1.91 to 2.53), when moving from Scenario 7 to Scenario 10, at solar zenith angles of 35° and 60° respectively.

Scenarios 4 and 5, 9 and 10 are the most relevant to measurements over the Highveld: the terrain elevation is high (between 1000 and 1600m) and, particularly in winter, there is in all probability an elevated layer of trace gases and aerosols present from subcontinental-scale recirculation. Changes in air-mass factor between Scenarios 4, 5 and 9 are relatively small, all ex-

hibiting similar trends with changes in SZA and surface albedo. The presence of an elevated layer of $NO_2$ and aerosols in the context of an exponentially decreasing profile (i.e. Scenario 10), a situation typical of winter, may lead to over-estimation of the vertical column density from the use of an air-mass factor that is too low. The error in the AMF if the elevated layer is neglected is up to 50 percent. For the purpose of having a representative air-mass factor for the aircraft measurements over the Highveld, two values of 1.6 (based on Scenarios 4, 5 and 9) and 2.5 (based on Scenario 10) have been used.

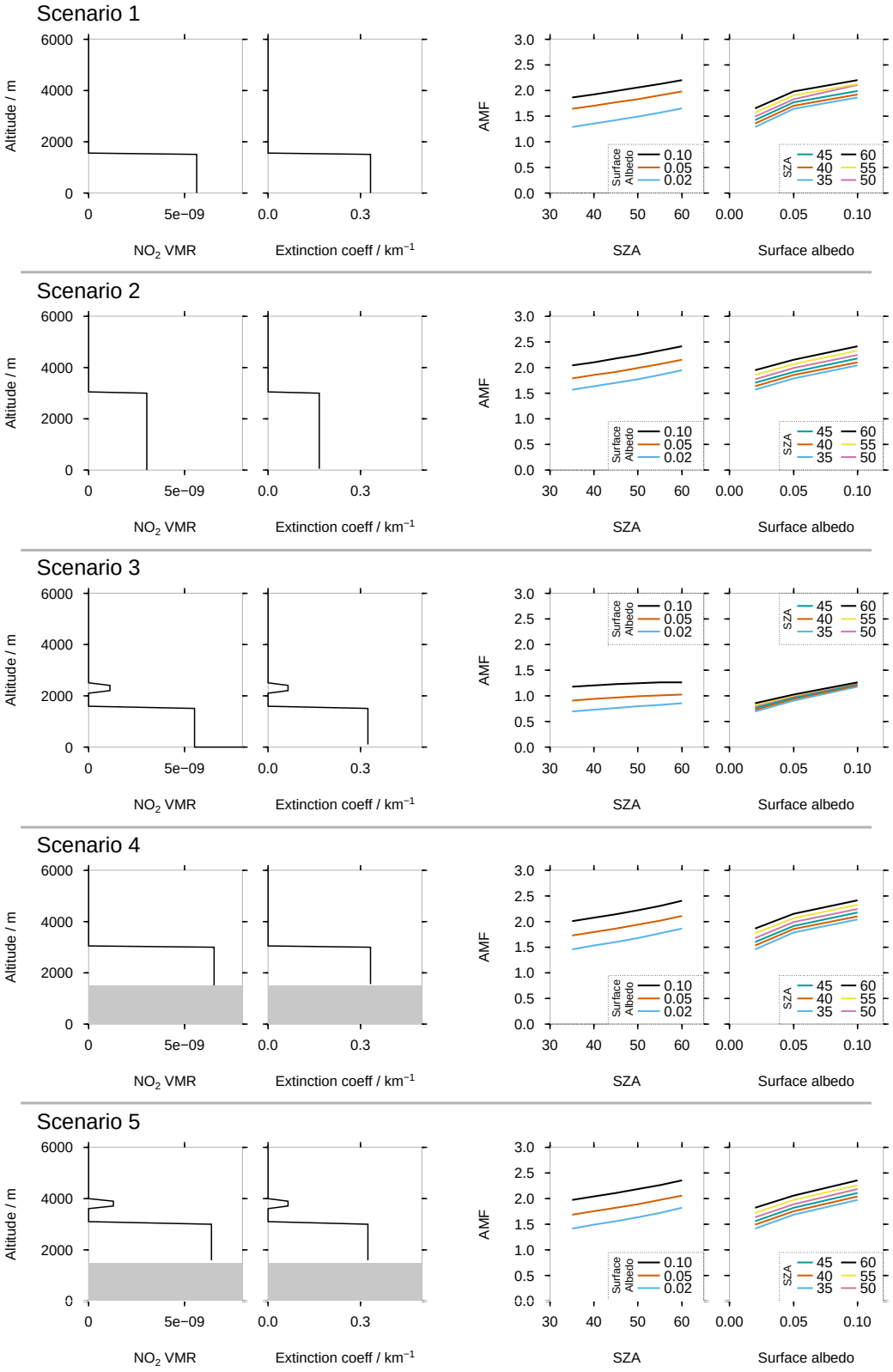


Figure 3.7: Grapical depiction of the profile shapes for model Scenarios 1 to 5, as well as the AMF calculated for three surface albedos and a range of solar zenith angles.

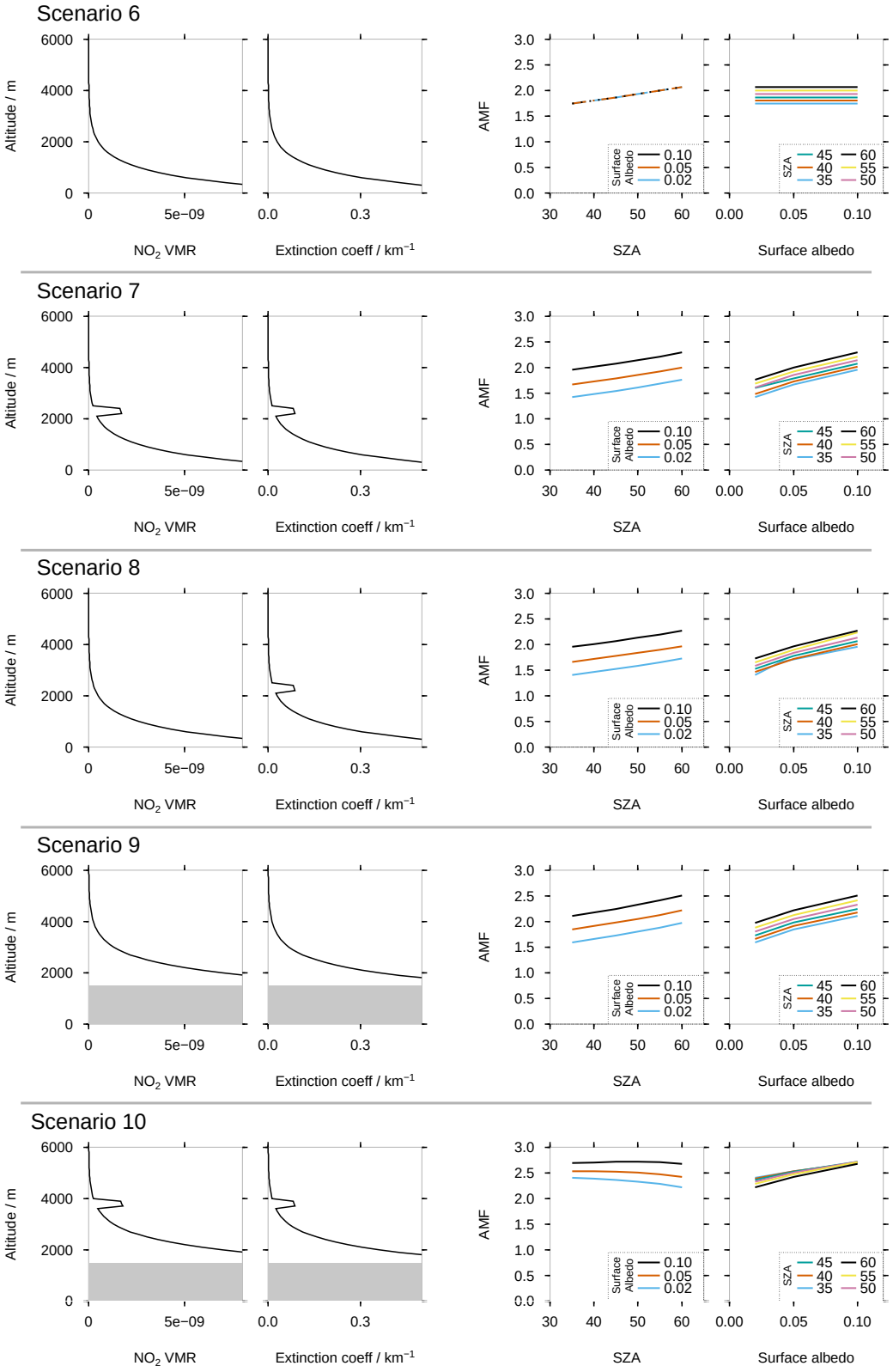


Figure 3.8: Grapical depiction of the profile shapes for model Scenarios 6 to 10, as well as the AMF calculated for three surface albedos and a range of solar zenith angles.

## 3.3 Regional Mapping of $NO_2$

On 5 October 2006, the aircraft took off from Bethlehem at 09:29 UTC and approached the Eastern Highveld from the south, passing to the east of Secunda shortly after 10:00 UTC. A simple mapping pattern was flown flying nominally magnetic north- and south-bound legs, avoiding the busy airspace around Johannesburg. Some adjustments were made to ensure that the flight path passed downwind of major point sources, including Kendal, Matla, Kriel, Tutuka and Duvha power stations. Following this a zig-zag pattern across the estimated plume position of Tutuka power station was flown, before returning to Bethlehem. The complete flight track is shown in Figure 3.9.

The concept of flux estimations presented by Heue *et al.* (2008*a*) can be extended to a regional scale. Nadir $NO_2$ vertical column densities were calculated using an air-mass factor of 1.6, these are plotted along the flight track in Figure 3.10. Inspection of this Figure allows one to distinguish plumes from individual facilities in the case of Sasol Secunda and Tutuka power station; and the combined plume of the greater Johannesburg city and Kendal, Matla and Kriel power stations.

A time-series of $NO_2$ vertical column densities is shown in Figure 3.11. An estimate of the local winds (300°, 4.5 m/s) was made based on the weather station at Kendal power station, and this wind was used to calculate the emission fluxes in each of the distinct plumes in Figure 3.10, using the technique described in Section 2.1.3. These estimated emission fluxes are shown in Figure 3.11.

The plumes from Sasol's Secunda plant, and from Tutuka power station were crossed several times during this flight. Distances downwind of each plume crossing are estimated and plotted against the estimated fluxes in Figure 3.12. Advection time downwind is estimated from the distances based on a wind speed of 4.5 m/s. It is interesting to note that the flux estimated from Sasol Secunda is significantly larger than that from Tutuka power station. Ten kilometers downwind, the fluxes from these two sources are approximately 36 tph and 10 tph respectively. This is expected, since Secunda generates power on-site, as well as being a petrochemical plant.

It is interesting to note that the estimated flux of $NO_2$ in each plume decreases, in contrast what is found close to the point of emission (Figure 1.14b on page 1.14b). This is also in stark contrast to the assumption made by Collett *et al.* (2010) that the dominant process occuring on a regional scale is the conversion of NO to $NO_2$. It is tempting to make a simple model of a

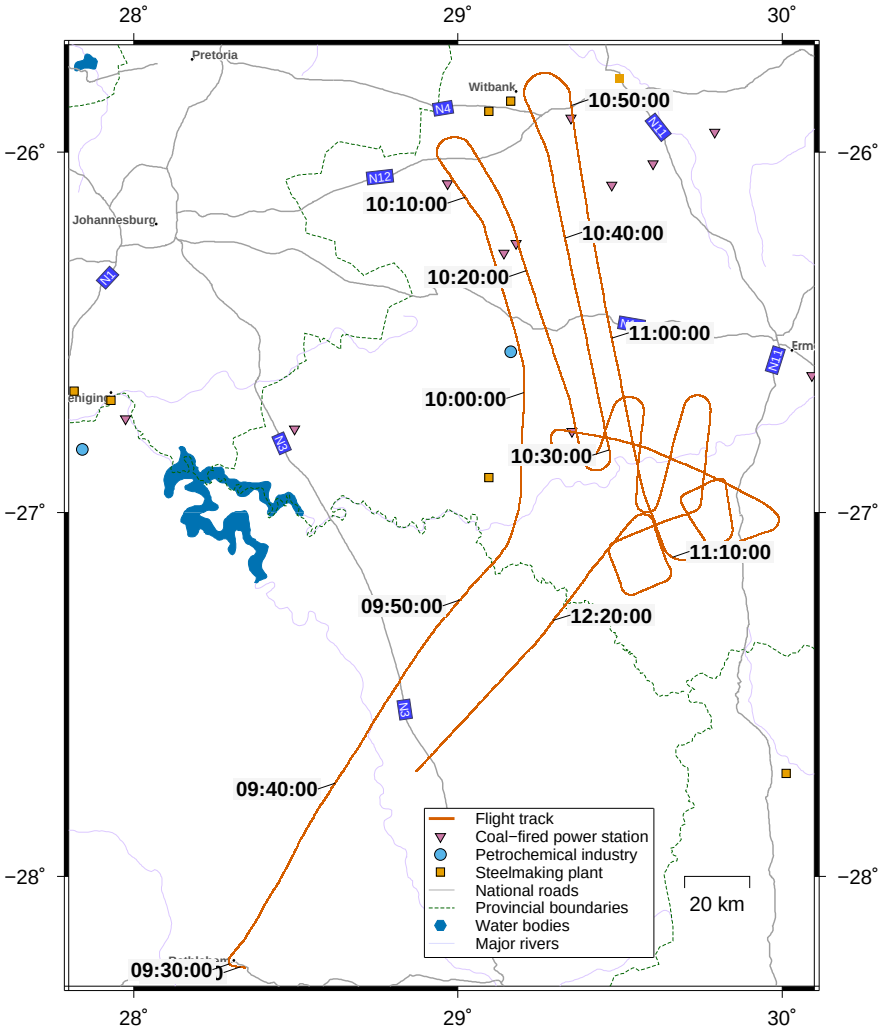


Figure 3.9: The complete flight track for the flight on 5 October 2006.

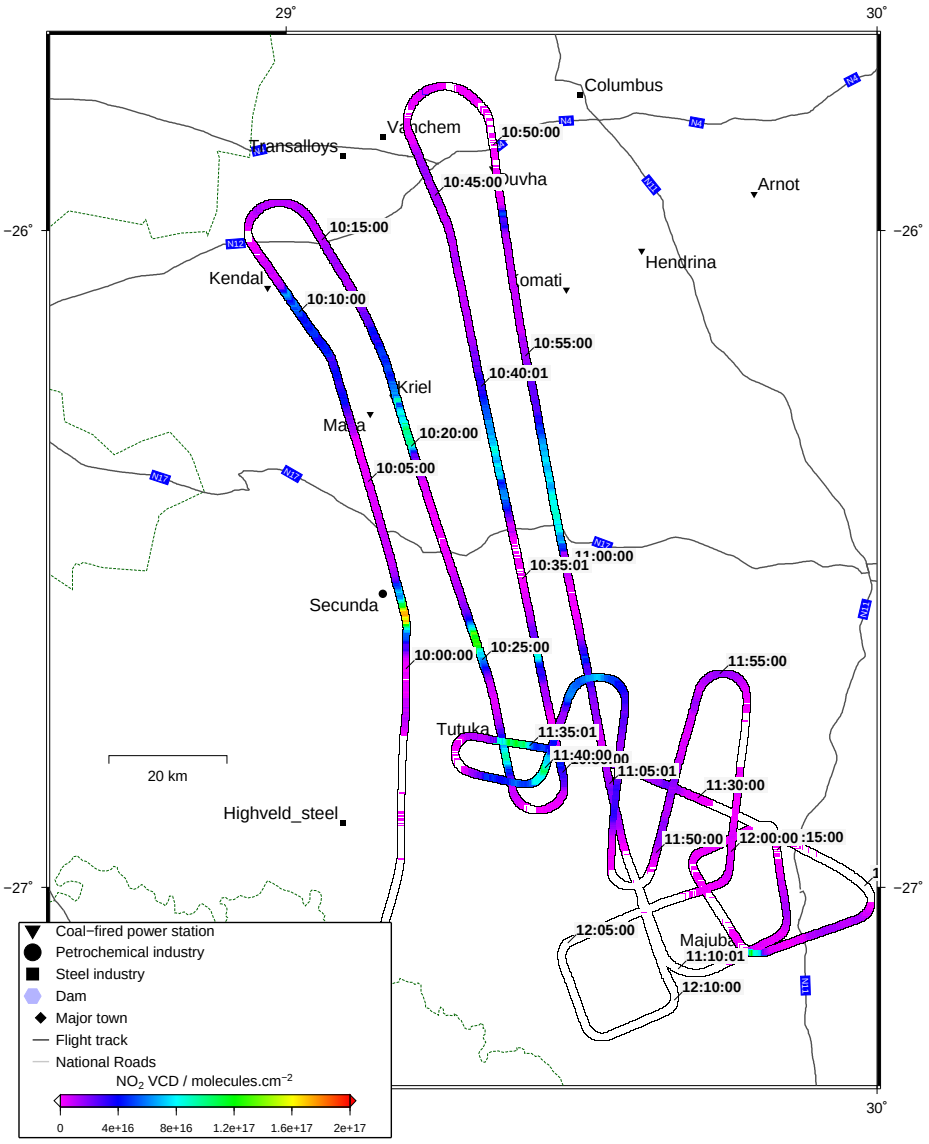


Figure 3.10: $NO_2$ vertical column densities plotted for the flight on 5 October 2006.

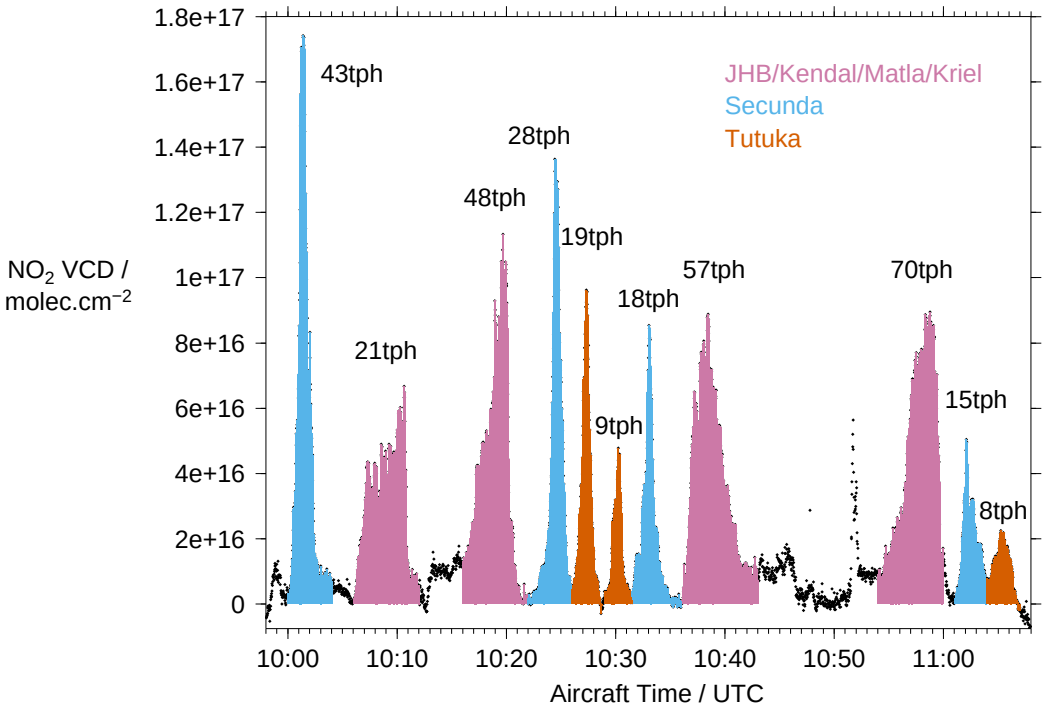


Figure 3.11: $NO_2$ vertical column densities plotted as a time-series for the flight on 5 October 2006. Plume crossings are assigned to sources by inspection of Figure 3.10. Estimates of $NO_2$ flux are shown for each plume.

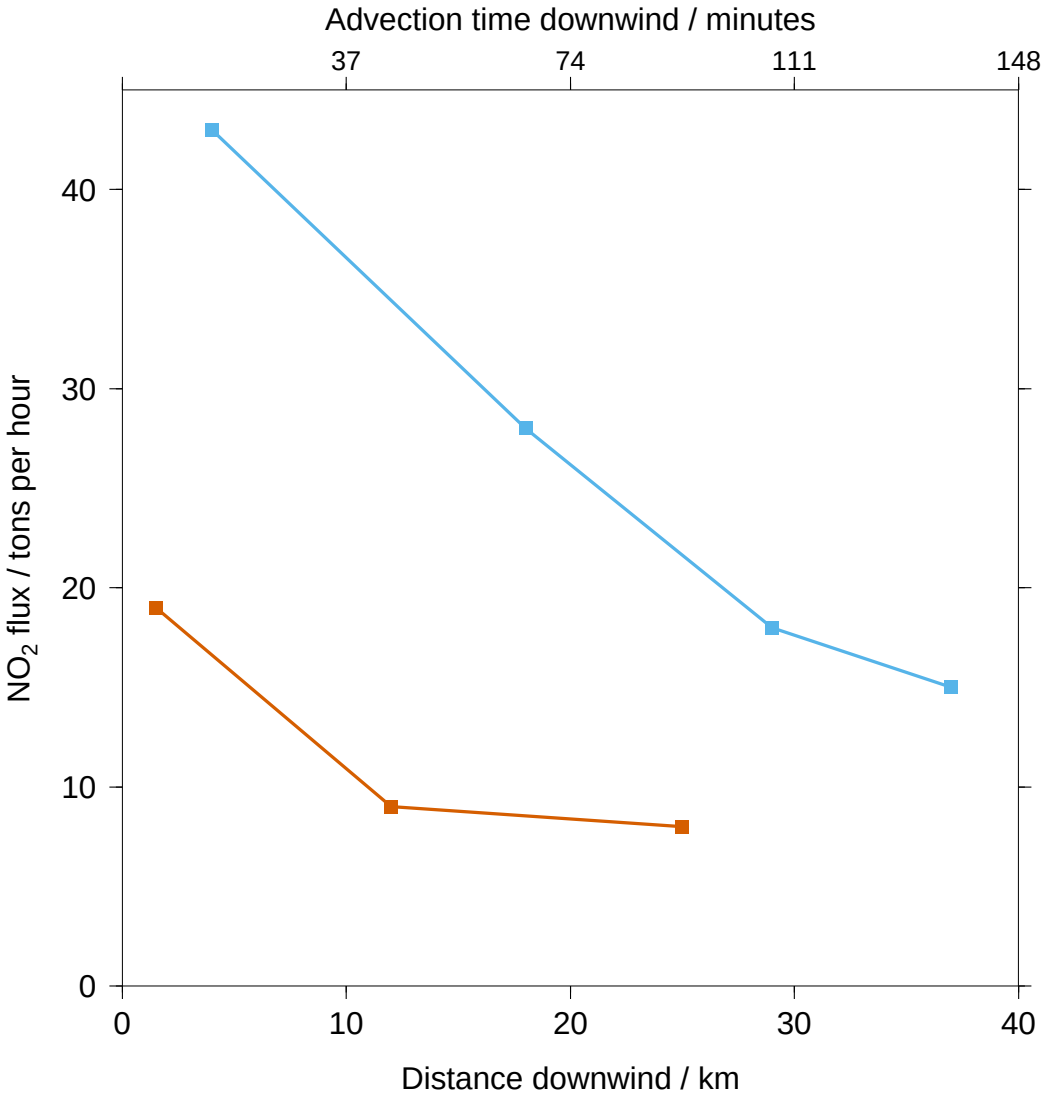


Figure 3.12: Estimates of $NO_2$ flux for the plumes from Secunda (in cyan) and Tutuka (in orange), plotted against estimated downwind distance and advection time.

plume (treating it as a plug-flow reactor (Rawlings and Ekerdt 2002)), to try to infer reaction rates, however the airborne DOAS does not allow us to measure other nitrogen species of interest, or other species that may participate in the reactions. Since there are several chemical pathways for $NO_2$ to be either removed from the atmosphere or convert to a different gaseous nitrogen species, having measurements of only $NO_2$ will make such a calculation under-determined.

The emission flux from the combined plume of Johannesburg, and the three power stations (Kendal, Matla, Kriel), is difficult to interpret: by the time the aircraft measured the Johannesburg plume, it had already advected a considerable distance downwind, and it is likely that the some of the $NO_2$ would have reacted. Fresh $NO_2$ would be added to the measured plume by Kendal, that can be seen as a peak towards the end of the plume crossing at 10:11 UTC. The second crossing of the plume has more $NO_2$ added by Matla and Kriel power stations bringing the total estimated flux to 48 tons per hour. The flux estimated from the third crossing is greater, at 57 tons per hour, and the fourth crossing even greater (70 tons per hour). It does not appear that there are any significant sources adding $NO_2$ to this plume between these crossings, and the increase in $NO_2$ flux, in contrast to the decrease seen from Secunda and Tutuka, is difficult to explain. From the time-series and the flight track it is also clear that there is an unidentified source to the South-West of Duvha power station whose plume was measured at 10:52 UTC.

## 3.4 Satellite Comparisons

The flight track of 9 August 2007 took the aircraft overhead O.R. Tambo International Airport. Takeoff from Bethlehem was at 11:54 UTC, proceeding to a point east of Bethlehem along the predicted Aura track. At this position a vertical profile to 19000 feet AMSL was done before setting course along the satellite track. The satellite overtook the aircraft slightly before this time, at 12:05 UTC. The aircraft proceeded along the predicted satellite nadir track, passing over O.R. Tambo Airport east of Johannesburg. At a position along this track approximately one hundred kilometres north of Pretoria, another vertical profile was done from cruise altitude down to approximately 300m (1500 feet) above ground. The aircraft then routed back to Bethlehem, landing at 15:03 UTC. The complete flight track is shown in Figure 3.13.

A direct comparison between the $NO_2$ vertical columns measured by the airborne DOAS (with AMF=2.5) and the DOMINO tropospheric $NO_2$ product is made in Figure 3.14. Since both the satellite and aircraft measurements are snap-shots of the atmosphere taken at slightly different times, one cannot expect a perfect match. However, the general features of increased $NO_2$ downwind of the Vaal Triangle (around Vanderbijlpark and Vereeniging), and downwind of Johannesburg city are captured by both the aircraft and the satellite.

Smaller scale features that the aircraft measured over Johannesburg around 12:54 were not captured by the satellite, which passed over the same area around 12:07. This is expected, given the much larger ground pixel size of OMI.

A time-series of the aircraft $NO_2$ VCD calculated with air-mass factors of 1.6 and 2.5 is shown in Figure 3.15. For comparison, OMI $NO_2$ VCD is shown, for the pixel at aircraft nadir (orange) and for the pixel to the East of aircraft nadir (i.e. upwind, plotted in blue-green). At times the aircraft was routing close to the boundary between two satellite pixels, and a comparison with the neighboring pixel may be more appropriate.

There is close agreement between the aircraft measurement and the OMI product, particularly in areas of low VCD in the portions of the flight track to the south and north of greater Johannesburg, and also downwind of the Vaal Triangle. Using an air-mass factor of 2.5 (appropriate to RTM Scenario 10) brings the magnitude of the aircraft measurement into good qualitative agreement with the satellite. At 12:45 UTC, upwind abeam Grootvlei power station, there is a small peak in the $NO_2$ measured by the aircraft: around $1\times10^{16}$ molecules.cm$^{-2}$. At this same position the satellite measurement both

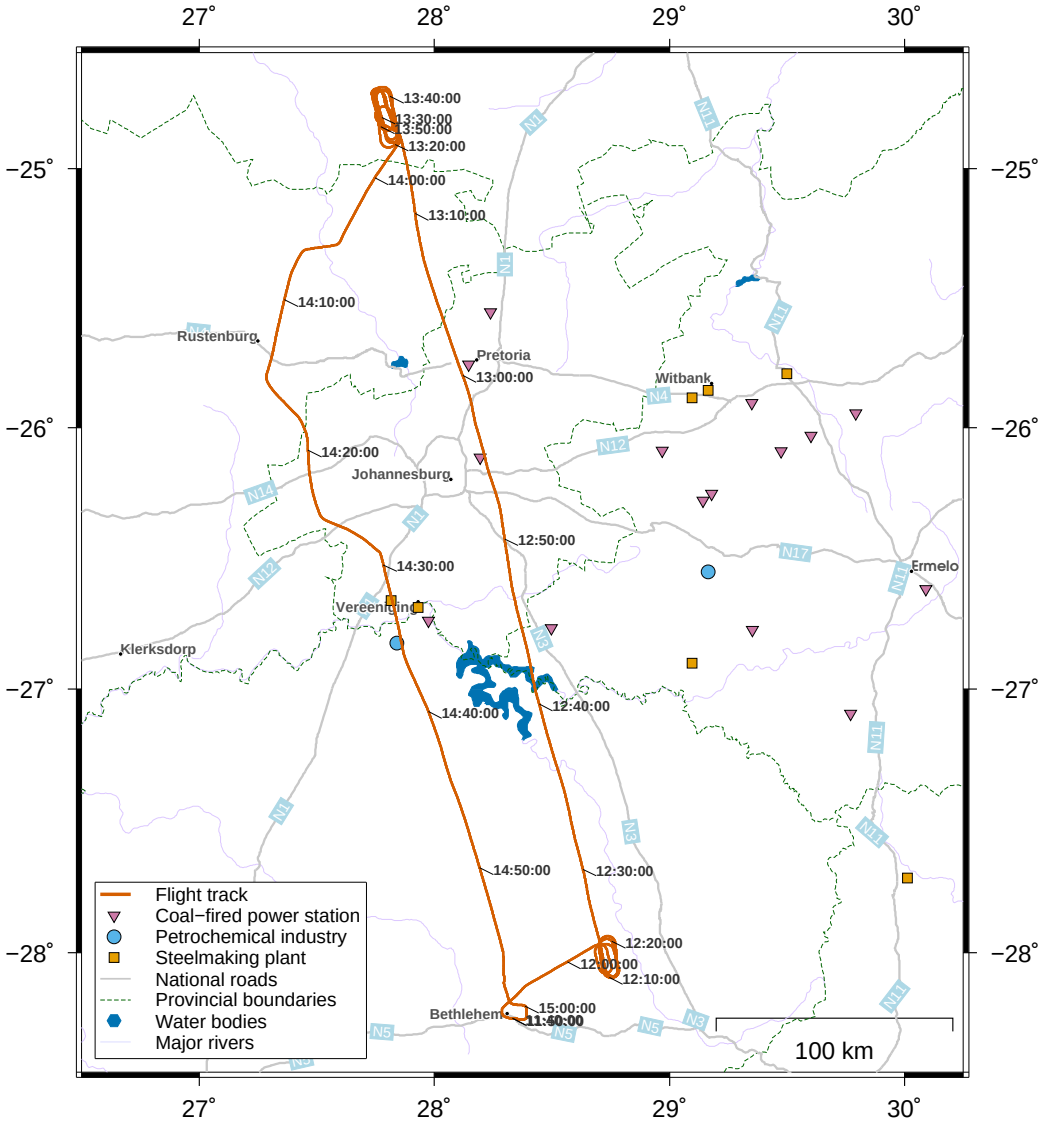


Figure 3.13: The complete flight track for the flight on 9 August 2007.

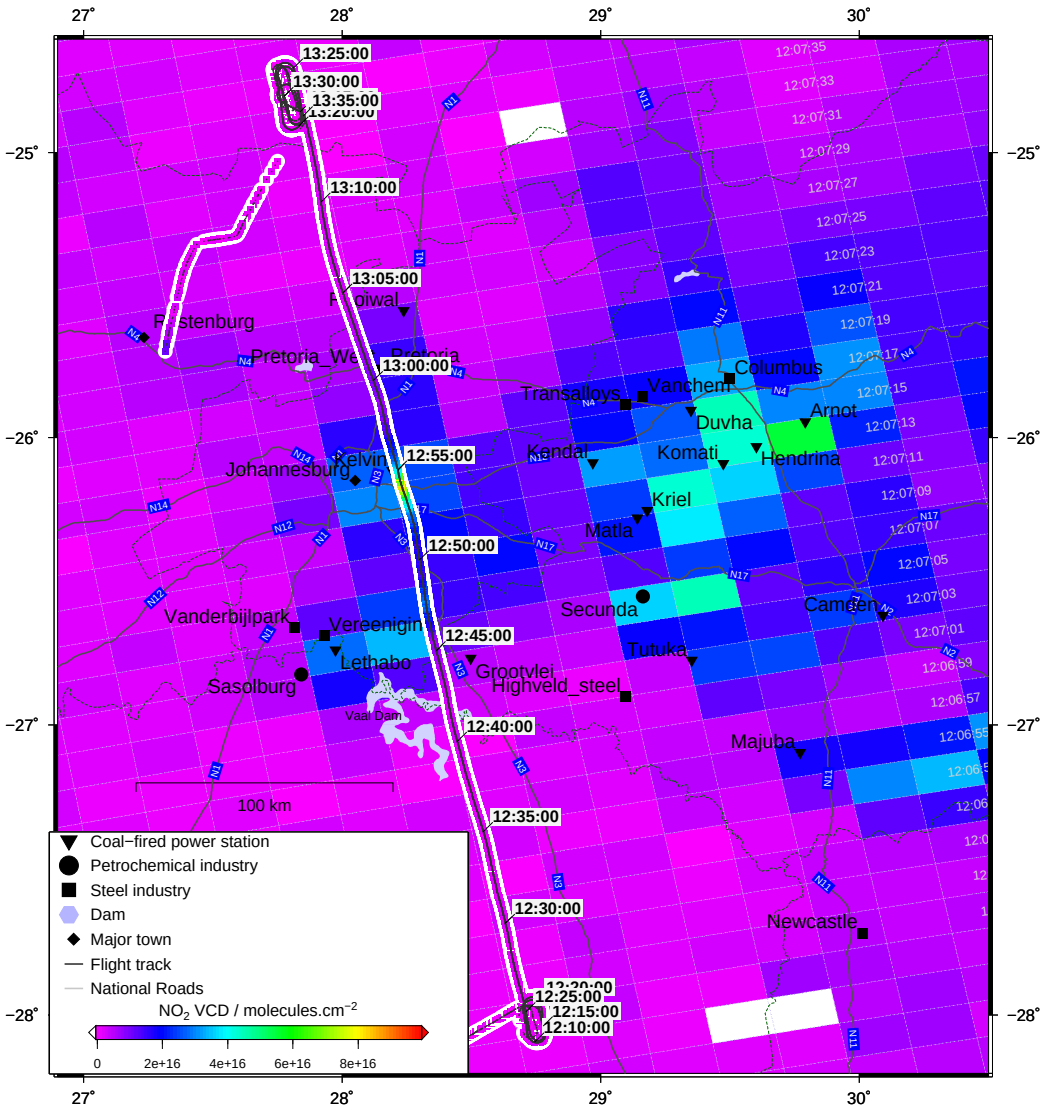


Figure 3.14: A comparison of the airborne DOAS $NO_2$ vertical column densities with DOMINO $NO_2$ from OMI on 9 August 2007. UTC aircraft time is indicated every five minutes along the flight track, UTC satellite time is shown for each data row.

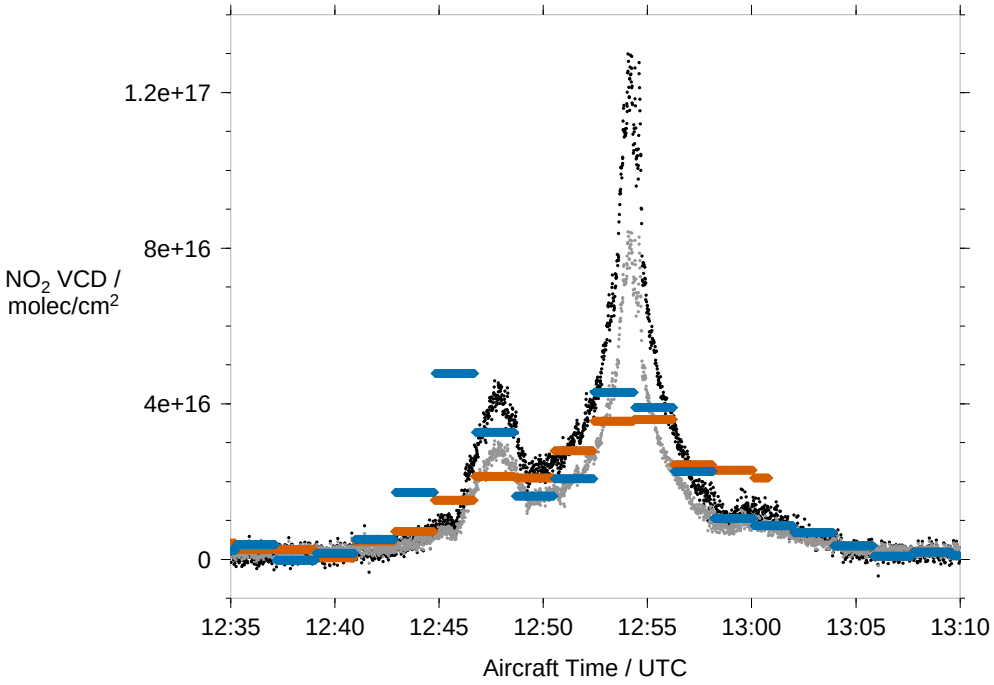


Figure 3.15: A time-series of $NO_2$ from the airborne DOAS (black: AMF=1.6, grey: amf=2.5), DOMINO $NO_2$ directly underneath the aircraft position (orange), and DOMINO $NO_2$ one satellite pixel upwind of the aircraft position (blue), on 9 August 2007.

at aircraft nadir and upwind was around $1.7\times10^{16}$ molecules.cm$^{-2}$. Around 12:48 UTC, while crossing the main plume from the Vaal triangle, the iDOAS measured a peak $NO_2$ VCD of approximately $2.8\times10^{16}$ molecules.cm$^{-2}$. The peak in the satellite measured $NO_2$ VCD at aircraft nadir is lower, around $2.0\times10^{16}$ molecules.cm$^{-2}$. Examining the satellite measurement upwind of the aircraft track, the $NO_2$ plume from the Vaal triangle is found to be further south, with the peak at around $4.9\times10^{16}$ molecules.cm$^{-2}$.

Overhead the city where $NO_2$ from traffic sources will play a larger part than downwind of the Vaal Triangle, there are small-scale features (around 12:54 UTC) that the airborne DOAS has detected that are not measured by the satellite. The highest $NO_2$ VCD measured by the aircraft was just over $8\times10^{16}$molecules.cm$^{-2}$ in this position, while the satellite measurement is less than half at approximately $3.8\times10^{16}$molecules.cm$^{-2}$. The larger AMF appropriate to RTM Scenario 10 gives a better qualitative agreement between the aircraft and the satellite. The gradual decrease in $NO_2$ VCD as the aircraft proceeded northwards past Pretoria is well captured by the satellite, particularly in the upwind pixel which matches the aircraft measurement very closely.

On 11 August 2007, takeoff was from Bethlehem at 10:06 UTC. The aircraft routed to Richards Bay, where a vertical profile from approximately 1500 feet (457m) above sea level was performed up to 20000 feet (6096m) AMSL. The aircraft tracked the satellite across Swaziland, cruising at 20000 feet. The satellite overtook the aircraft along this leg, at 11:54 UTC. The aircraft performed a vertical profile down to the surface, before landing at Nelspruit at 13:20 UTC to re-fuel. Takeoff from Nelspruit was at 14:17 UTC, and the aircraft ferried at low altitude back to Bethlehem, landing at 15:29 UTC. The complete flight track is shown in Figure 3.16.

Figure 3.17 shows a direct comparison between the airborne DOAS $NO_2$ VCD (calculated with AMF=2.5) and the OMI DOMINO $NO_2$ TVCD product. Except from Richards Bay itself, the aircraft is measuring an aged plume, more than 150 kilometres from any likely sources. Small spatial-scale features in the plume will have dispersed, and one can expect that the aircraft and satellite measurments will correlate closely. Between 12:20 and 12:40 the aircraft crossed a large plume that can be seen from the satellite measurement to be coming from the cluster of coal-fired power stations on the Eastern Highveld.

A comparison of the airborne DOAS $NO_2$ VCD time series with the co-located satellite measurement is shown in Figure 3.18. Vertical column densities are calculated with air-mass factors of 1.8 (plotted in black) and

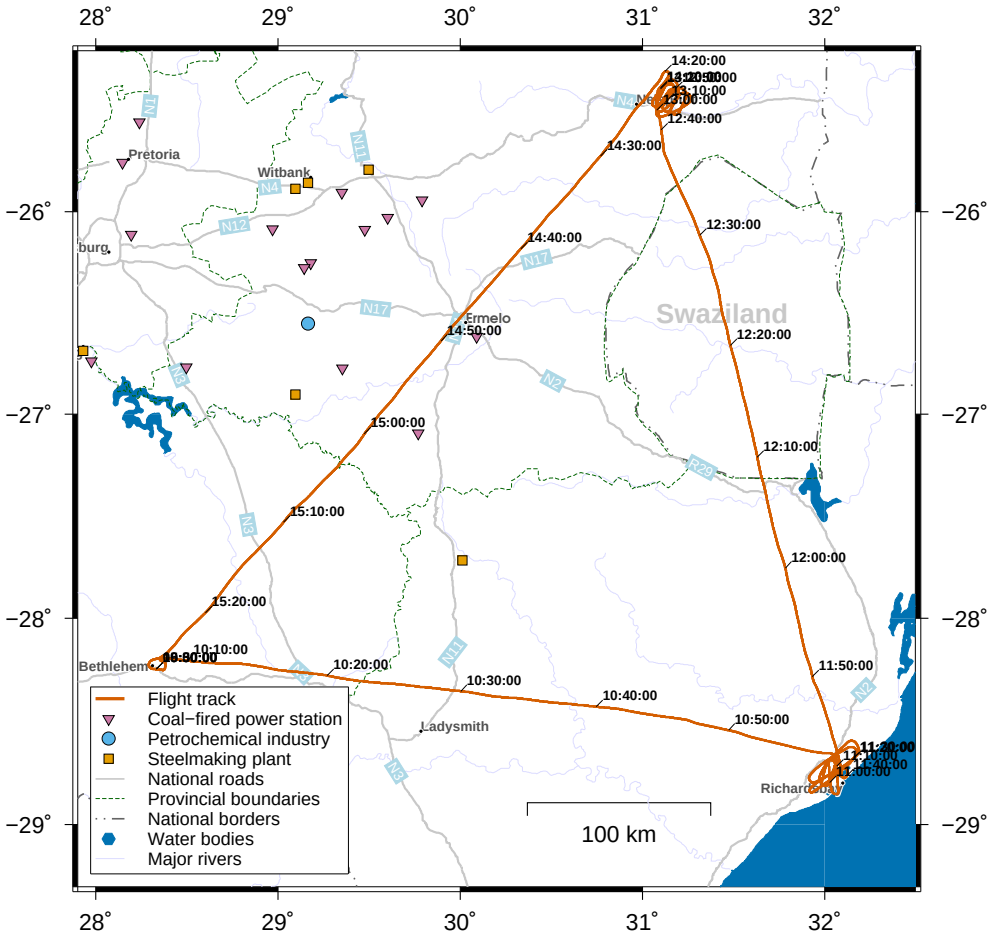


Figure 3.16: Flight track of the flight on 11 August 2007.

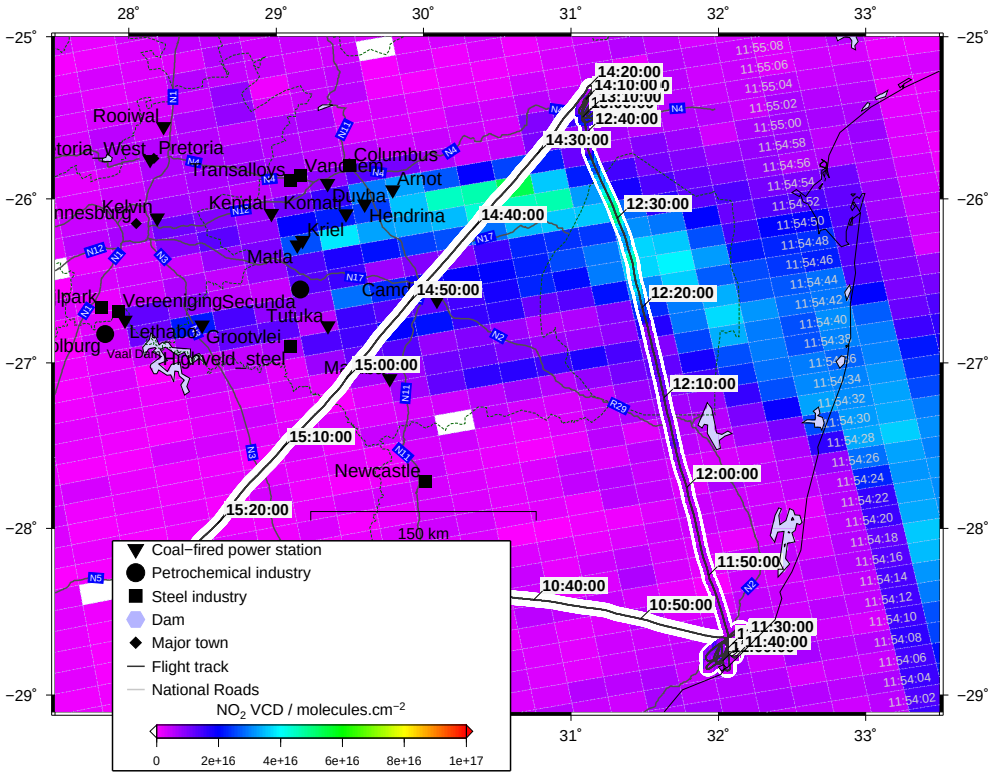


Figure 3.17: A comparison of the airborne DOAS $NO_2$ vertical column densities with DOMINO $NO_2$ from OMI on 11 August 2007. UTC aircraft time is indicated every ten minutes along the flight track, UTC satellite time is shown for each data row.

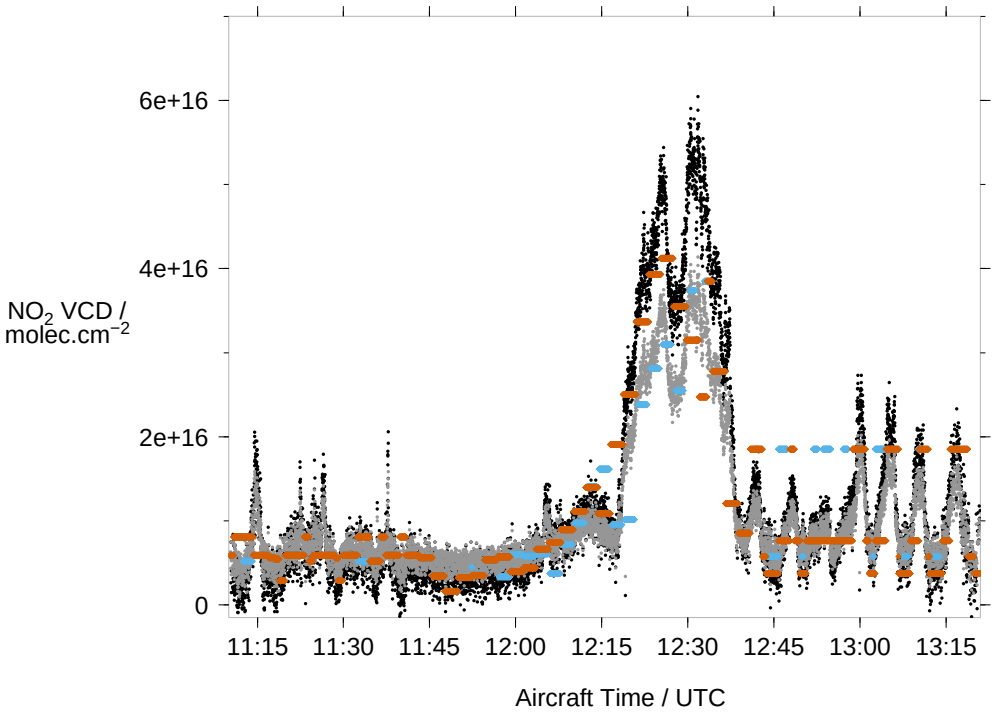


Figure 3.18: A time series comparison of the airborne DOAS $NO_2$ vertical column densities (black: AMF=1.8, grey: AMF=2.5), with DOMINO $NO_2$ from OMI, at the aircraft nadir position (orange) and one satellite pixel upwind of the aircraft (blue) on 11 August 2007.

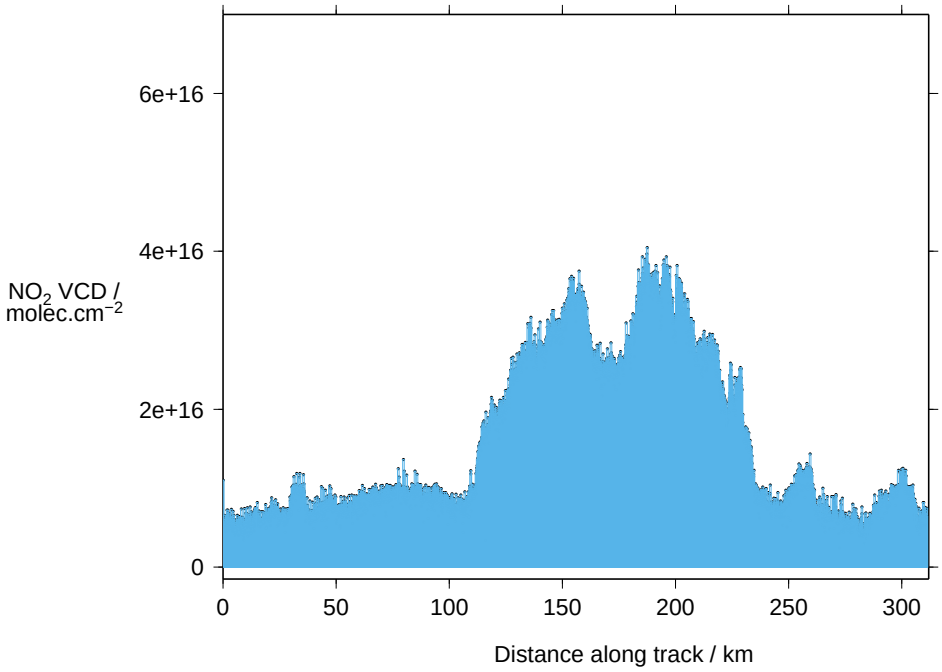


(a)

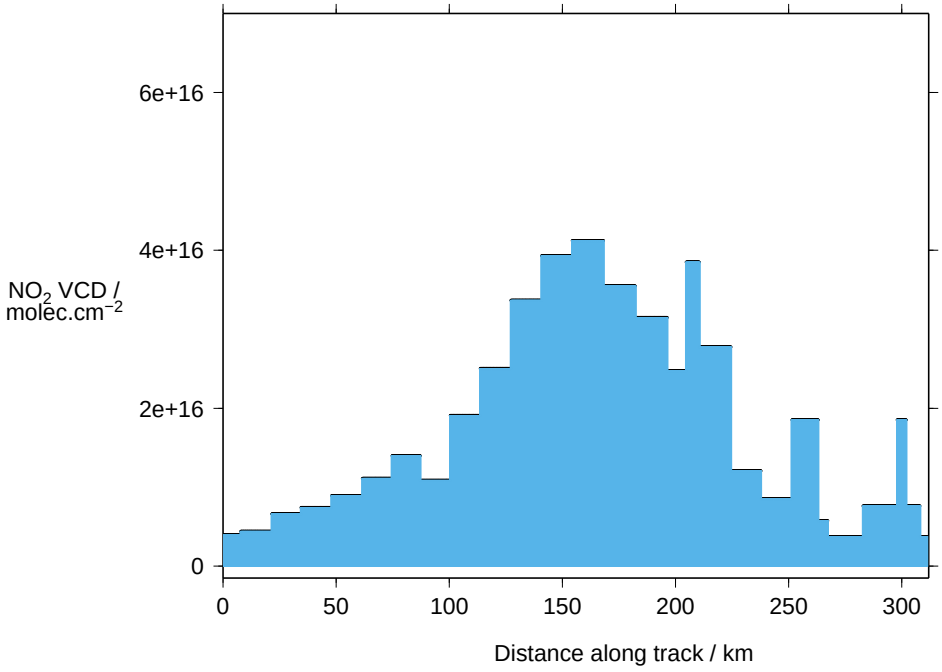


(b)

Figure 3.19: Areas under the curve used for flux estimates from the (a) aircraft and (b) satellite measurements.

2.5 (plotted in grey). Satellite measurements at aircraft nadir (shown in orange) and one pixel upwind (shown in cyan) of the aircraft are shown. These satellite measurements at aircraft nadir and upwind are broadly speaking quite close to each other, with the peak $NO_2$ VCD from OMI around $4\times10^{16}$molecules.cm$^{-2}$. Good agreement can be seen between the aircraft and the satellite starting at 11:40, when the aircraft started routing away from local sources in Richard's Bay. At 12:15 the aircraft measured the southern plume from the Vaal Triangle, Tutuka and Majuba power stations, the peak in the satellite measurement is $1.4\times10^{16}$ molecules.cm$^{-2}$; the aircraft measurement in this position is slightly lower at approximately $1.2\times10^{16}$ molecules.cm$^{-2}$.

In the satellite image, a large northern plume is evident that can be traced back to the city of Johannesburg, Secunda, and the cluster of power stations on the Eastern Highveld. This plume was measured by the aircraft between 12:20 and approximately 12:35. $NO_2$ VCD up to $4\times10^{16}$ molecules.cm$^{-2}$ was measured by OMI. The aircraft measurement with air-mass factor 2.5, although resolving smaller spatial scale features, also has a peak value of $4\times10^{16}$ molecules.cm$^{-2}$. At around 12:45 UTC, the aircraft was making measurements of the forest-fire plume, with peak $NO_2$ VCD's around $1.2\times10^{16}$ molecules.cm$^{-2}$ initially, increasing to around $2\times10^{16}$ molecules.cm$^{-2}$ as the aircraft performed a spiral descent. Since the evolution of the plume from the forest fire is not known, it is difficult to tell if this increase is real or resulting from a change in radiative transfer situation as the aircraft descends. The satellite measurement of this forest fire plume gave a $NO_2$ VCD of approximately $1.8\times10^{16}$ molecules.cm$^{-2}$.

Taking a similar approach to flux estimation as Heue *et al.* (2006), and using an estimate of the surface winds from the weather station at Kendal power station of 3m/s and 281°, a flux estimate for the Highveld on this day can be made. Figure 3.19a shows the area under the aircraft measurement curve that is used, the $NO_2$ flux derived from the aircraft using an air-mass factor of 2.5 is 395 tons per hour. Simliarly, $NO_2$ flux from the satellite product was calculated at 405 tons per hour. Naturally, the potential errors in such an estimate are large, and originate from both the measurement of the VCD and errors in the wind vector.

The flight on 14 August 2007 was planned to coincide with a SCIAMACHY overpass; however on this day three satellites passed over the same area, allowing some comparison to be made between the satellite products.

Takeoff from Bethlehem was at 06:25 UTC. The flight proceeded at low level to a point on the predicted SCIAMACHY track approximately 100km

north-east of Ermelo where a vertical profile was done from 1500 feet above ground to 19000 feet AMSL. The aircraft then proceeded south-bound along the predicted satellite track, performed another vertical profile measurement overhead Estcourt before proceeding at low-level back to Bethlehem, landing at 09:41 UTC.

Comparisons of $NO_2$ vertical column density are shown with SCIAMACHY (Figures 3.21 and 3.22), OMI (Figures 3.23 and 3.24), and GOME-2 (Figures 3.25 and 3.26). In Figures 3.21, 3.23 and 3.23, the aircraft VCDs was calculated using an AMF of 2.5.

Aircraft measurements on this day covered the northern part of SCIAMACHY's nadir segment. Much of the SCIAMACHY measurement is to the south of the power stations on the Eastern Highveld and as such, low $NO_2$ column densities were measured over much of the coverage area. SCIAMACHY shows a general enhancement of $NO_2$ column densities in the area of the power stations. The aircraft measurements show finer-scale plume features not captured by the satellite measurement. Around 08:01 the aircraft measured a plume with $NO_2$ VCD up to $2.5\times10^{16}$ molecules.cm$^{-2}$. SCIAMACHY measured approximately $1\times10^{16}$ molecules.cm$^{-2}$ at this position. A little later, around 08:08 and 08:09, the aircraft measured two plumes with $NO_2$ VCD of greater than $1.5\times10^{16}$ molecules.cm$^{-2}$, SCIAMACHY at this position measured around $0.4\times10^{16}$ molecules.cm$^{-2}$.

Examining Figures 3.23 and 3.24, it is clear that the higher spatial resolution of OMI allows it to better capture the finer spatial features. The northern plume resolved by OMI was not completely measured by the airborne DOAS on this day since the flight was planned to track SCIAMACHY. The southern plume from the Vaal Triangle, Tutuka and Majuba power stations, measured by the aircraft around 08:08 is resolved by the satellite. This gives an indication of the stable structure of this plume: the satellite overpass was 3 hours 40 minutes after the aircraft measurement. Inspection of the first vertical profile in Figure 3.5a on page 51 suggests RTM scenario 10 is appropriate, and hence an air-mass factor for the aircraft measurement of 2.5 is assumed.

The initial (northernmost) plume at 07:52 UTC aircraft time has a peak of $2.7\times10^{16}$ molecules.cm$^{-2}$. In this position, OMI measured a substantially lower VCD of around $1.4\times10^{16}$ molecules.cm$^{-2}$. The next plume measured by the aircraft at 07:57 has a peak $NO_2$ VCD of around $1.7\times10^{16}$ molecules.cm$^{-2}$. The peak in the OMI measurement is a little further north, and around $2\times10^{16}$ molecules.cm$^{-2}$. A narrow peak further south, at 08:01 aircraft time, is well resolved by the satellite, with the satellite peak of $2.2\times10^{16}$ molecules.cm$^{-2}$ closely matching the aircraft measured peak of

$2.5\times10^{16}$ molecules.cm$^{-2}$. The background measured by OMI further to the south of this ($1.4\times10^{16}$ molecules.cm$^{-2}$) is substantially higher than the aircraft measurement of around $0.4\times10^{16}$ molecules.cm$^{-2}$. This may be related to the different measurement time. The southernmost large plume measured by the aircraft (actually two separate plumes with peaks of approximately $1.5\times10^{16}$ molecules.cm$^{-2}$ are resolved by the airborne DOAS), is further south in the satellite measurement, also with a peak of just over $1.5\times10^{16}$ molecules.cm$^{-2}$.

Metop-A, carrying the GOME-2 instrument passed overhead the aircraft track at approximately 07:24 UTC, twenty-five minutes earlier than SCIAMACHY. Spatial resolution of GOME-2 is similar to SCIAMACHY and inspection of Figure 3.25 reveals a similar pattern of $NO_2$ SCD. The large pixel size of GOME-2 is also unable to resolve the fine spatial scale of the plumes. The initial peak at 07:57, measured by the aircraft to be approximately $1.7\times10^{16}$ molecules.cm$^{-2}$, is reduced to $1.2\times10^{16}$ molecules.cm$^{-2}$ in the GOME-2 measurement. The next plume measured by the aircraft at 08:01 with a peak $NO_2$ VCD of $2.5\times10^{16}$ molecules.cm$^{-2}$ is measured by GOME-2 at $1\times10^{16}$ molecules.cm$^{-2}$. The twin plumes measured by the airborne DOAS at 08:08 with peak $NO_2$ VCD of around $1.5\times10^{16}$ molecules.cm$^{-2}$ are not resolved by the satellite, which measured an $NO_2$ VCD of $0.75\times10^{16}$ molecules.cm$^{-2}$.

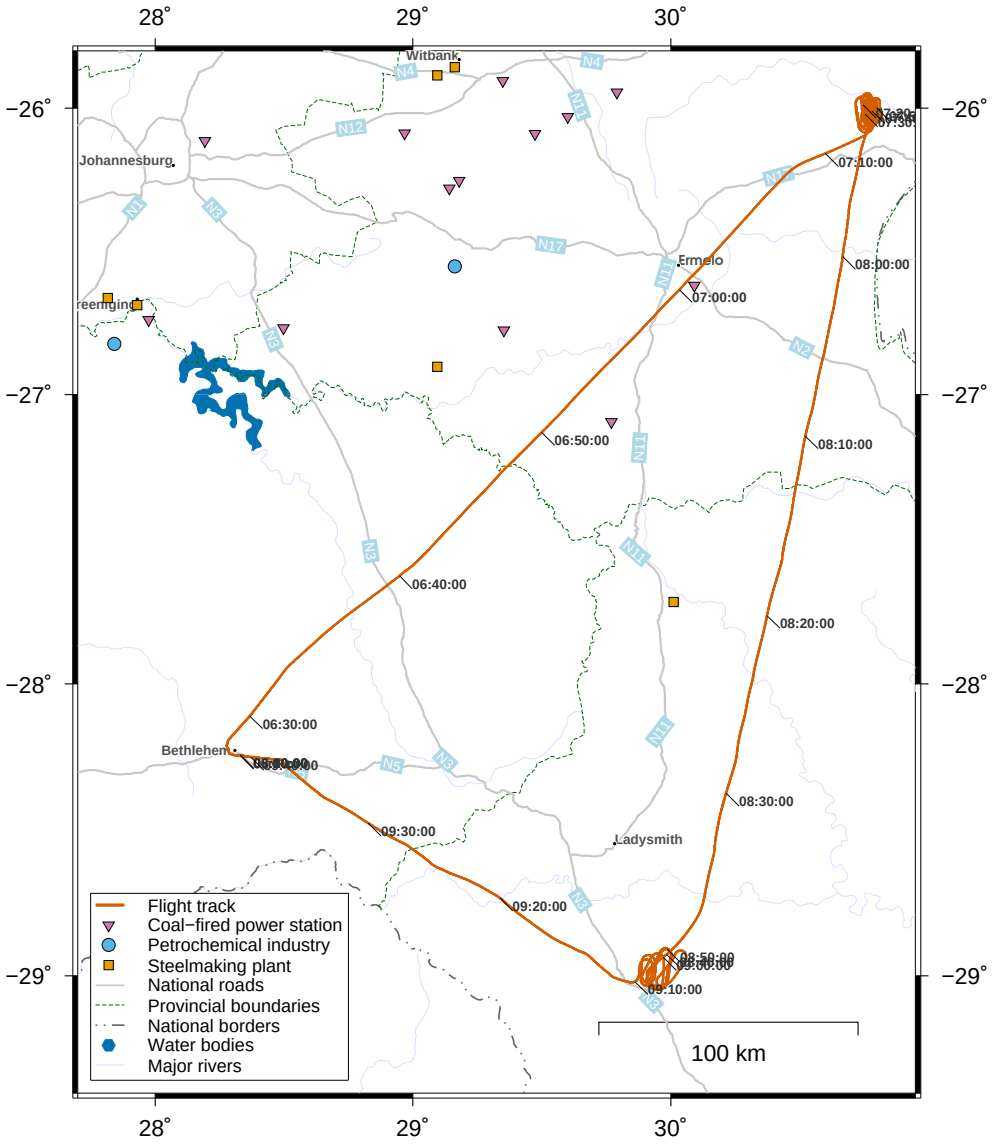


Figure 3.20: Complete track of the flight on 14 August 2007.

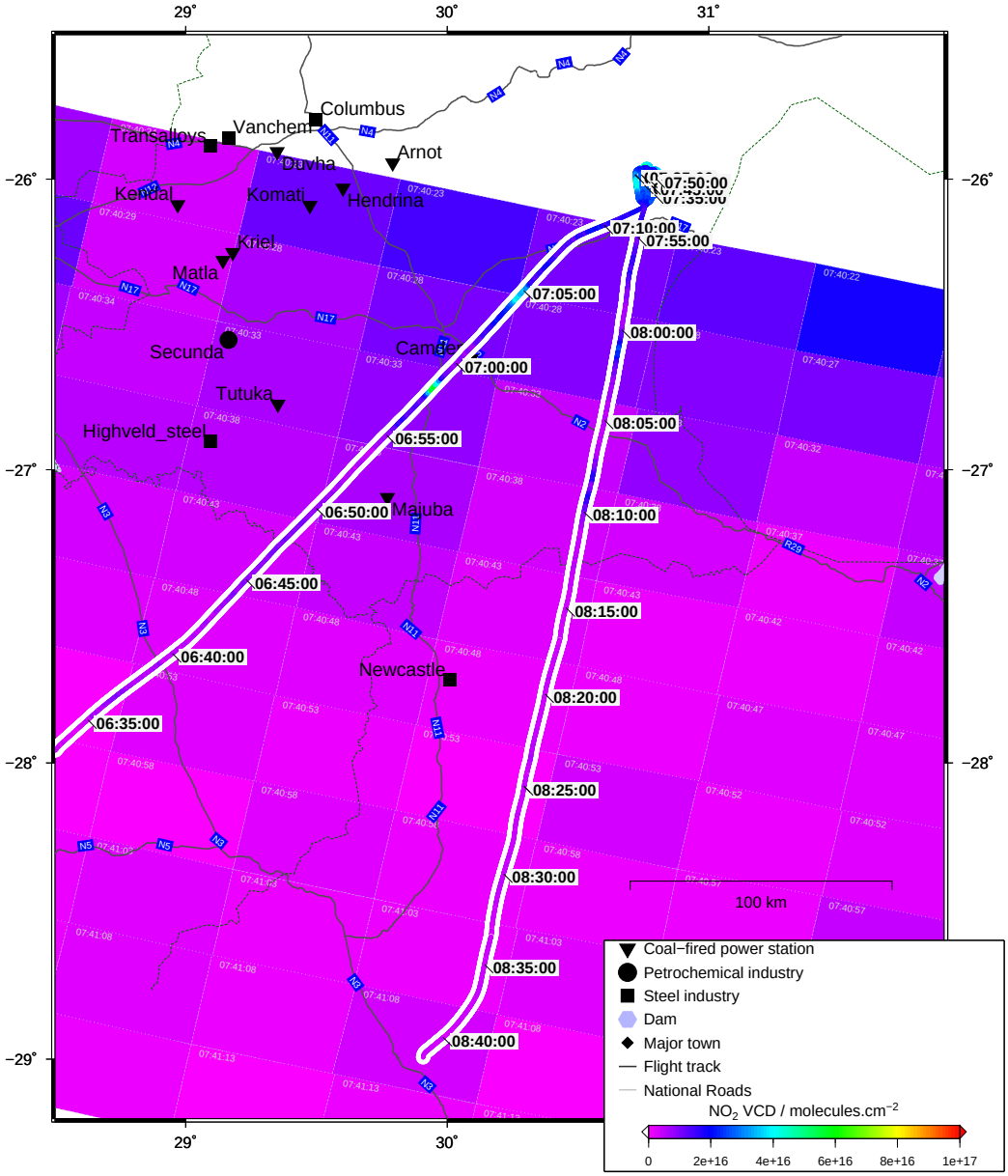


Figure 3.21: A comparison of the airborne DOAS measurements with the SCIAMACHY satellite instrument on 14 August 2007.

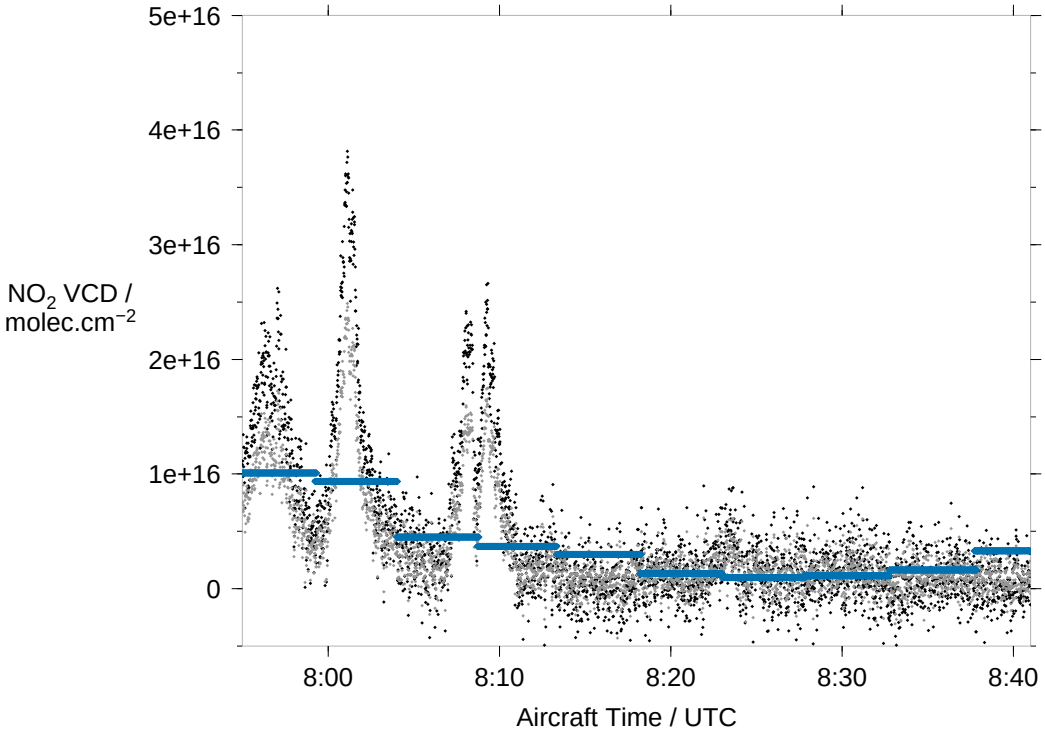


Figure 3.22: A time-series comparison of $NO_2$ measured by the airborne DOAS (black: AMF=1.8, grey: AMF=2.5) and the SCIAMACHY satellite measurement on 14 August 2007.

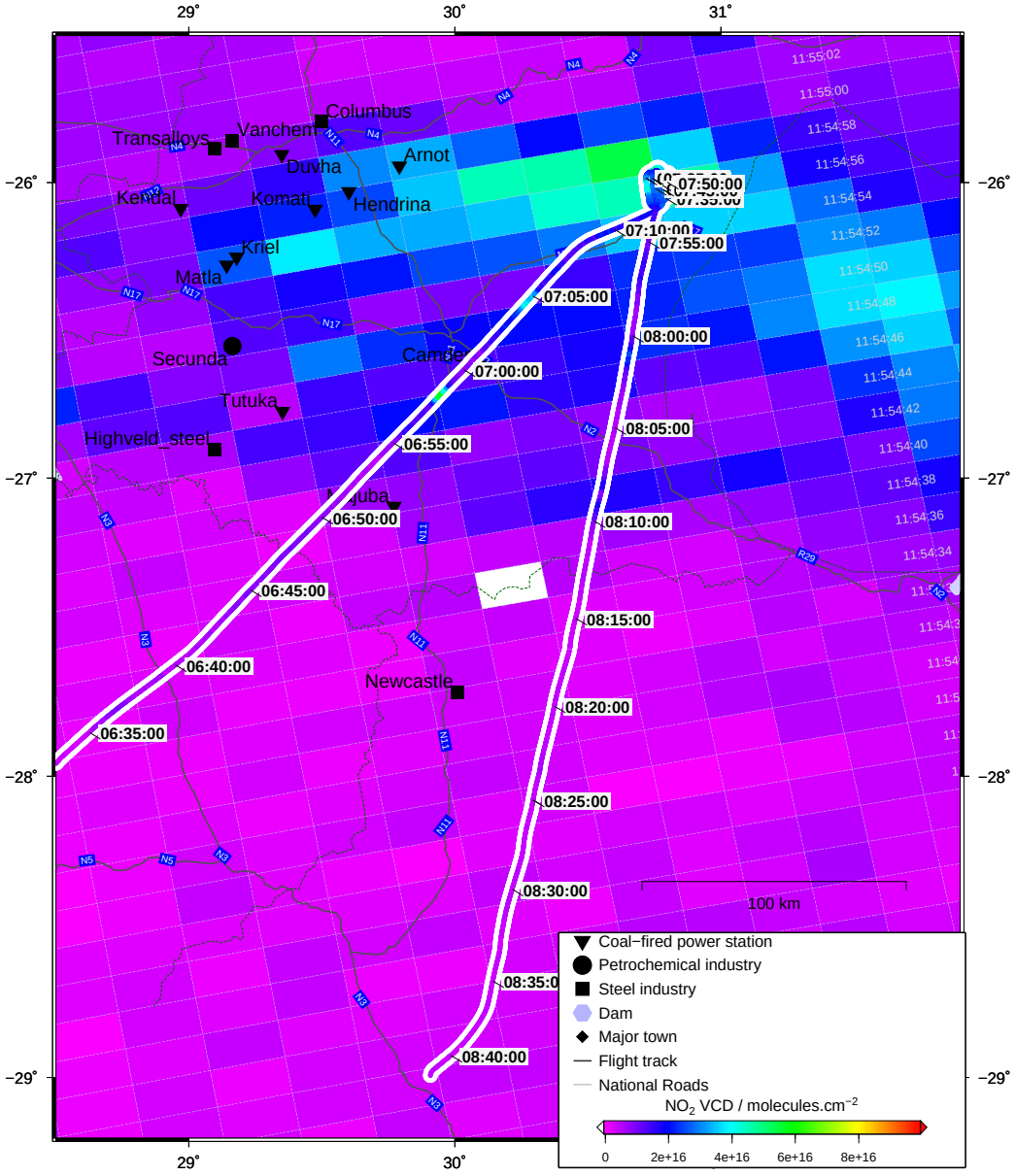


Figure 3.23: A comparison of the airborne DOAS measurements with the OMI DOMINO satellite product on 14 August 2007.

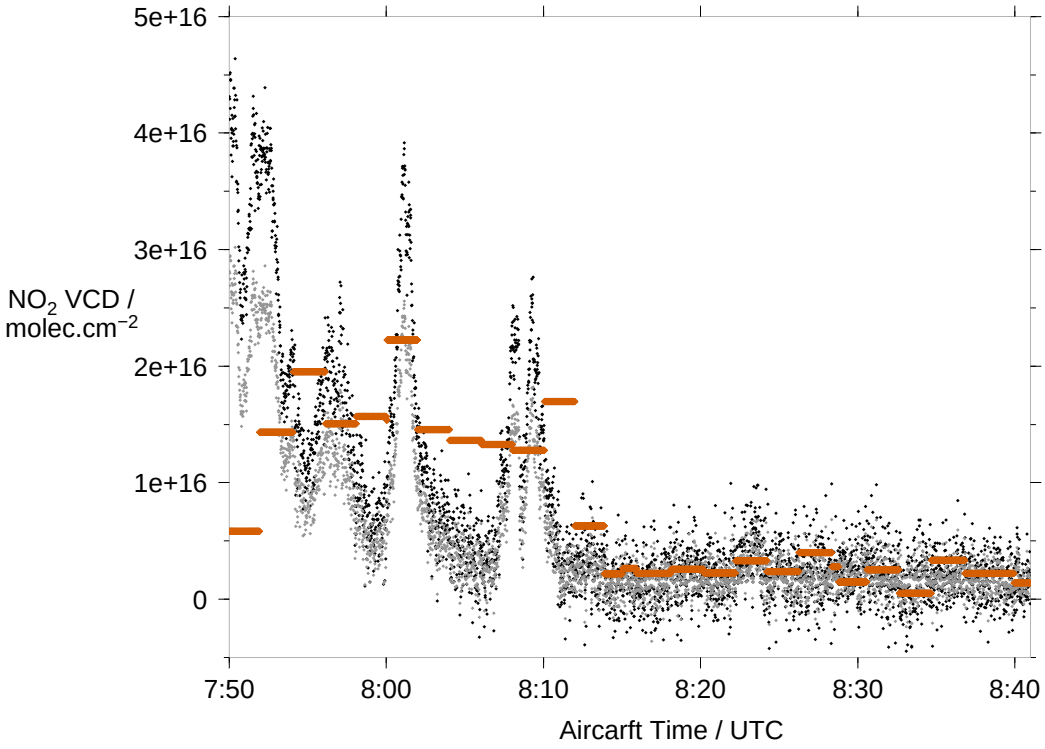


Figure 3.24: A time-series comparison of $NO_2$measured by the airborne DOAS (black: AMF=1.8, grey: AMF=2.5) and the OMI DOMINO product on 14 August 2007.

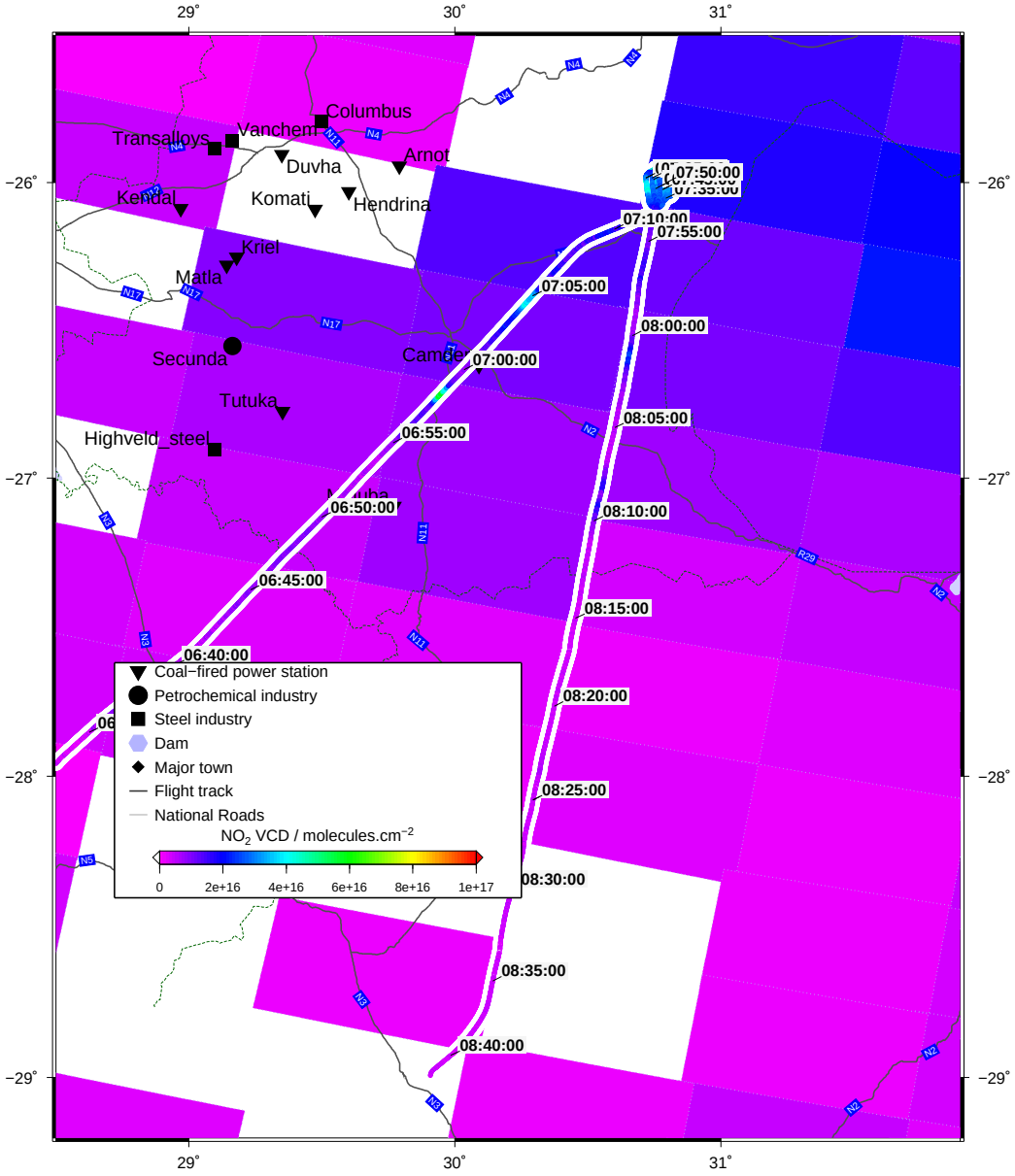


Figure 3.25: A comparison of the airborne DOAS measurements with the GOME-2 satellite instrument on 14 August 2007.

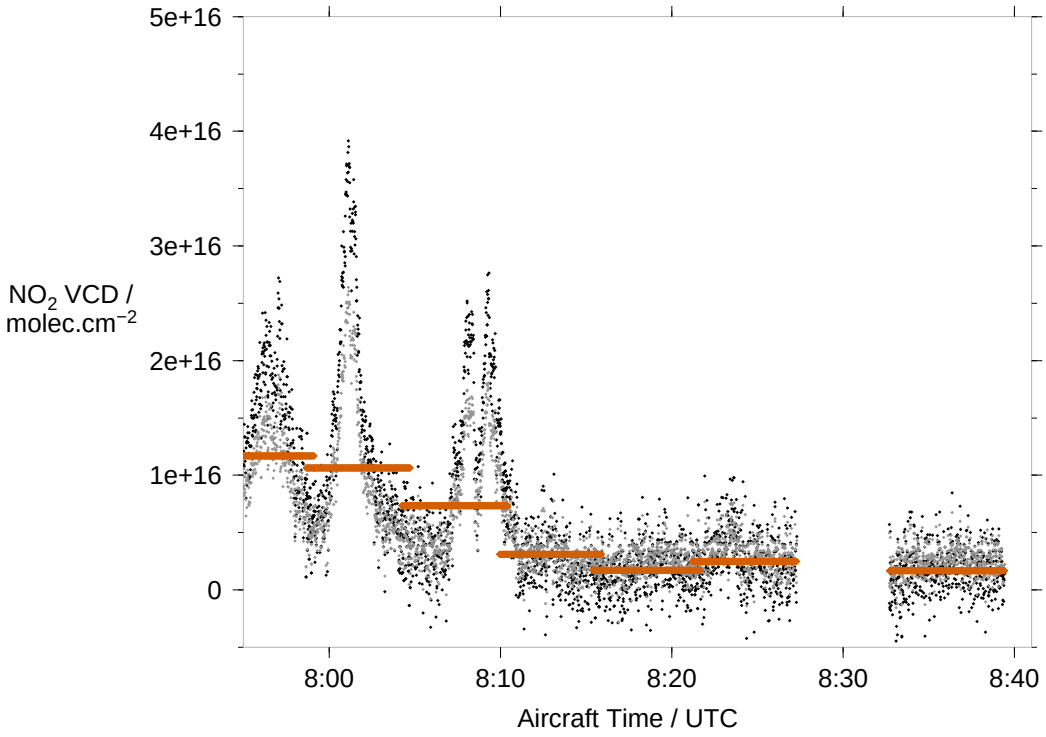


Figure 3.26: A time-series comparison of $NO_2$ measured by the airborne DOAS and the GOME-2 satellite instrument on 14 August 2007.

Figure 3.27 shows the complete flight track for the flight on 18 August 2007. The primary GPS connected to the data logger failed on this flight, GPS data from a handheld receiver was used to reconstruct the flight path, however the logging interval of the handheld GPS was ten seconds, hence the dotted line depicting the flight track in the figure. Takeoff from Bethlehem was at 11:14 UTC, landing back at 14:24 UTC. This flight passed over the Eastern Highveld, close to Camden power station and between Hendrina and Arnot power stations.

Figure 3.28 shows a direct comparison between the $NO_2$ vertical column density measured by the airborne DOAS instrument (with AMF of 2.5) during the high-altitude segment of the flight and the DOMINO $NO_2$ product from OMI. There is general agreement between the satellite and the aircraft measurement. The plume from Majuba power station is resolved by both, as are plumes to the east of Camden power station and west of Hendrina.

Figure 3.29 shows a time-series comparison of OMI DOMINO at aircraft nadir and one satellite ground pixel upwind of the aircraft with the airborne DOAS nadir $NO_2$ vertical column density. Between 12:35 and 12:45 aircraft time, using an air-mass factor of 2.5, the airborne DOAS resolves an initial plume of approximately $2\times10^{16}$ molecules.cm$^{-2}$, which is missed by OMI, which shows a smooth increase in VCD between the background and the main peak measured at 12:45 aircraft time. This latter peak is measured by the aircraft at $4.5\times10^{16}$ molecules.cm$^{-2}$; OMI measured approximately $2.4\times10^{16}$ molecules.cm$^{-2}$ at aircraft nadir and $4\times10^{16}$ molecules.cm$^{-2}$ in the upwind pixel. Around 12:50 there is a decrease in $NO_2$ measured by both the satellite and the aircraft, there is good agreement between the two for the aircraft-nadir satellite pixel. The plume from Secunda, Matla and Kriel is crossed by the aircraft at 12:54, with a peak $NO_2$ VCD of $4.6\times10^{16}$ molecules.cm$^{-2}$. There is a corresponding enhancement in the column densities measured by the satellite, with the upwind pixels giving a better match to the aircraft, bearing in mind that the aircraft track is substantially different from the satellite's. The aircraft peak $NO_2$ at 12:54 is $5.5\times10^{16}$ molecules.cm$^{-2}$; OMI gives an $NO_2$ VCD around $4\times10^{16}$ molecules.cm$^{-2}$ at aircaft nadir. At 13:02 a broad plume appearing to come from Duvha and Hendrina power stations is measured by the aircraft with peak $NO_2$ VCD of $6.8\times10^{16}$ molecules.cm$^{-2}$. The satellite, which measured the same area an hour before measured a much broader plume of $NO_2$ VCD around $4.5\times10^{16}$ molecules.cm$^{-2}$. Between 13:04 and 13:05 a narrow plume was measured by the aircraft with $NO_2$ VCD $4.8\times10^{16}$ molecules.cm$^{-2}$, it is difficult to determine its origin from inspection of the figure. It would appear to be too narrow to be originating from Duvha power station, given the broadening witnessed in the other plumes.

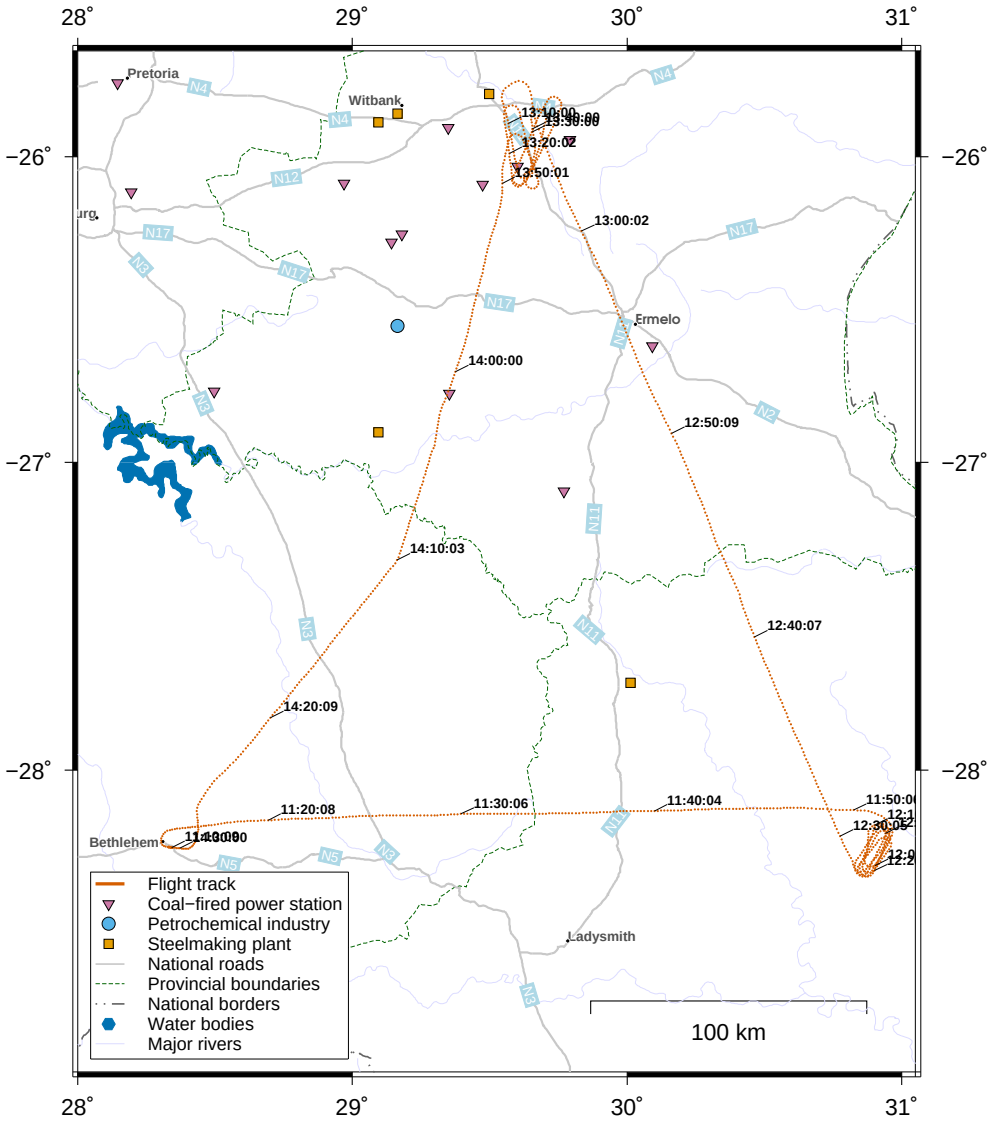


Figure 3.27: Complete track of the flight on 18 August 2007.

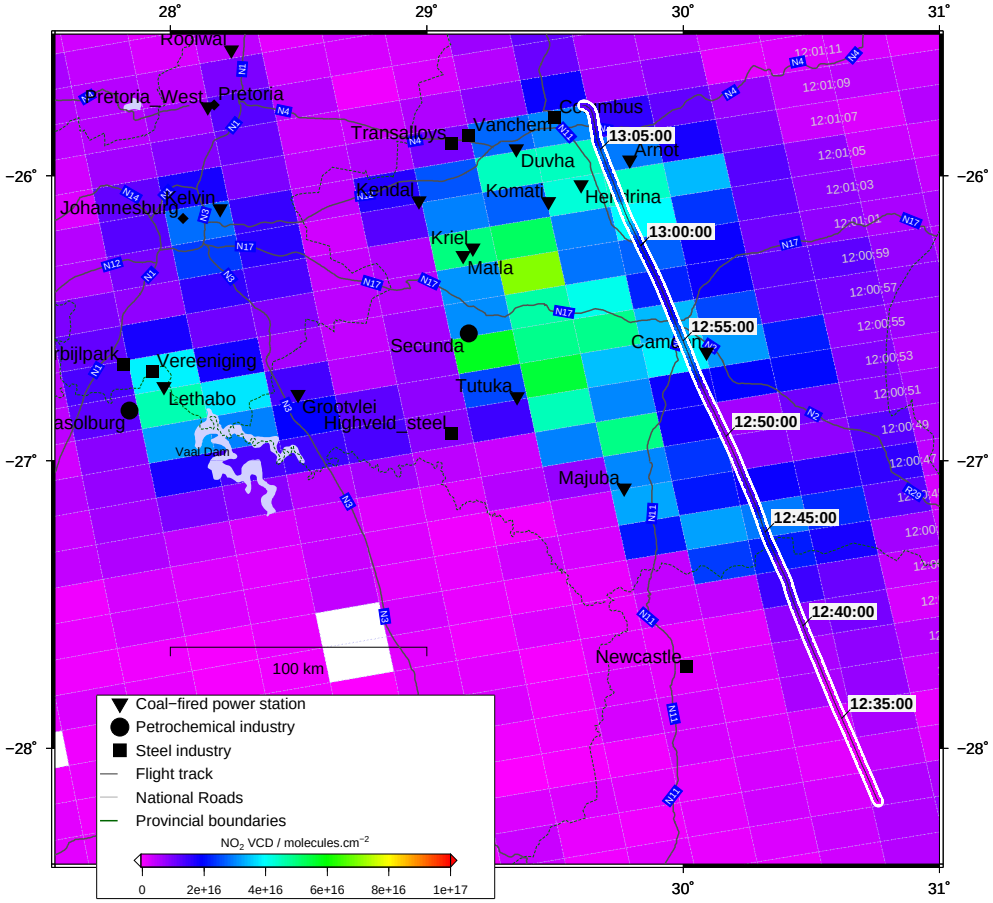


Figure 3.28: A direct comparison between the airborne DOAS $NO_2$ vertical column density and measurements from OMI on 18 August 2007.

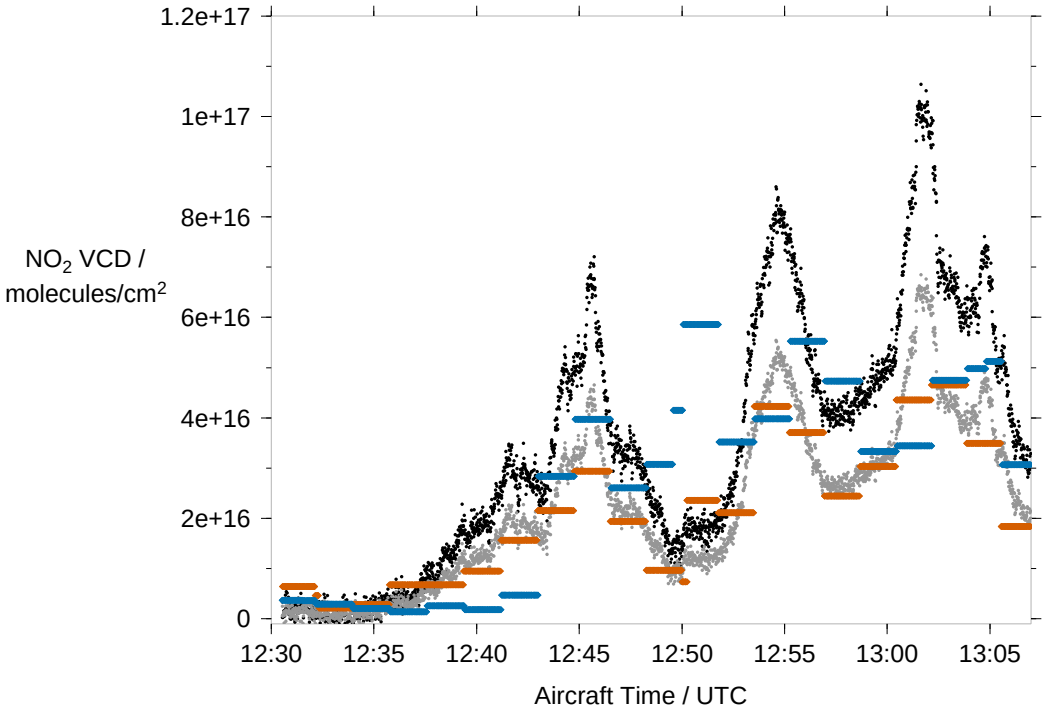


Figure 3.29: A time-series comparison of the airborne DOAS measurement (black: AMF=1.8, grey: AMF=2.5) OMI DOMINO at aircraft nadir (orange) and OMI DOMINO one satellite pixel upwind of the aircraft (blue) on 18 August 2007.

In general, good qualitative agreement is found between the aircraft measurements and the satellites. The satellites with larger ground-pixels generally fare worse, since they cannot resolve the small spatial features of the plumes observed, and generally underestimate the peak $NO_2$ VCD measured by the aircraft. In cases where a plume has advected further downwind and had sufficient time to disperse, and for measurements of background values, the satellite measurements more closely match the airborne DOAS. It would appear that in general, an AMF of 2.5 for the airborne DOAS gives a better match to the satellite measurements, implying the presence of a ubiquitous elevated layer, as well as an approximately exponential profile of $NO_2$ and aerosols.

It should be noted that the airborne DOAS and the satellite instruments suffer from the same sources of error, and it would therefore seem that in-situ measurements of vertical profiles using a suitable instrument would be a better technique. However, the problem of spatial resolution mismatch is even greater, unless a flight strategy can be developed to cover a significant area of a satellite pixel during a vertical profile measurement. An airborne imaging DOAS with a wider swath and reduced spatial resolution, such as the HAIDI (General *et al.* 2014), would be a good complimentary measurement to in-situ measurements for satellite validation.

# Chapter 4

# Satellite Climatology

Nine years of Level 3 OMI NASA standard product from 1 January 2005 to 31 December 2013 were analysed. An overview of the mean, minimum, maximum, and data availability for the nine years, as well as a seasonal analysis is presented in Figure 4.1. The seasons used for this analysis were December to February (DJF), March to May (MAM), June to August (JJA), and September to November (SON). Larger scale maps of the same data are presented in subsequent figures.

Figure 4.2 shows the mean $NO_2$ tropospheric vertical column density (TVCD) over Southern Africa during this time period. Enhancements over the background levels are evident at various scales: over the continent compared to over the oceans, as well as over metropolitan and industrialised areas within South Africa. Matimba power station near the town of Lephalale, an isolated point source, also contributes to an enhancement of the mean values in the surrounding area particularly to the south-west. The Highveld region, including the Johannesburg-Pretoria conurbation and the Vaal triangle to the south of Johannesburg, as well as the area to the east of these towns, has mean $NO_2$ TVCD's up to an order of magnitude larger than any other area on the sub-continent. The area of enhanced mean $NO_2$ TVCD extends over Swaziland, and beyond the east coast of South Africa. Northern Angola has an enhancement in $NO_2$ TVCD similar in intensity to the smaller urban areas in South Africa, which is generally attributed to winter biomass burning (van der A *et al.* 2008).

Seasonal mean $NO_2$ TVCD over Southern Africa is presented in Figure 4.3. The DJF season has the lowest mean over the Highveld as well as over Cape Town, Port Elisabeth and East London. Mean $NO_2$ in the region of Matimba power station is consistent across the seasons. During MAM and JJA, the Eastern Highveld mean $NO_2$ is at its highest, and the spatial extent of $NO_2$

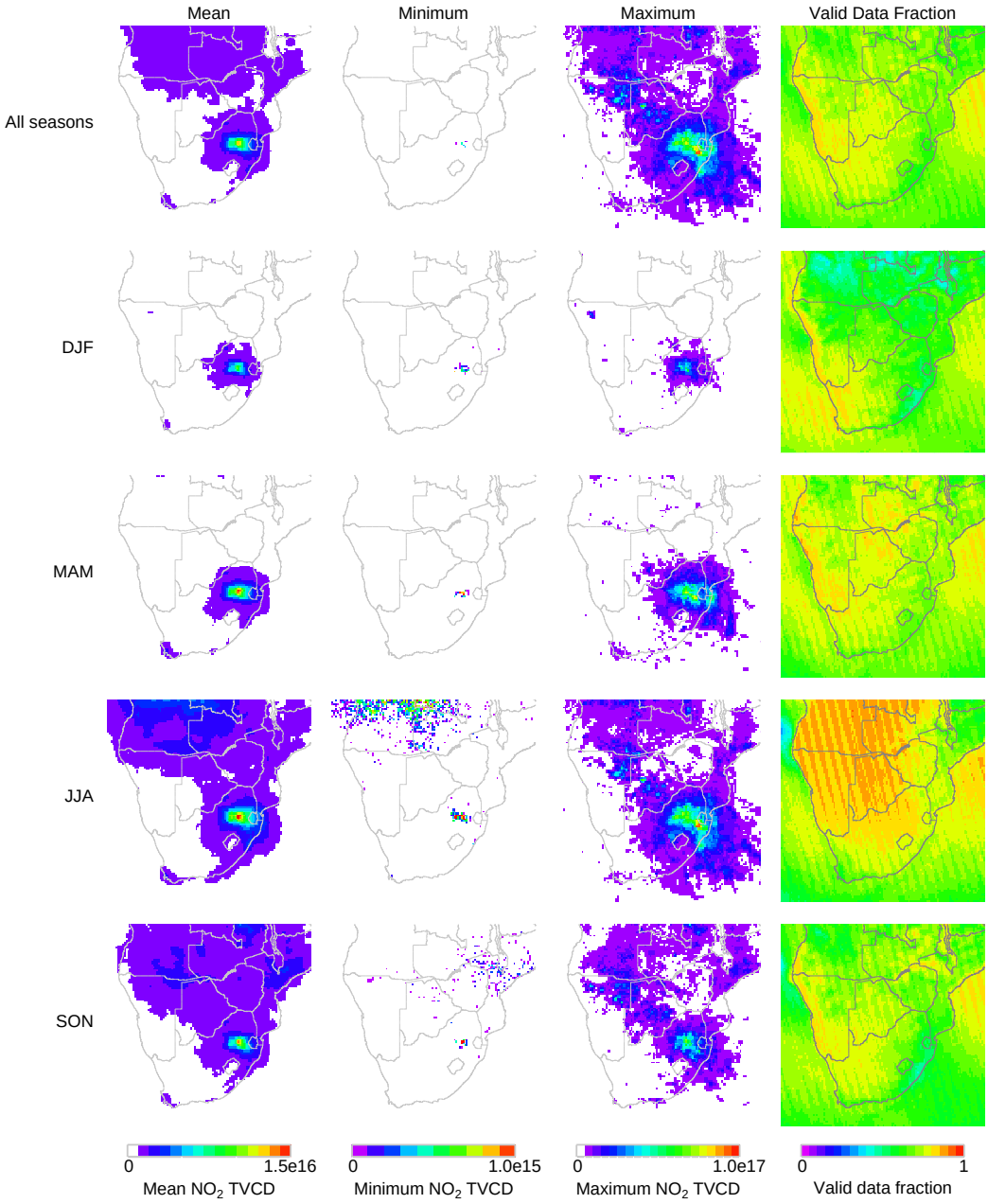


Figure 4.1: Satellite climatology overview from OMI Level 3 data between 1 January 2005 and 31 December 2013. Mean, minimum, maximum, as well as the fraction of days with valid data are shown for the whole nine-year period, as well as for each of the seasons. Note that the colour-scales are different for each quantity. These maps are reproduced at a larger scale in subsequent figures.

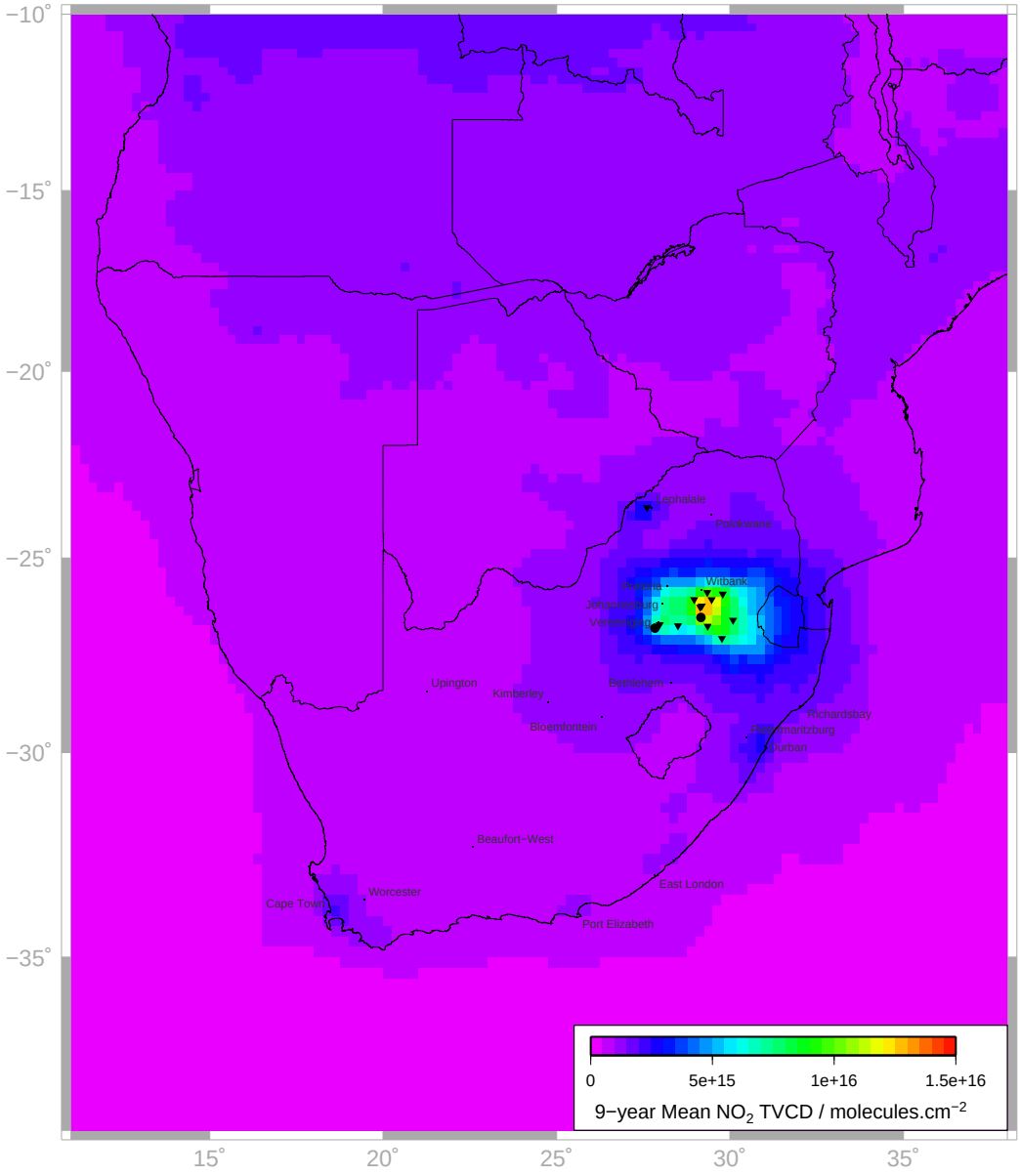


Figure 4.2: Mean tropospheric $NO_2$ vertical column density over Southern Africa calculated from nine years of OMI Level 3 data between 1 January 2005 and 31 December 2013.

TVCD's greater than a threshold of approximately $7\times10^{15}$ molecules.cm$^{-2}$ is largest. A region of slightly higher seasonal $NO_2$ TVCD's (between $1\times10^{15}$ and $3\times10^{15}$ molecules.cm$^{-2}$) expands in spatial extent from its smallest during DJF, to encompass the eastern half of South Africa as well as large parts of Botswana, Zimbabwe and Mozambique during June to November. This region of enhancement appears to be controlled by topography around the Drakensberg escarpment to the east of Lesotho; the Lesotho high ground has low $NO_2$ TVCD's compared to surrounding areas during all seasons. The area surrounding Cape Town shows an enhancement in $NO_2$ TVCD consistent in intensity and spatial extent across the seasons, except for a decrease in both of these parameters during DJF.

Seasonal minimum $NO_2$ TVCD is plotted in Figure 4.4. During the winter months, the minimum values are greater than in the summer, and the spatial extent of these high minima is larger. Some isolated areas have JJA minima during nine years of measurement between $1.4\times10^{15}$ and $1.5\times10^{15}$ molecules.cm$^{-2}$. This can be ascribed to lower dispersion potential in winter as well as higher emissions from domestic heating sources.

Seasonal maximum $NO_2$ TVCD's are shown in Figure 4.5. The presence of seasonal maxima (during JJA and SON) in areas of Botswana and Namibia indicate that these are transient sources, most likely biomass burning. The central Highveld shows no such seasonal pattern in the nine-year maximum, although there is a reduction in the maxima during DJF, when dispersion potential is higher compared to the other seasons.

Data availability (i.e. the fraction of days with valid data) by season is shown in Figure 4.6. The central Highveld summer months have around sixty percent data availability compared to close to eighty percent in the winter, most likely due to higher cloud cover during the summer rainy season. Over the Eastern Highveld, data availability in winter is slightly lower at around seventy-five percent. The western Cape shows a similar pattern, with lower data availability during the rainy winter months of JJA compared to DJF. The Atlantic coast of Namibia shows a stark contrast between over-land and over-water values. This is likely related to the formation of fog which occurs preferentially over the water. Off the Mozambique coast, there is the opposite pattern: data availability over the water is generally better than over the land. There appears to be an artefact in the data, with striping of the data availability maps at the satellite's orbital inclination. This is likely related to inherently decreased data quality at the edges of the OMI swath.

A polynomial fit was done within each Level 3 spatial pixel, as described in Section 2.3.2. The linear fit parameter, indicating the annual change in $NO_2$

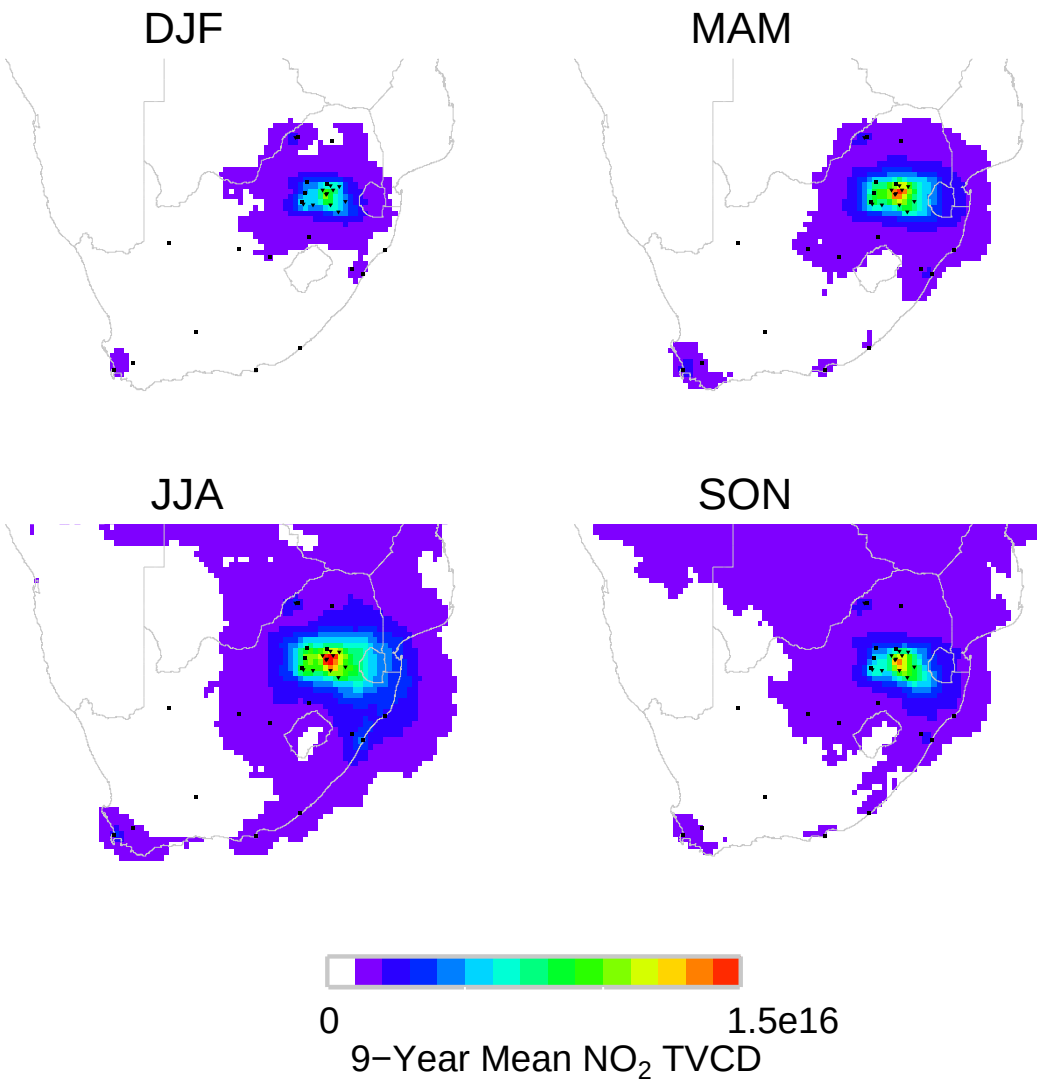


Figure 4.3: Mean tropospheric $NO_2$ VCD over South Africa for each season from nine years of OMI Level 3 data. Towns and coal-fired power stations are as indicated in Figure 4.2; however the names are omitted for clarity.

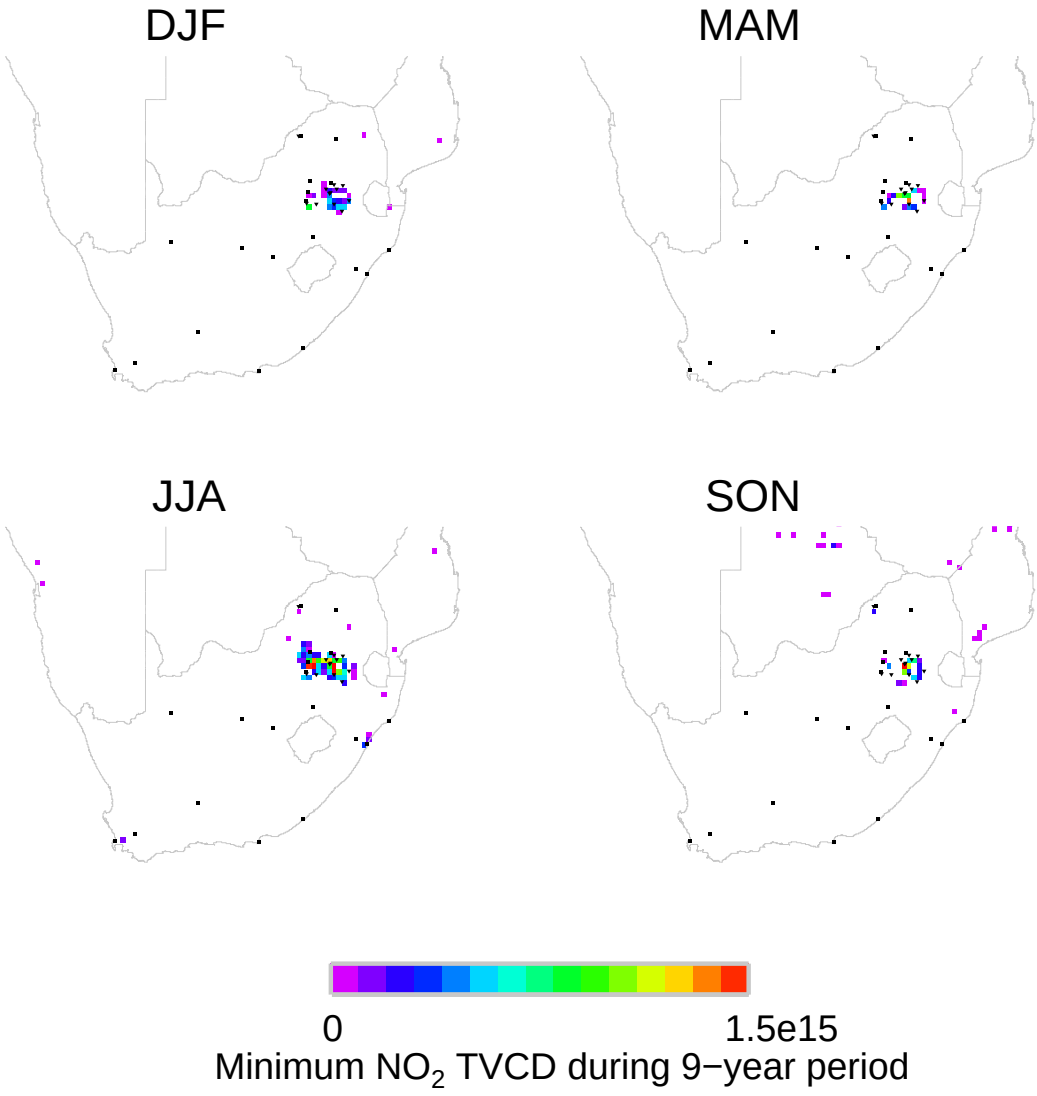


Figure 4.4: Minimum tropospheric $NO_2$ VCD over South Africa for each season from nine years of OMI Level 3 data. Towns and coal-fired power stations are as indicated in Figure 4.2; however the names are omitted for clarity.

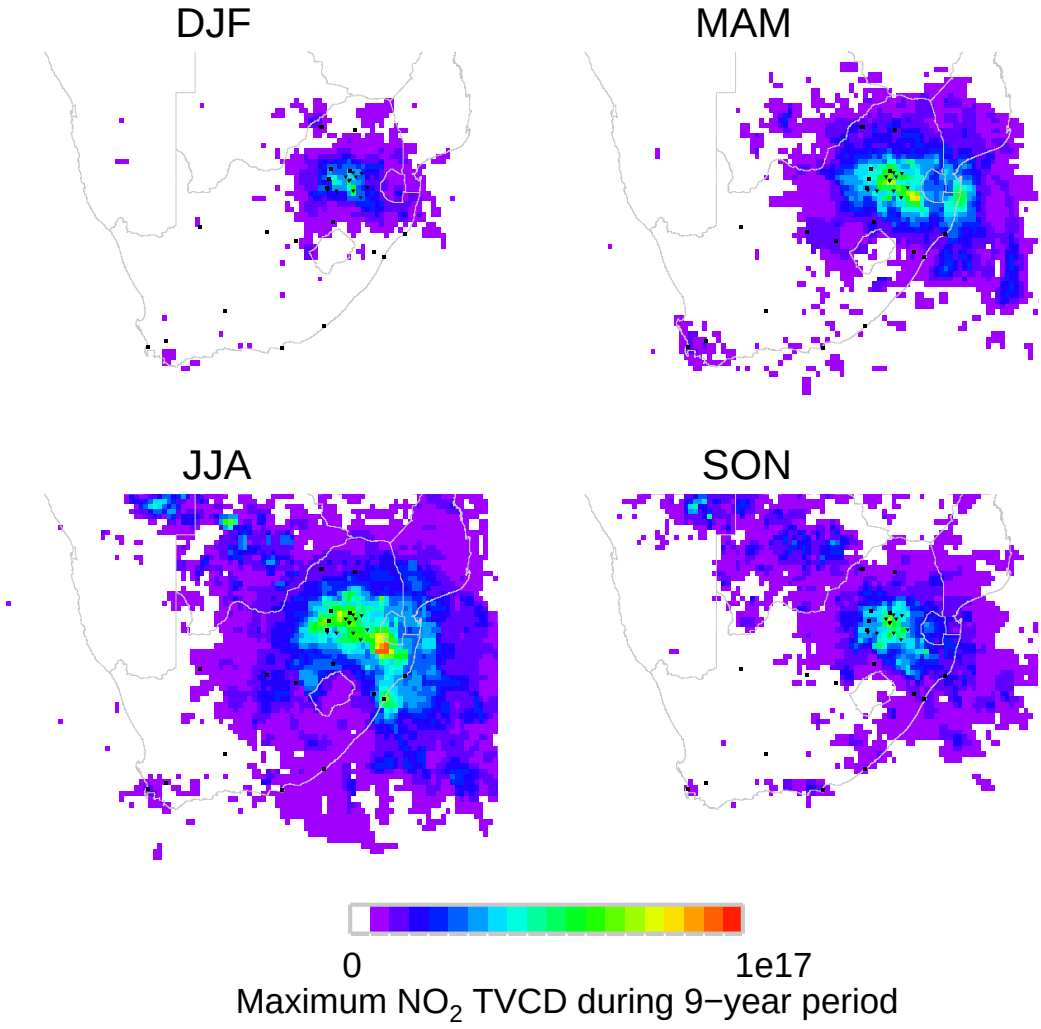


Figure 4.5: Maximum tropospheric $NO_2$ VCD over South Africa for each season from nine years of OMI Level 3 data. Towns and coal-fired power stations are as indicated in Figure 4.2; however the names are omitted for clarity.

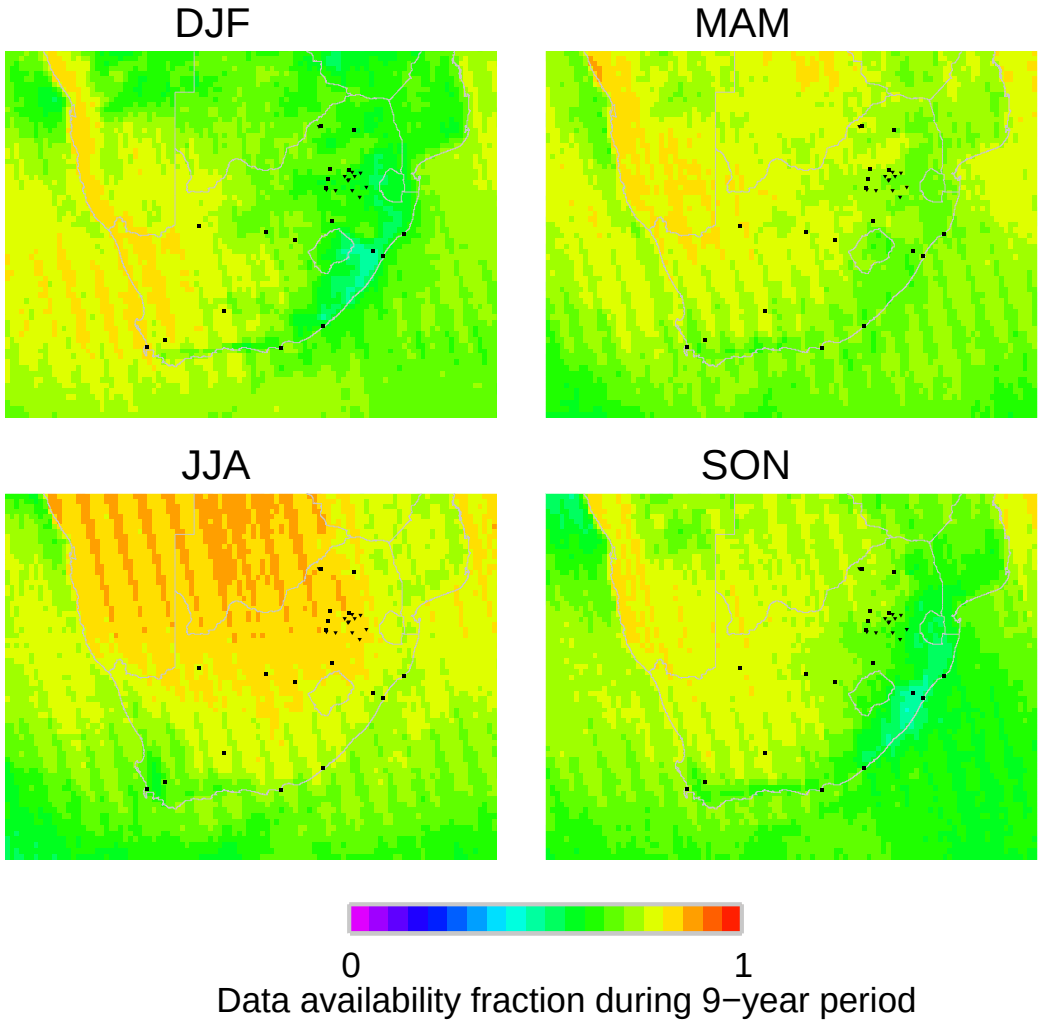


Figure 4.6: $NO_2$ TVCD fractional data availability over South Africa for each season from nine years of OMI Level 3 data. Towns and coal-fired power stations are indicated as in Figure 4.2; however the names are omitted for clarity.

TVCD is plotted in Figure 4.7. Most areas in South Africa show very little change over the nine years analysed. The areas around Johannesburg and Pretoria, as well as between Witbank and Secunda show a decrease in $NO_2$ TVCD. South of these areas is a broad area of increasing $NO_2$ TVCD, which extends over Swaziland and into the Indian Ocean. The largest increases are found to the east-south-east of the power station cluster, towards the border with Swaziland. This area of increase corresponds approximately with the locus of the plume exiting the Highveld in an easterly direction. The magnitude of the decreasing trends around Johannesburg and Witbank is up to three times larger than that of the increasing trends in the areas immediately adjacent. North-eastern Namibia displays an area of increasing trend; the possible origins of this trend are unknown. Southern Angola also has some areas of linear increase in $NO_2$ TVCD. These increasing trends in Namibia and Angola are in contrast to the literature which shows either no trend (Richter *et al.* 2005), or a negative trend (van der A *et al.* 2008).

The relative trend (i.e. the absolute trend divided by the mean) in $NO_2$ TVCD is shown in Figure 4.8. In this view, several features that may have been missed on inspection of the absolute trend stand out. The areas of increasing trend in north-eastern Namibia and southern Angola are again evident. In Zambia several areas of decrease are evident. There is a large area of decreasing trend stretching from west of Johannesburg and Pretoria, over the eastern Highveld and in a north-easterly direction over Mozambique. The increase seen over the Indian Ocean in the absolute trend is evident again in the relative trend. Decreasing trends over Durban and Cape Town, and to a lesser extent over Port Elizabeth can be seen. There is a hint of a pattern at orbital inclination, particularly evident over the ocean south-east of the Cape.

The fit parameter corresponding to the amplitude of the seasonal variation in $NO_2$ TVCD is plotted in Figure 4.9. Metropolitan areas such as Cape Town and Port Elisabeth have a larger amplitude than the surrounding areas. The area around Durban has a larger seasonal variation than Cape Town. The area immediately east of Johannesburg has a still larger seasonal variation. The Eastern Highveld south-east of Witbank displays the highest variation. The area of increased seasonal amplitude extends to the east of the Highveld, extending over Swaziland, and beyond the east coast at Kosi Bay. Northern Angola's seasonal variation is similar to that over Durban and the Vaal Triangle to the south of Johannesburg. Areas over the ocean to the south-west of Cape Town, as well as a large area over the Kalahari and Namib deserts have extremely low variation.

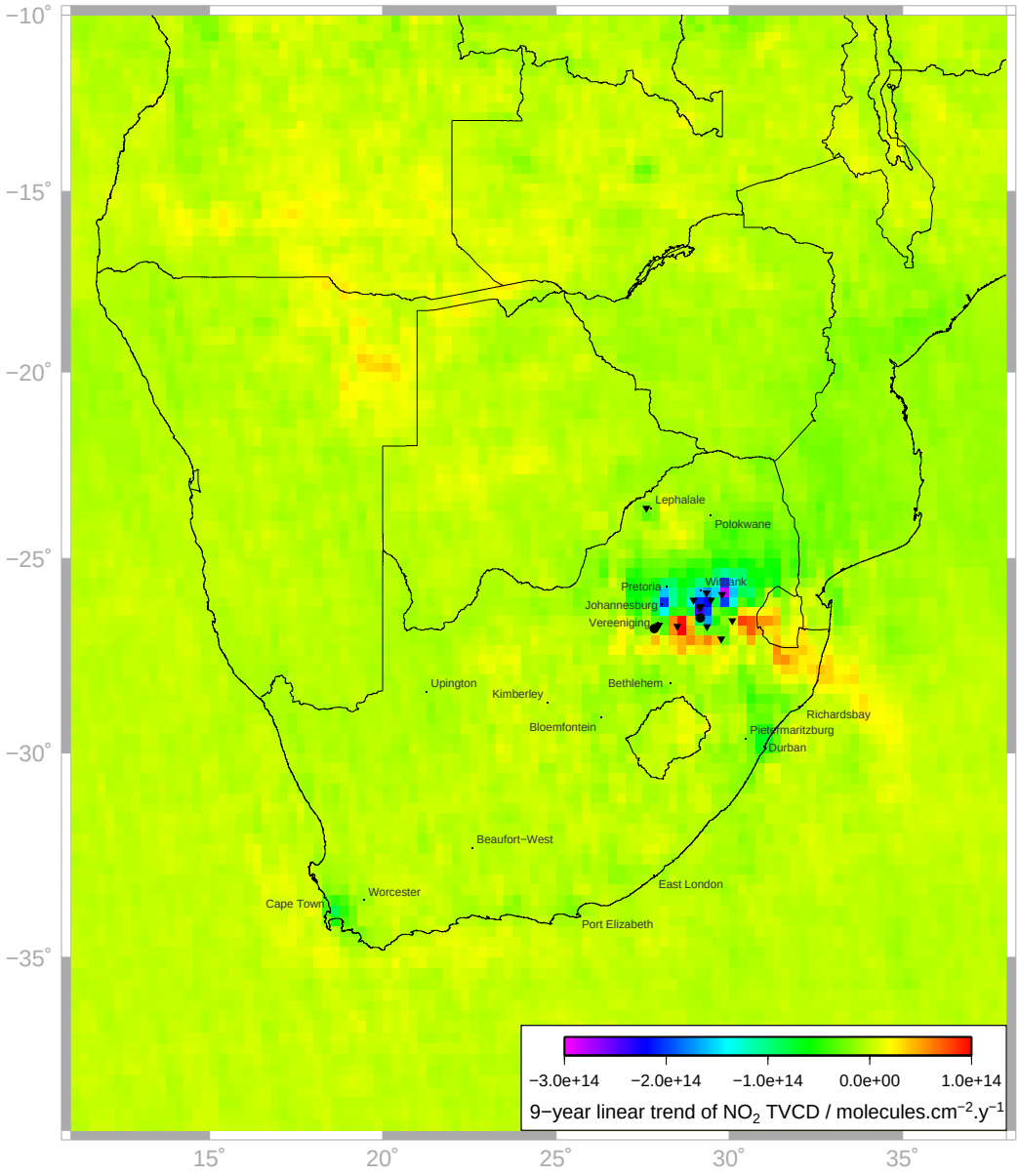


Figure 4.7: Linear trend of $NO_2$ TVCD from OMI Level 3 data between 1 January 2005 and 31 December 2013.

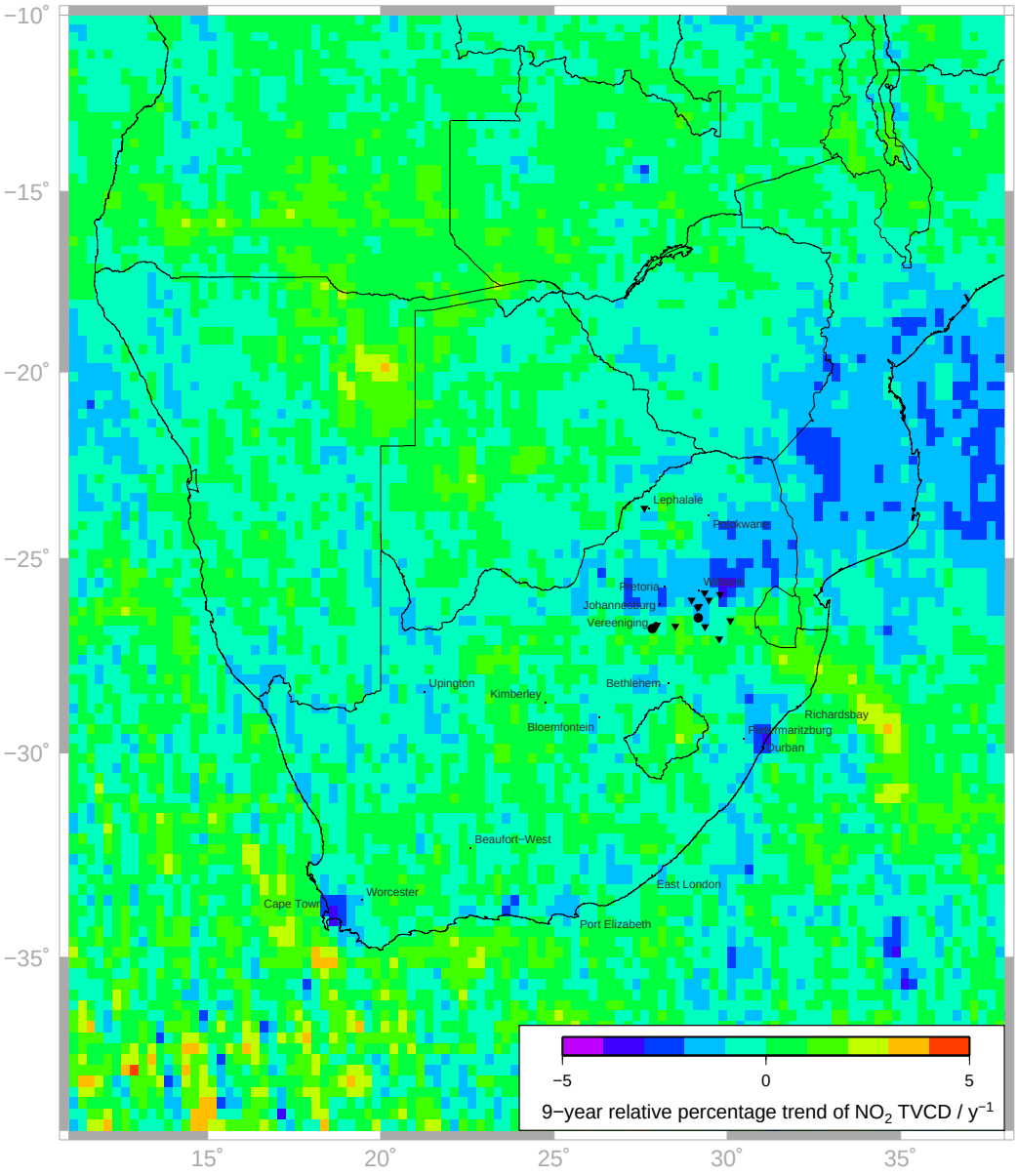


Figure 4.8: Relative trend of $NO_2$ TVCD from OMI Level 3 data between 1 January 2005 and 31 December 2013.

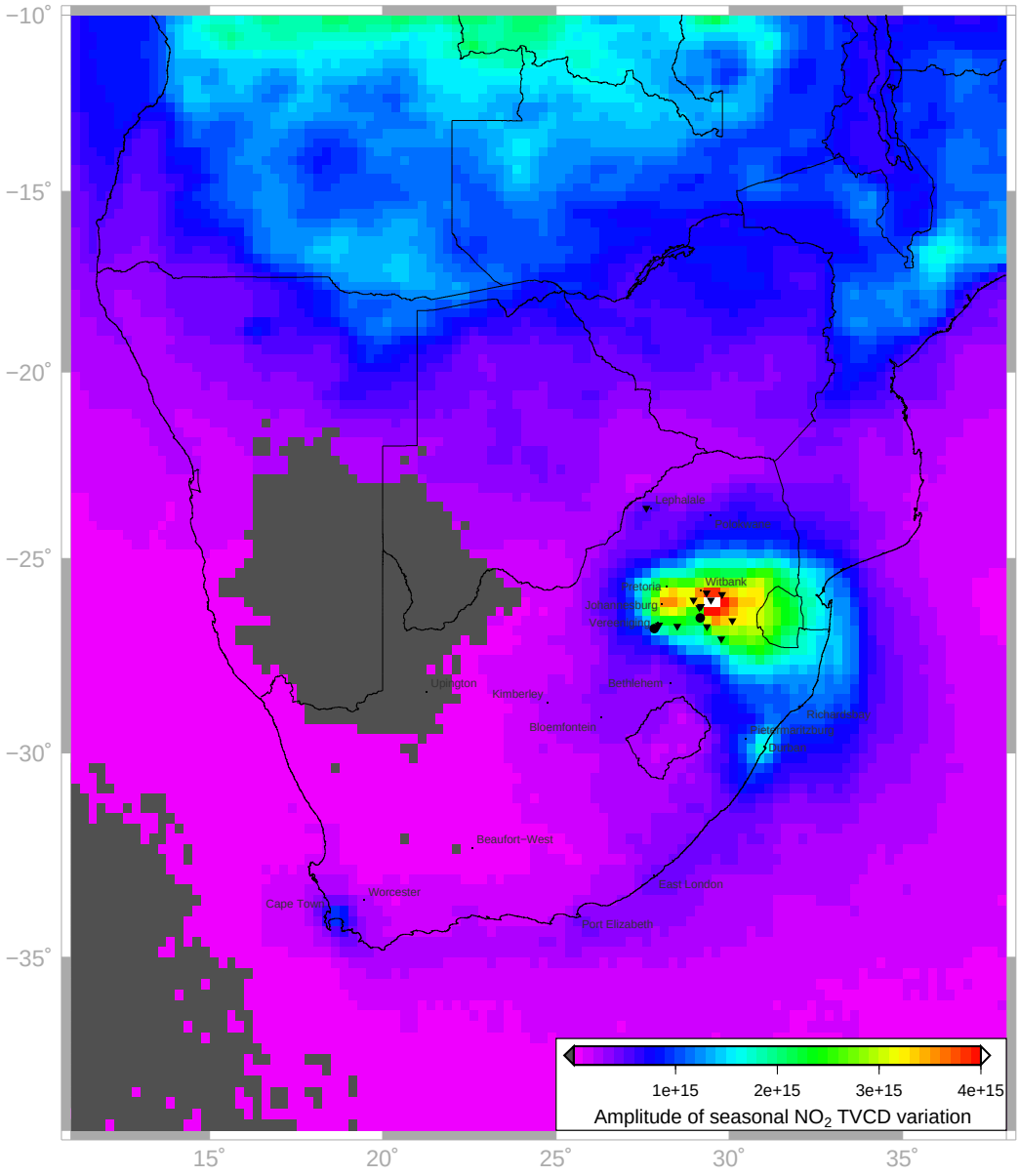


Figure 4.9: Amplitude of seasonal variation of $NO_2$ TVCD from OMI Level 3 data between 1 January 2005 and 31 December 2013.

The Julian day of the seasonal peak of $NO_2$ TVCD determined from the $\beta_3$ parameter is plotted in Figure 4.10. A table of Julian days is given in Appendix A on page 128. Areas of very low seasonal variation (Figure 4.9) and low mean $NO_2$ TVCD (Figure 4.2 on page 93) over the ocean display a noisy pattern of adjacent pixels of early and late peak $NO_2$: likely an artefact arising from the difficulty of fitting a sine curve to data that has very little seasonal variation. There is a gradient in the day of peak $NO_2$ TVCD extending from northern Angola (peak at the end of July), through Zambia (early August peak), Botswana, Namibia and Zimbabwe (late August to early September peak). Comparing this with the peak month of fire counts from the MODIS sensor (Giglio *et al.* 2006), reproduced in Figure 4.11, there appears to be a strong spatial correlation between peak fire counts and peak $NO_2$ from OMI. This north-west to south-east gradient of later peak $NO_2$ is reversed as one moves across the northern border of South Africa.

Kwazulu-Natal and the eastern Cape have their peak $NO_2$ around early July to early August. A large area over the Namib and Kalahari deserts, extending into the Northern Cape, has a peak during April to May (Julian day 90 to 140). This area corresponds with an area of no fire counts (Giglio *et al.* 2006), and is attributed to soil $NO_x$ emissions (van der A *et al.* 2008).

The Highveld appears as an area of earlier peak, compared to the regions to the north and south. The central Highveld (i.e. the region enclosed by Pretoria-Vaal Triangle-Secunda-Witbank) is an area of uniform late-June peak. Extending to the south-west of this is a tongue of relatively early peak reaching to the east of Maseru. To the east and north-east of the central Highveld, an early-peak tongue extends over Swaziland to the Indian Ocean. These tongues correspond respectively with re-circulation and eastwards transport of emissions from the Highveld. Matimba power station near to the town of Lephalale appears as an isolated area of relatively early-peak, compared to surrounding areas.

Focussing on the eastern half of South Africa, inspection of the nine-year mean $NO_2$ TVCD shown in Figure 4.12 allows three regions of interest (ROI) to be identified from the data: the greater Highveld area including Johannesburg, Pretoria, the Vaal Triangle, and the Eastern Highveld; the area around Matimba power station and the town of Lephalale; and the area around Durban and Pietermaritzburg. These ROI are labelled Region 1, 2, and 3 respectively. Over the western Cape, the nine-year mean $NO_2$ is plotted in Figure 4.13: we define as Region 4 as shown.

Spatial averaging within each of these regions was done for each day's data, and a polynomial fit was performed on the spatially-averaged daily measure-

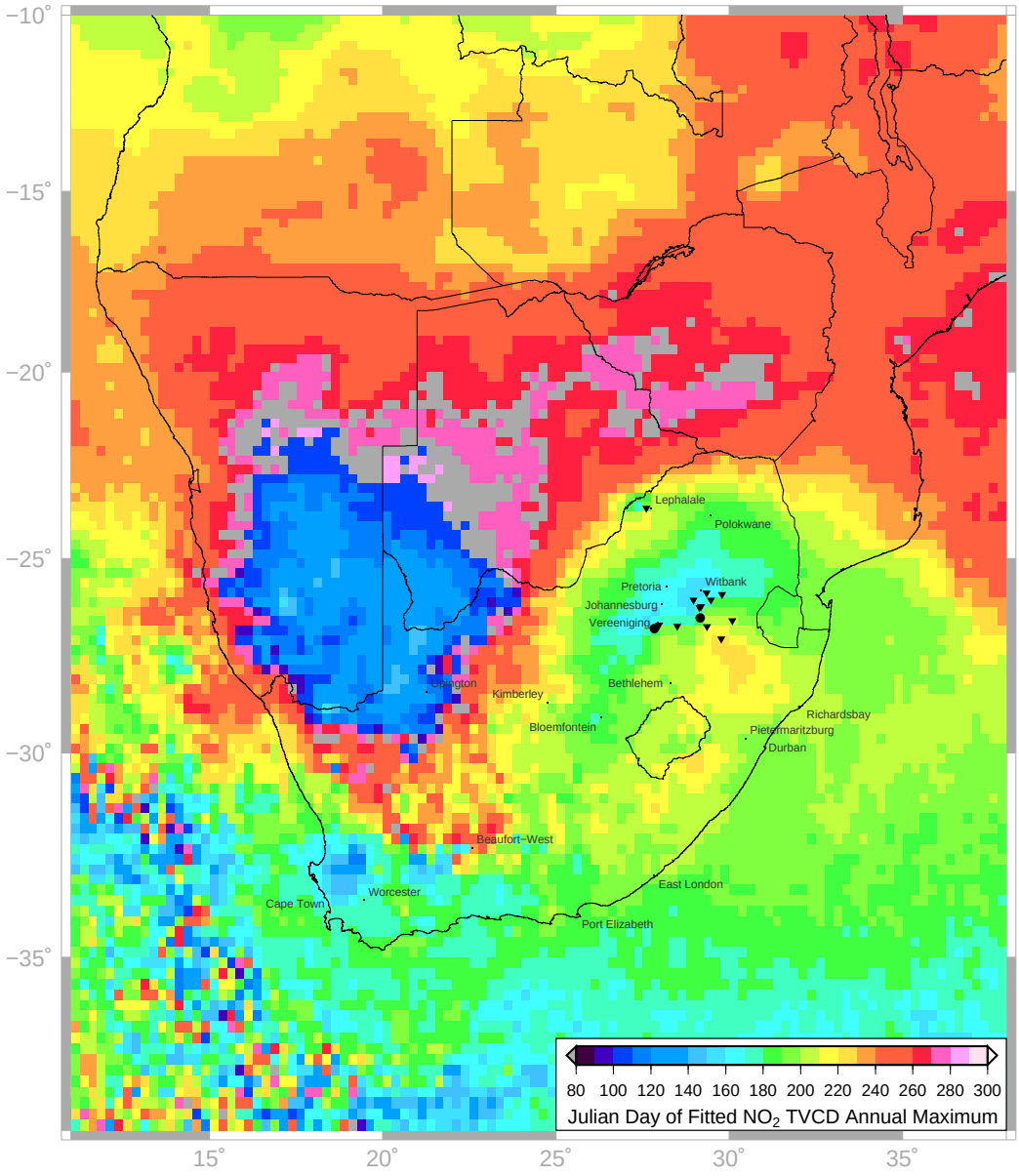


Figure 4.10: Julian day of the seasonal $NO_2$ TVCD peak fitted to OMI Level 3 data between 1 January 2005 and 31 December 2013.

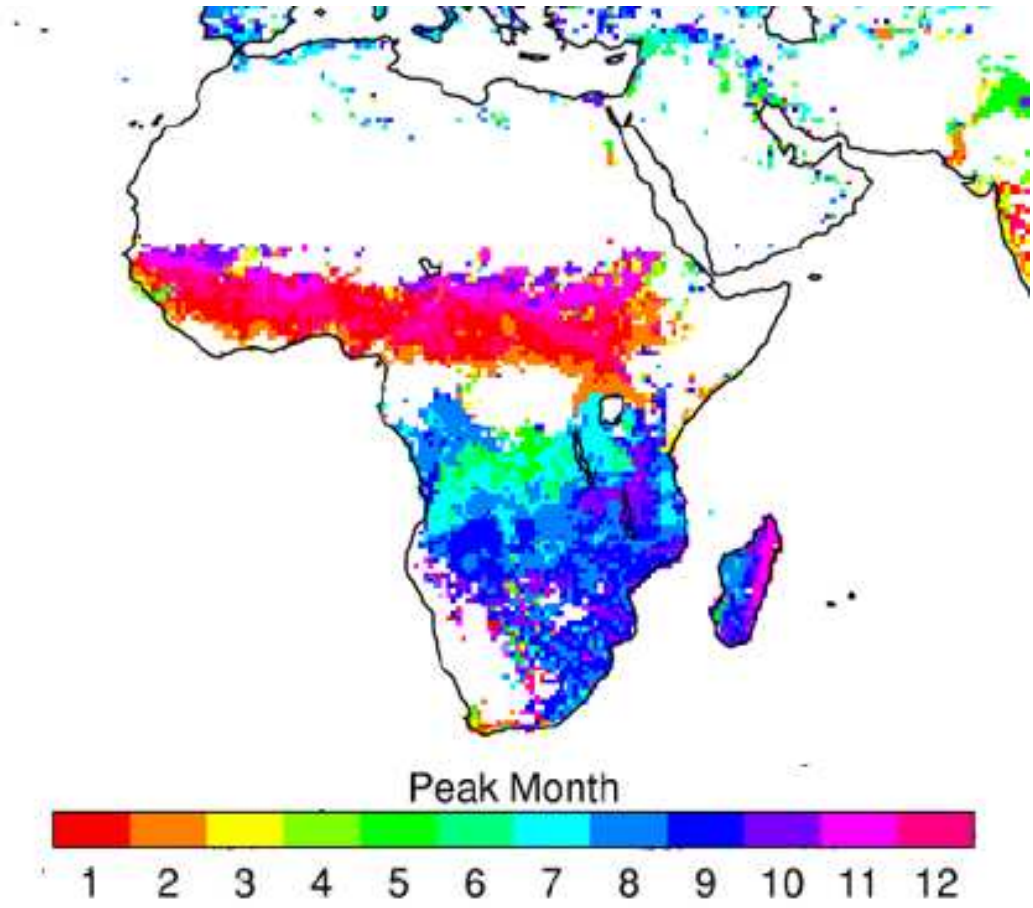


Figure 4.11: The month of peak fire counts from Terra MODIS (after Giglio *et al.* (2006)).

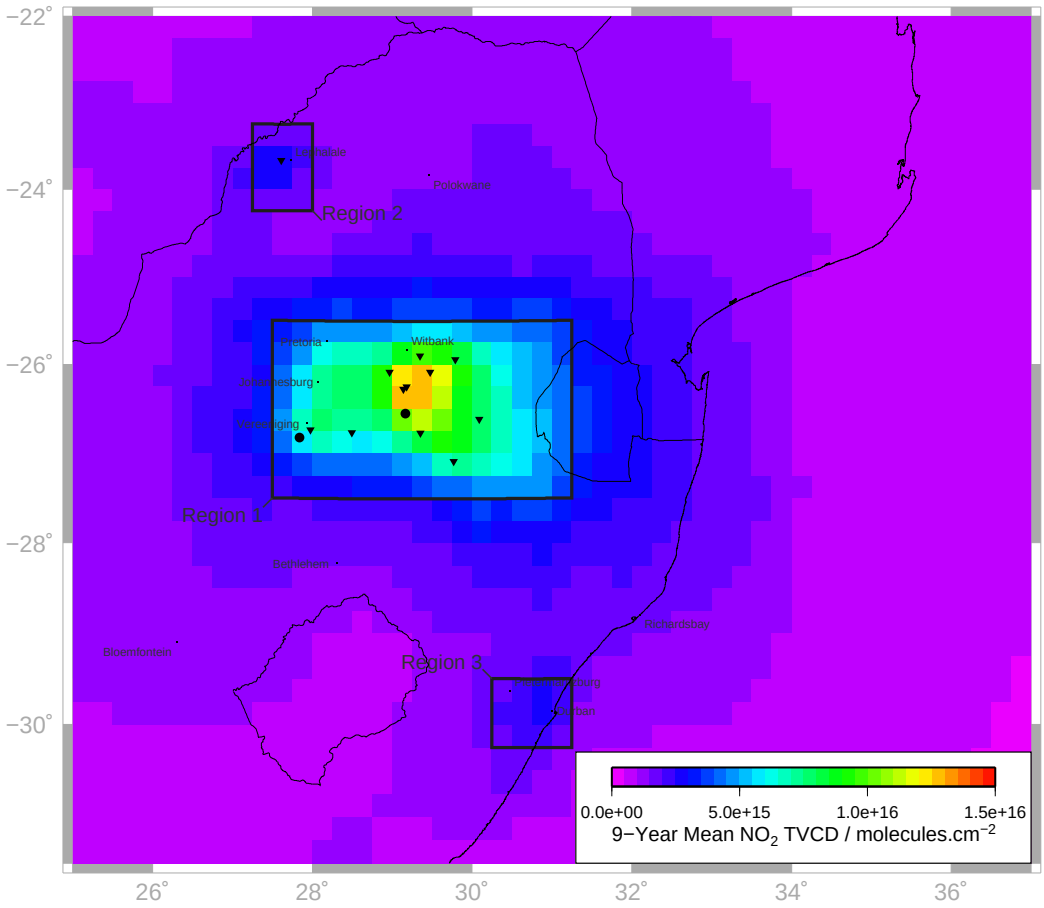


Figure 4.12: Mean tropospheric $NO_2$ vertical column density over the eastern part of South Africa calculated from OMI Level 3 data between 1 January 2005 and 31 December 2013.

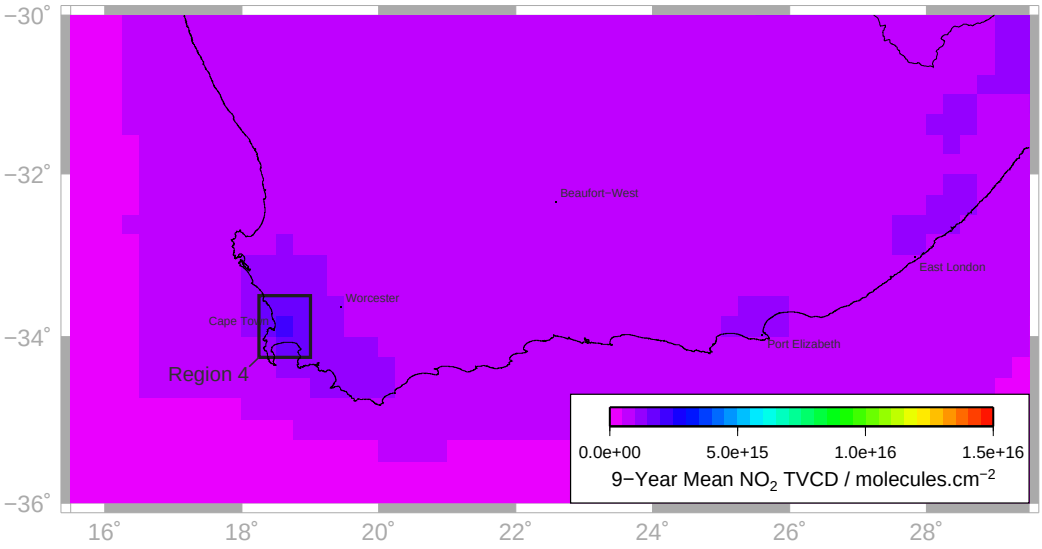


Figure 4.13: Mean tropospheric $NO_2$ vertical column density over the western and southern Cape calculated from OMI Level 3 data between 1 January 2005 and 31 December 2013.

ments as described in Section 2.3.2, allowing a linear trend to be established over the nine year period for each region, as well as parameters describing the amplitude of the seasonal variation, and the day of the year when the seasonal peak in $NO_2$ TVCD occurs.

Time-series plots for Regions 1, 2, 3 and 4 are shown in Figure 4.14. Note that the vertical scale used for Region 1 is larger than the others. Spatially-averaged daily measurements are shown as black dots, space- and time-averaged monthly values are shown as blue-green circles, and the fitted polynomial as an orange line. Fit parameters $\beta_1$ (linear trend), $\beta_2$ (seasonal amplitude), day of fitted peak (DFP), and the sum of squared errors (between the polynomial and daily data) are shown for each region. The latter parameter is difficult to interpret as a comparison between plots, since it will be influenced by the magnitudes and range of the daily measurements; however it is included for completeness.

Region 1 (greater Highveld) has the highest seasonal amplitude of the three, with monthly peak winter values around $1.9\times10^{16}$ molecules.cm$^{-2}$ and daily peak values around $2\times10^{16}$ molecules.cm$^{-2}$. The fitted polynomial shows a good correlation with the monthly mean values, bearing in mind that the polynomial was fitted to the daily data. A decreasing annual linear trend of -$6.4\times10^{13}$ molecules.cm$^{-2}$.y$^{-1}$ was found. The amplitude of the seasonal variation is $2.4\times10^{15}$ molecules.cm$^{-2}$, and the seasonal peak is on 6 July.

Region 2 (Matimba power station) has a seasonal amplitude of $4.6\times10^{14}$ molecules.cm$^{-2}$, close to an order of magnitude smaller than Region 1. Daily winter peak values are up to $1\times10^{16}$ molecules.cm$^{-2}$. The linear trend over the nine years is -$1.5\times10^{13}$ molecules.cm$^{-2}$.y$^{-1}$. The date of the peak is on 27 July.

The seasonal amplitude in the region around Durban and Pietermaritzburg (Region 3) is smaller than the Highveld, at $1.3\times10^{15}$ molecules.cm$^{-2}$, and the linear trend is -$2.9\times10^{13}$ molecules.cm$^{-2}$.y$^{-1}$. Daily winter peak values are up to $1.4\times10^{13}$ molecules.cm$^{-2}$. The winter peak $NO_2$ TVCD is on 15 July.

Region 4 (Cape Town) has a seasonal amplitude of $6.2\times10^{14}$ molecules.cm$^{-2}$, slightly larger than Matimba power station. Daily peak values in winter are up to $8\times10^{15}$ molecules.cm$^{-2}$. The annual peak of the fitted curve is on 20 June. A decreasing linear trend of -$3.6\times10^{13}$ molecules.cm$^{-2}$.y$^{-1}$ is found over the nine-year period.

Further regions of interest are defined in Figure 4.15, based on areas of decreasing and increasing linear trend. The Highveld has adjacent areas with increasing and decreasing trends. A similar spatial pattern has been reported previously over the Highveld based on GOME and SCIAMACHY data for the years 1996 to 2002 (Richter *et al.* 2005), but was not explored further. Regions 5 and 6 have a decreasing trend and are the areas of Johannesburg-Pretoria, and Witbank-Secunda respectively. Region 7 is around Grootvlei power station, with an increasing trend; and Regions 8 (Piet Retief), 9 (Mkuze) and 10 (Indian Ocean) approximate the locus of the plume exiting the sub-continent over the Indian Ocean. Regions 1, 2, and 3 are also indicated in Figure 4.15. Also indicated are the sites of the monitoring stations described by (Balashov *et al.* 2014).

Surface ozone measurements analysed by Balashov *et al.* (2014) indicate no significant long-term trends, from which one might infer that there is no significant trend in surface $NO_x$, since $NO_x$ is the limiting ozone precursor. Given this, apparent trends in the satellite $NO_2$ record must originate higher up in the atmospheric column.

Time-series plots of daily, monthly, and fitted $NO_2$ TVCD for Regions 5, 6 and 7 are shown in Figure 4.16. Region 5 (Johannesburg, Pretoria) shows a decreasing linear trend over the nine-year period of -$1.6\times10^{14}$ molecules.cm$^{-2}$. y$^{-1}$. The seasonal amplitude is $3.3\times10^{15}$ molecules.cm$^{-2}$, and the winter peak of the fitted curve is on 16 June. Peak daily values in winter are around $2\times10^{16}$ molecules.cm$^{-2}$, with occasional days of $NO_2$ TVCD reaching $3\times10^{16}$

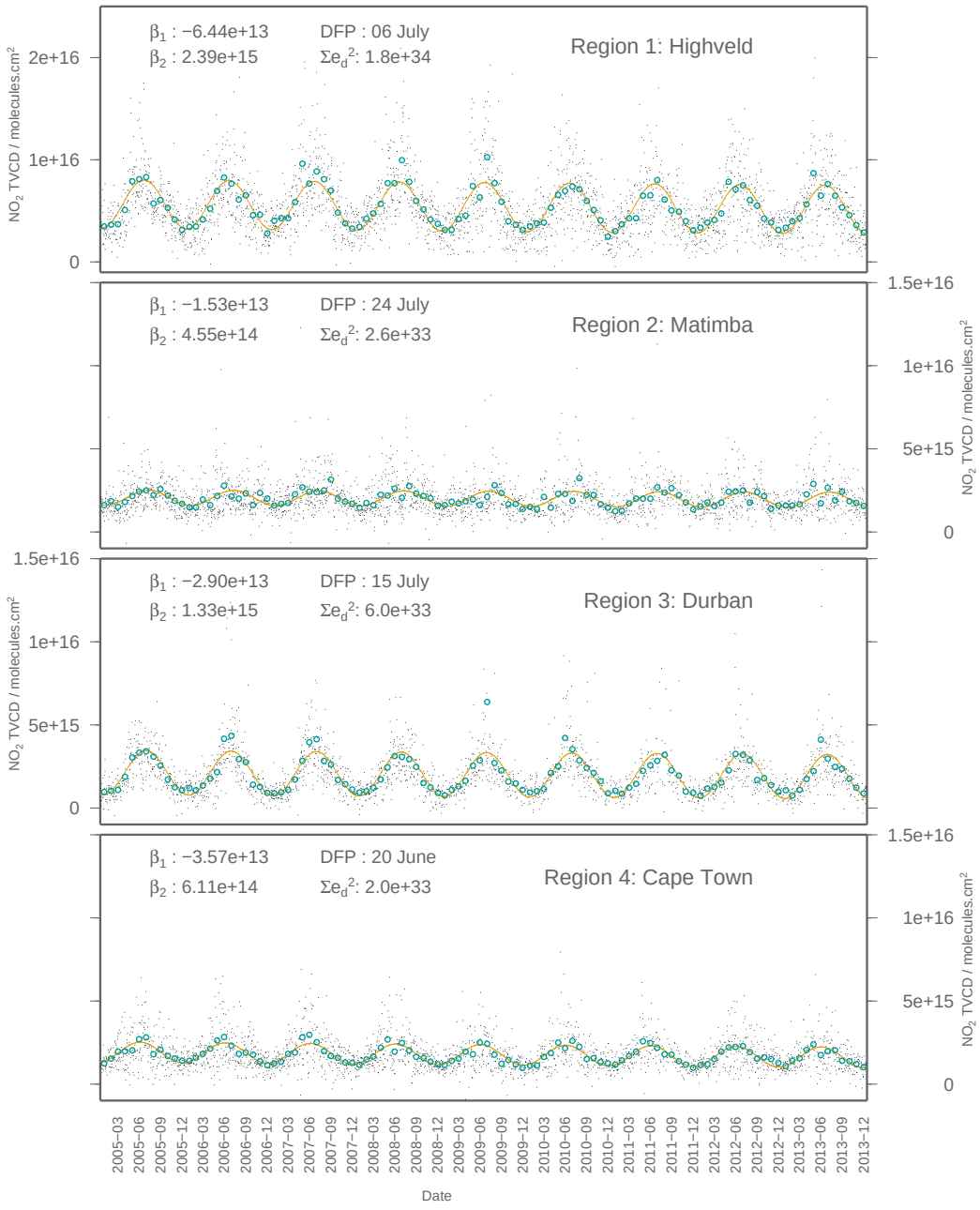


Figure 4.14: Time-series of spatially-averaged OMI Level 3 $NO_2$ data in the three regions shown in Figure 4.12 as well as Region 4 shown in Figure 4.13. Daily measured values are shown as black dots, monthly means as blue-green circles and the polynomial fitted to the daily measurements as an orange line. Fit parameters describe the linear trend, amplitude, date of the seasonal peak and sum of squared errors

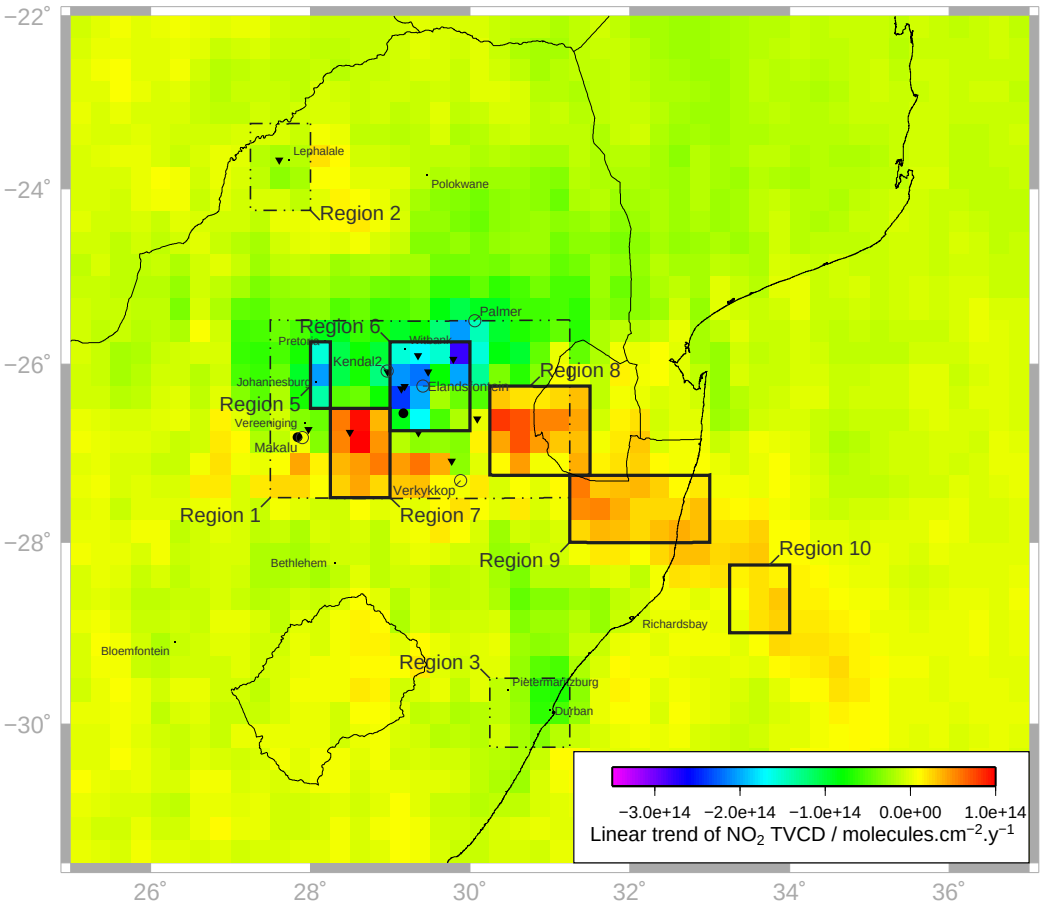


Figure 4.15: A map of linear trend in OMI $NO_2$ TVCD over the Highveld from January 2005 to December 2013, showing adjacent areas of increase and decrease. Six new regions of interest are defined. The positions of surface monitoring stations used by (Balashov *et al.* 2014) are shown.

molecules.cm$^{-2}$. Over the nine-year time period analysed, the daily peak values appear to be decreasing.

Region 6 around Witbank has a decreasing linear trend in $NO_2$ TVCD of -1.5×10$^{14}$ molecules.cm$^{-2}$.y$^{-1}$. Seasonal amplitude within this region is 3.5×10$^{15}$ molecules.cm$^{-2}$, and the winter peak of the fitted curve is on 4 July. Daily winter peak values are around 2×10$^{16}$ molecules.cm$^{-2}$, with occasional days around 3×10$^{16}$ molecules.cm$^{-2}$. The frequency of these high peak values appears to be decreasing over the time period analysed.

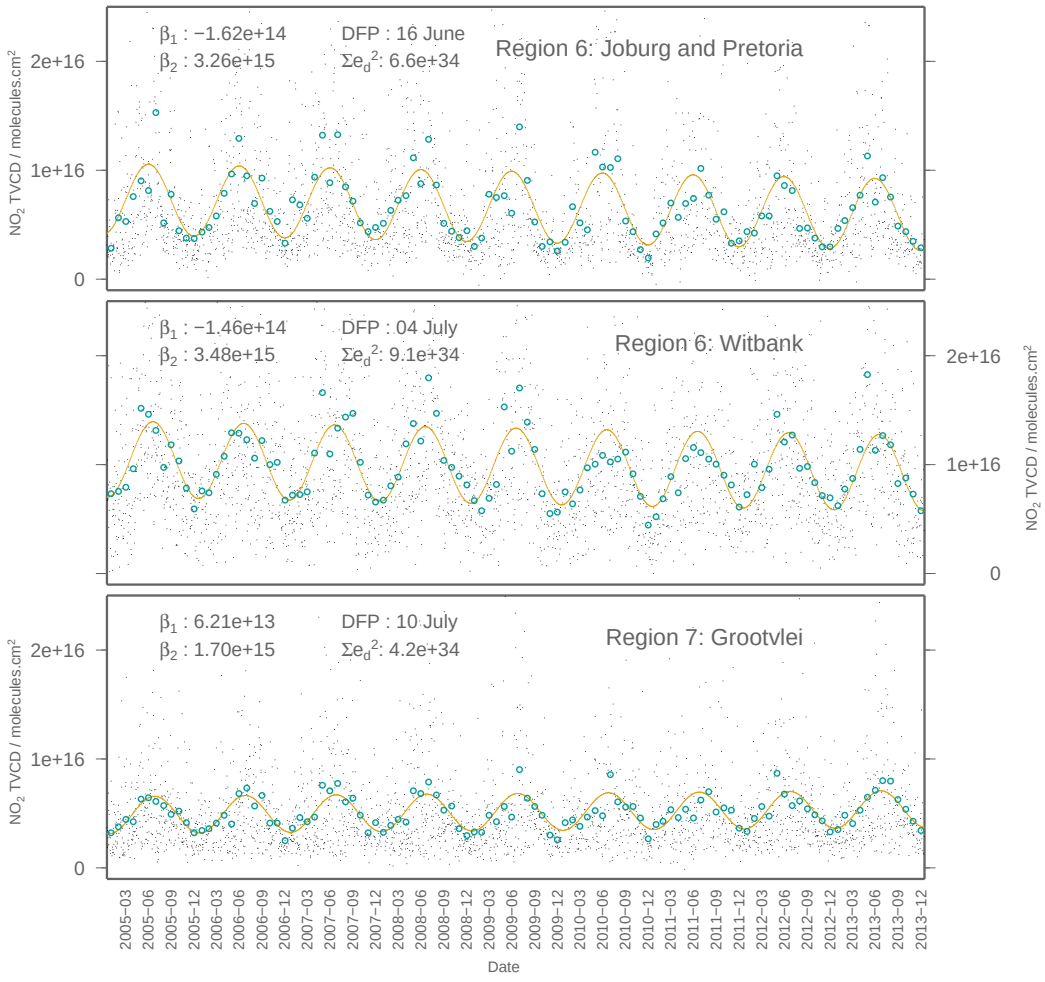


Figure 4.16: Time-series of spatially-averaged OMI Level 3 $NO_2$ data in Regions 5, 6 and 7 defined in Figure 4.15. Daily measured values are shown as black dots, monthly means as blue-green circles and the polynomial fitted to the daily measurements as an orange line. Fit parameters describe the linear trend, amplitude, date of the seasonal peak and sum of squared errors.

Referring now to Figure 4.17, Region 8 (Piet Retief) has an increasing linear trend over the nine year period of $4.62\times10^{13}$ molecules.cm$^{-2}$.y$^{-1}$ and the seasonal amplitude of $NO_2$ TVCD within this region is $2.73\times10^{15}$ molecules.cm$^{-2}$. Peak $NO_2$ is on 16 July. Further downwind, Region 9 (Mkuze) also shows an increase in $NO_2$ TVCD of $3.51\times10^{13}$ molecules.cm$^{-2}$.y$^{-1}$ and a seasonal amplitude of $1.54\times10^{15}$ molecules.cm$^{-2}$. The peak $NO_2$ is slightly later, on 21 July. Over the Indian Ocean (Region 10), the linear trend is positive: $1.58\times10^{13}$ molecules.cm$^{-2}$.y$^{-1}$, with a lower seasonal amplitude of $9\times10^{14}$ molecules.cm$^{-2}$. The peak $NO_2$ in this region is on 18 July.

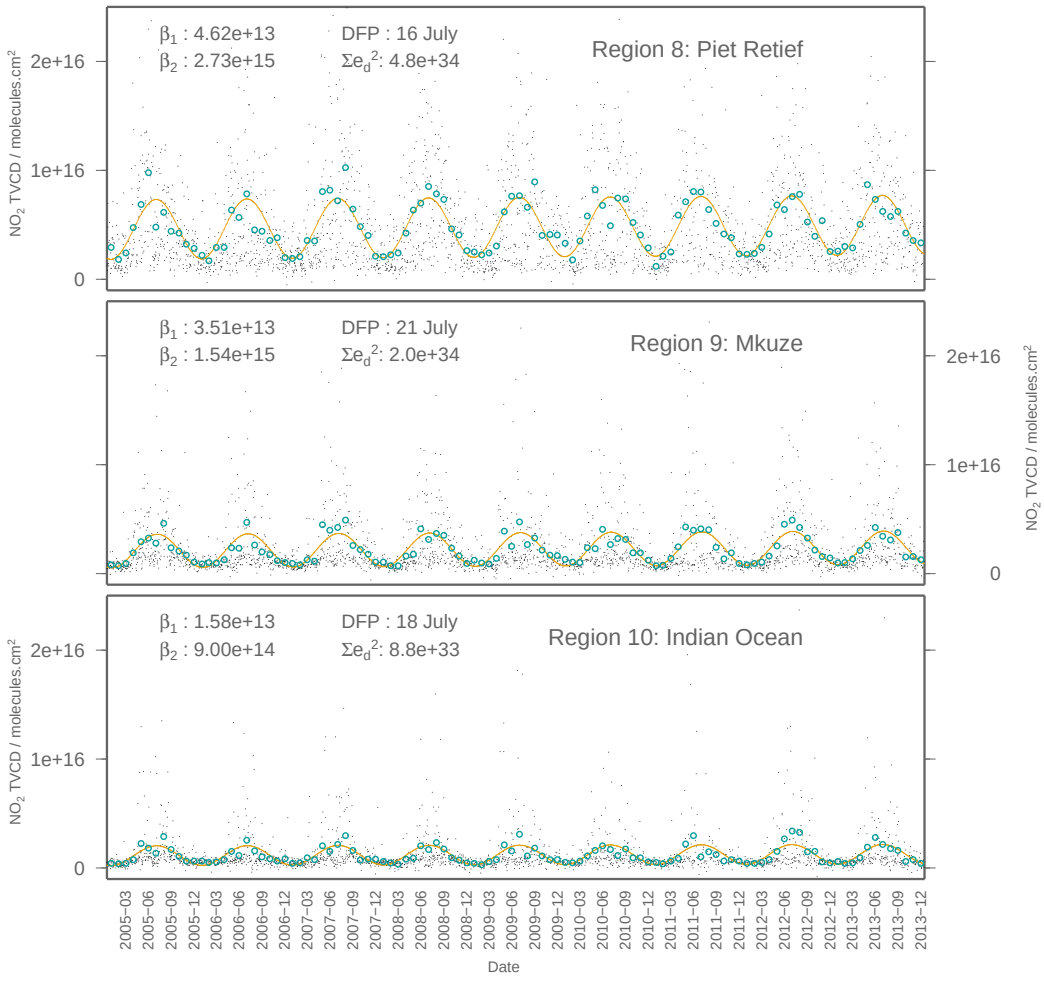


Figure 4.17: Time-series of spatially-averaged OMI Level 3 $NO_2$ data in Regions 8, 9 and 10 defined in Figure 4.15. Daily measured values are shown as black dots, monthly means as blue-green circles and the polynomial fitted to the daily measurements as an orange line. Fit parameters describe the linear trend, amplitude, date of the seasonal peak and sum of squared errors.

Table 4.1: Additional Radiative Transfer Scenarios

| Scenario | $NO_2$ Profile Shape | Aerosol Profile Shape | Surface Elevation | AOT |
|---|---|---|---|---|
| 4 | 1.5 km block | 1.5 km block | 1.5 km | 0.5 |
| 14 | 1.5 km block | 1.5 km block | 1.5 km | 0.75 |
| 24 | 1.5 km block | 1.5 km block | 1.5 km | 1.0 |
| 5 | 1.5 km block + EL | 1.5 km block + EL | 1.5 km | 0.5 |
| 15 | 1.5 km block + EL | 1.5 km block + EL | 1.5 km | 0.75 |
| 25 | 1.5 km block + EL | 1.5 km block + EL | 1.5 km | 1.0 |
| 9 | Exponential | Exponential | 1.5 km | 0.5 |
| 19 | Exponential | Exponential | 1.5 km | 0.75 |
| 29 | Exponential | Exponential | 1.5 km | 1.0 |
| 10 | Exponential + EL | Exponential + EL | 1.5 km | 0.5 |
| 20 | Exponential + EL | Exponential + EL | 1.5 km | 0.75 |
| 30 | Exponential + EL | Exponential + EL | 1.5 km | 1.0 |

A possible explanation for the anomaly in linear trend between Regions 5 and 6 (decreasing) and Regions 7 and 8 (increasing) could be that it is an artefact arising from a steady increase in aerosol loadings affecting radiative transfer through the atmosphere. To investigate this, radiative transfer model scenarios were designed, based on Scenarios 4, 5, 9 and 10 (i.e. the scenarios with the surface elevation at 1500m, presented in Section 3.2). The new scenarios are described in Table 4.1. Scenarios with aerosol optical thickness of 0.75 are named 14, 15, 19 and 20 to emphazise their relationship to the corresponding profiles. Scenarios 24, 25, 29 and 30 similarly are designed with aerosol optical thickness of 1.0. Radiative transfer modelling was done using these scenarios, as described in Section 2.2. Figure 4.18 shows the model results with these scenarios, with the surface albedo set at 0.05.

Region 7, aside from one power station providing an $NO_2$ source, is downwind (given the prevailing wind direction) of the source regions of Johannesburg and the Vaal Triangle. Similarly, Region 8 is downwind of Region 6, which encompasses six power stations and Secunda. One might expect that as plumes are advected further from their sources, they become more dispersed in both the horizontal plane and in the vertical. This implies, if we assume that there is an elevated layer of re-circulated aerosols and $NO_2$, that the radiative transfer scenario is changing from something approximating Scenario 10 nearby to sources, to something resembling Scenario 5 further downwind.

Scenario 5, and it's higher AOT siblings Scenarios 15 and 25, exhibit a in-

crease in AMF with increasing AOT. Therefore more scattering aerosols in the downwind regions will lead to an under-estimated AMF and, for a given SCD, an over-estimated VCD. A steady increase in AOT, if not accounted for, will lead to a steady increase in VCD in areas downwind of sources.

Scenarios 10, 20 and 30, exponential profiles of $NO_2$ and aerosols with an elevated layer at 2200m above the surface, exhibit a different trend in air-mass factor with changes in aerosol optical thickness. For a given SZA less than approximately 57°(SZA at the winter solstice over the Highveld is between 57° and 62°), an increase in aerosol loading leads to a decrease in air-mass factor, hence using the higher air-mass factor appropriate for a low-AOT atmosphere in the context of a high-AOT atmosphere will lead to a VCD that is too low. A steady increase in aerosol loading, if not accounted for, will result in an apparent decrease in VCD in source areas.

This possible artefact indicates that changes in AMF arising from changes in aerosols over time are important in the analysis of trends, in contrast to suggestions in the literature (van der A *et al.* 2006). The behaviour of the air-mass factor with respect to parameters such as surface albedo, AOT, presence of elevated layers, shape of the aerosol profile and SZA does not submit to an intuitive treatment. The radiative transfer modelling that is presented here indicates that the situation is more complex than it at first appears. However, the aerosol model used for radiative transfer calculations in the present study is simplistic, and the subject warrants further investigation. The discrepancies reported by Josipovic *et al.* (2013) between PANDORA, OMI, and surface in-situ $NO_x$measurements, as well as the mismatch between the surface (Balashov *et al.* 2014) and satellite trends, further indicate a systematic error arising from either an elevated plume or an artefact as described here.

The problem of statistical significance of trends is generally approached by analysis of autocorrelation of measurement noise (van der A *et al.* 2006, van der A *et al.* 2008, Ghude *et al.* 2008, Weatherhead *et al.* 1998), however the present problem is one of a change in the systematic error of the measurement, and such an approach may be of little value until the underlying driver of the trend is established. Furthermore, in this approach, noise is assumed to be generated by a stationary white-noise process. Inspection of the time-series in Figures 4.14, 4.16 and 4.17 makes it clear that the noise process is not stationary, but varies substantially with the seasons. No analysis of the significance of the trends described was attempted in the present study.

Figure 4.19 focusses on the Cape coastal area from Cape Town to East Lon-

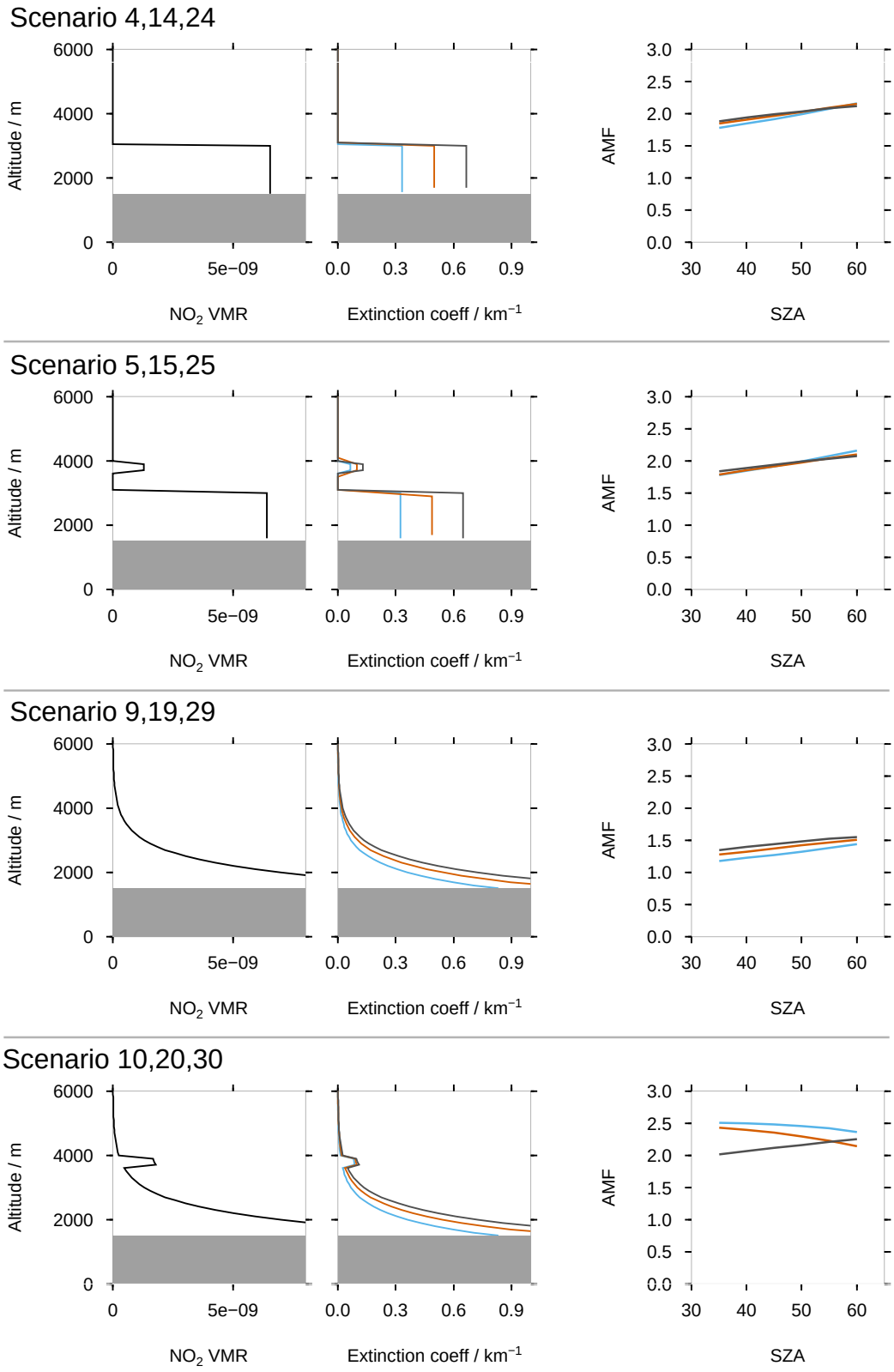


Figure 4.18: Air mass factors calculated for scenarios with AOT of 0.5, 0.75 and 1.0.

don. The previously-defined Region 4 is indicated, being the only contiguous region with any discernable trend. The fit parameters for Region 4 have already been discussed above in relation to Figure 4.14.

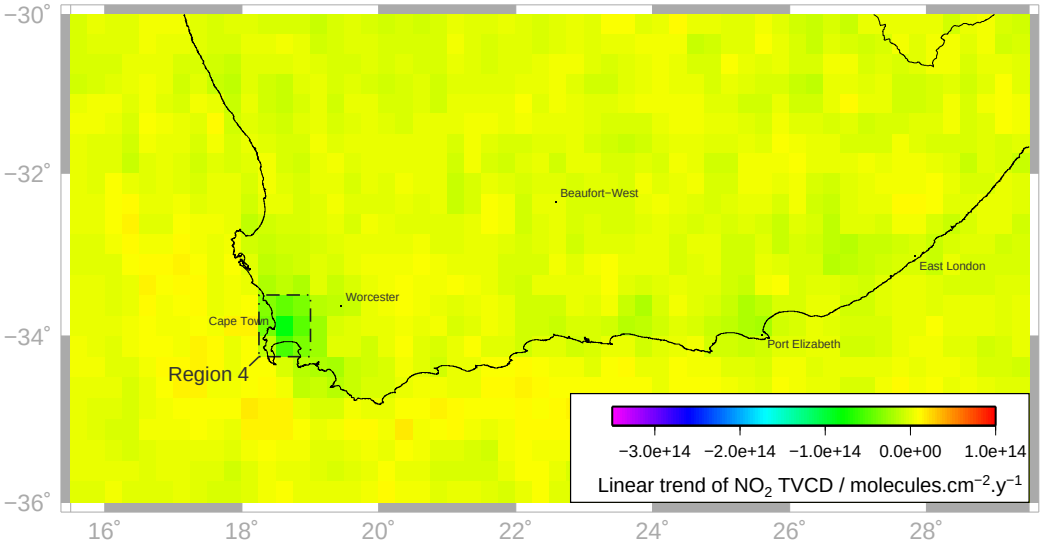


Figure 4.19: A map of linear trend in OMI $NO_2$ TVCD over the Cape coastal region from January 2005 to December 2013. Region 4 is indicated.

Figure 4.20 depicts the Julian day of the seasonal peak (similar to Figure 4.10), at a larger spatial scale and a narrower colour-scale to focus on the Highveld. The ROI previously highlighted in Figures 4.12 and 4.15 are shown. A new region around Bloemfontein (Region 11) is defined in Figure 4.20.

Focusing on region 2 around the town of Lephalale and the Matimba power station, it is interesting to note that the area immediately around the power station has a seasonal peak in $NO_2$ VCD that is 20 to 40 days earlier than the surrounding areas which are largely free of anthropogenic sources. One would expect the power station and its immediate surroundings to be subject to the same seasonal changes in meteorology. The power station, in contrast to the surrounding areas is a strong point source that has a constant $NO_2$ output year-round. The fact that the power station differs from its surroundings indicates that the date of the peak $NO_2$ VCD in the surrounding areas is driven by something other than meteorology. Region 11 (Bloemfontein) with a peak $NO_2$ in early July (i.e. during the dry season) surrounded by regions of later peak, indicates that an area of anthropogenic emissions can influence the day of the peak. Giglio *et al.* (2006) depict the months of peak fire count over most of the eastern half of South Africa to be August and September.

The gradient in day of peak between the area around Johannesburg-Pretoria-

Witbank (peak around mid-May to mid-June) towards the South African border with Botswana and Zimbabwe (where the peak occurs in early August), is in the opposite direction to the gradient from northern Angola, as discussed earlier. This could be an anthropogenic influence surrounding the Highveld corresponding to the area of enhanced mean $NO_2$ shown in Figure 4.12 on page 106. A large region of anthropogenic $NO_x$ source extending approximately to the northern border of South Africa is depicted by van der A *et al.* (2008).

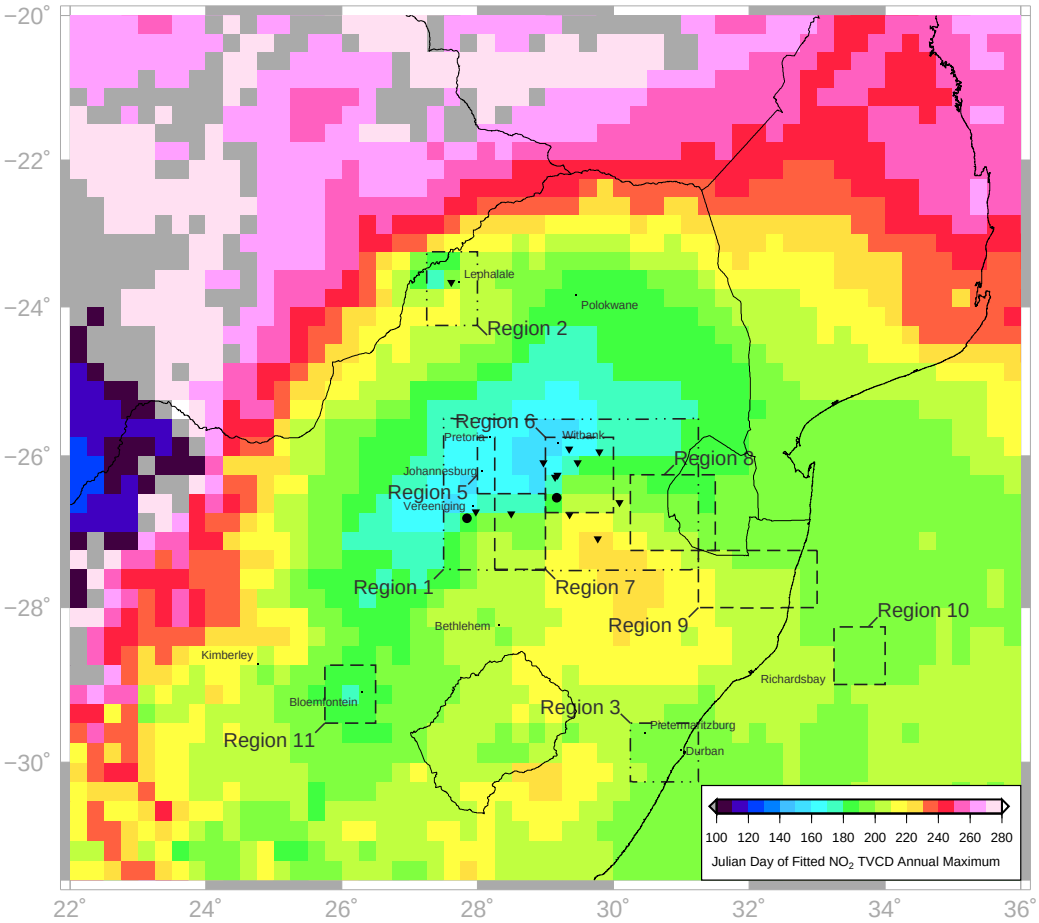


Figure 4.20: A map of the Julian day of peak fitted $NO_2$ over the Highveld. Previously examined regions of interest are indicated, and Region 11 is defined.

Julian day of the seasonal peak for the Cape region is shown in Figure 4.21. A new region (Region 12: Saldahna) to the north of the previously defined Cape Town region is defined, as a contiguous region of peak $NO_2$ around mid-May. The area of late-peak (first half of September) to the north-east of

this is the Karoo semi-desert. This date of peak is in sharp contrast to the Kalahari desert region further north, where the peak is in April-May. This shift in peak could be related to different vegetation or soil types.

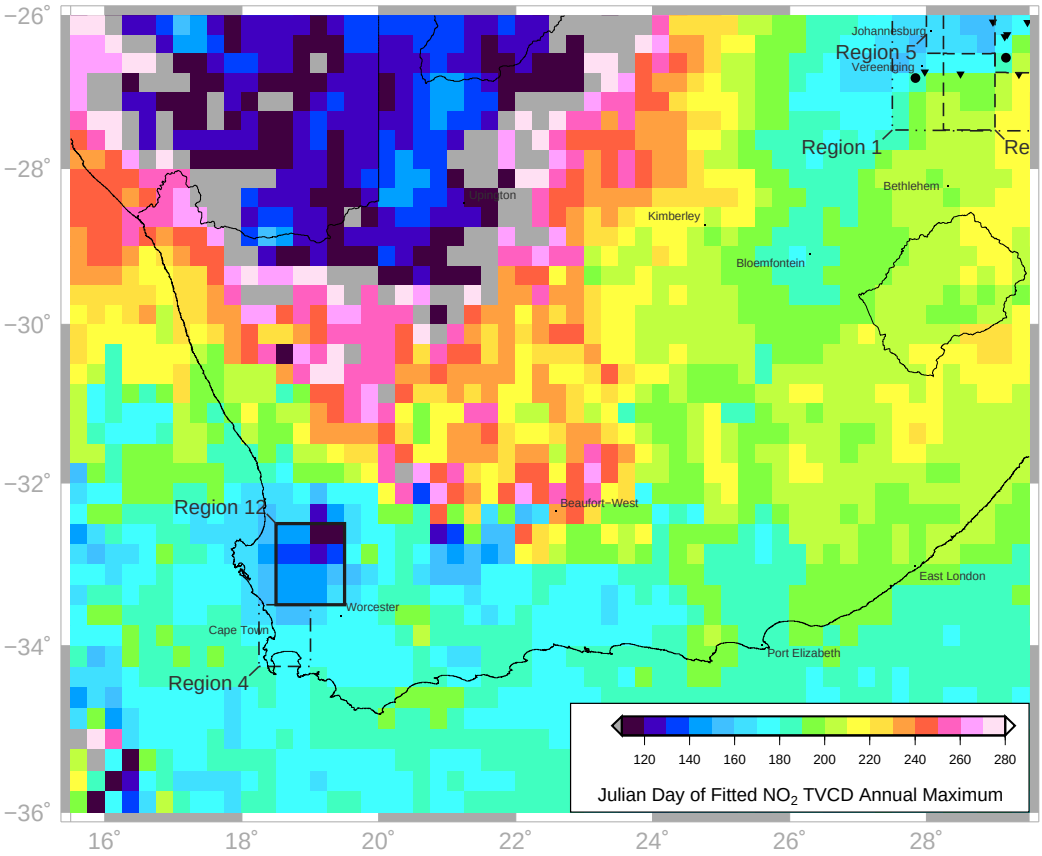


Figure 4.21: A map of the Julian day of peak fitted $NO_2$ over the Cape coastal region. Previously examined regions of interest are indicated, and Region 12 is defined.

Spatial- and time-averaging of daily $NO_2$ TVCD's was done in Region 11 and 12, as described above for the other regions of interest. The data are plotted in Figure 4.22, along with a fitted seasonal model. The region around Bloemfontein has a decreasing trend of -9.5×$10^{12}$ molecules.cm$^{-2}$.y$^{-1}$ and a seasonal amplitude of 3.1×$10^{14}$ molecules.cm$^{-2}$. The day of the fitted peak $NO_2$ is 6 July. Daily maximum values are around 1×$10^{16}$ molecules.cm$^{-2}$. Region 12 (Saldahna) has a decreasing trend of -4.6×$10^{12}$ molecules.cm$^{-2}$.y$^{-1}$, a seasonal amplitude of 1.1×$10^{14}$ molecules.cm$^{-2}$, and a seasonal peak on 20 May.

Given the seasonal differences in data coverage over the Highveld, as well as

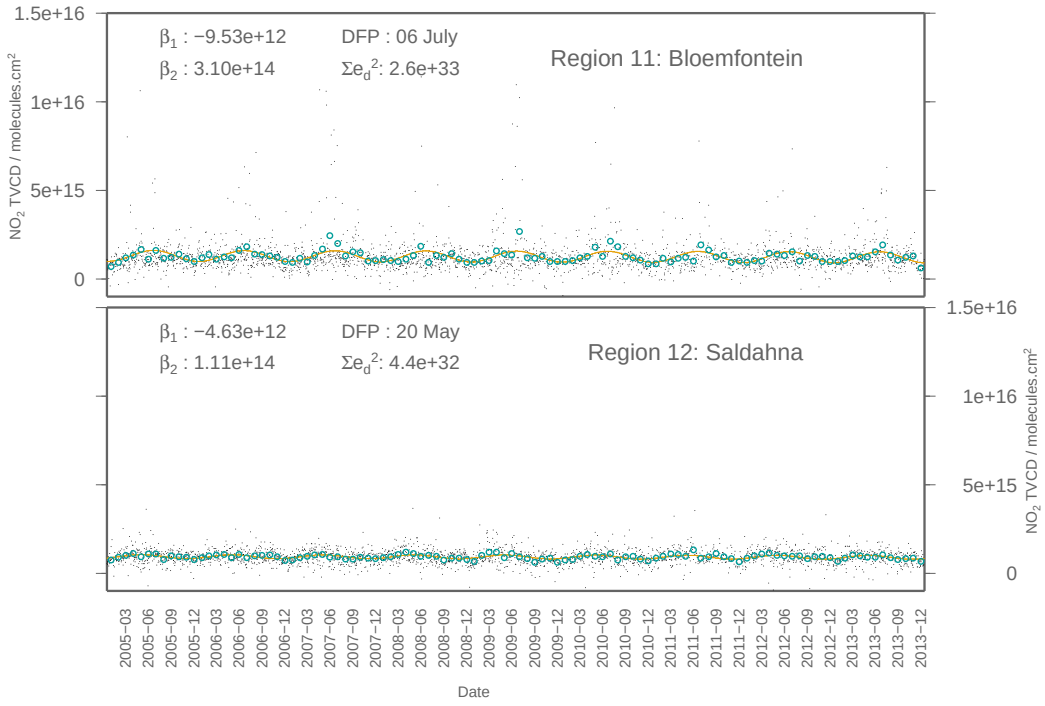


Figure 4.22: Time-series of spatially averaged $NO_2$ VCD for regions 11 and 12, defined in Figures 4.20 and 4.21. Daily measured values are shown as black dots, monthly means as blue-green circles and the polynomial fitted to the daily measurments as an orange line. Fit parameters describe the linear trend, amplitude, date of the seasonal peak and sum of squared errors.

the large seasonal amplitude of $NO_2$ TVCD, a bias towards the dry-season values might be expected. A correction of the 9-year mean is suggested: for each pixel, missing data was replaced with a climatalogical value calculated from the fitted equation in that pixel. A new mean value was then calculated for each pixel; the results are plotted in Figure 4.23. From inspection of this figure and of Figure 4.2 on page 93, it is not obvious what the changes are; the percentage difference between the conventional mean and the corrected mean is shown in Figure 4.24. Most of Southern Africa, including the Highveld, shows a small negative change of around 5 percent with this correction. An increase in the mean of around five percent is evident in a small region to the south-east of Cape Town. A region to the north-east of Witbank and over north-western Swaziland shows a decrease of around ten percent. The region around the KZN South Coast, Durban, Pietermaritzburg, and extending inland to the Drakensberg escarpment shows a decrease of between eight and ten percent. A larger correction is made in a band stretching from Angola across northern Zambia, with a broad reduction of around fifteen percent, with some areas' mean $NO_2$ reducing by more than 20 percent.

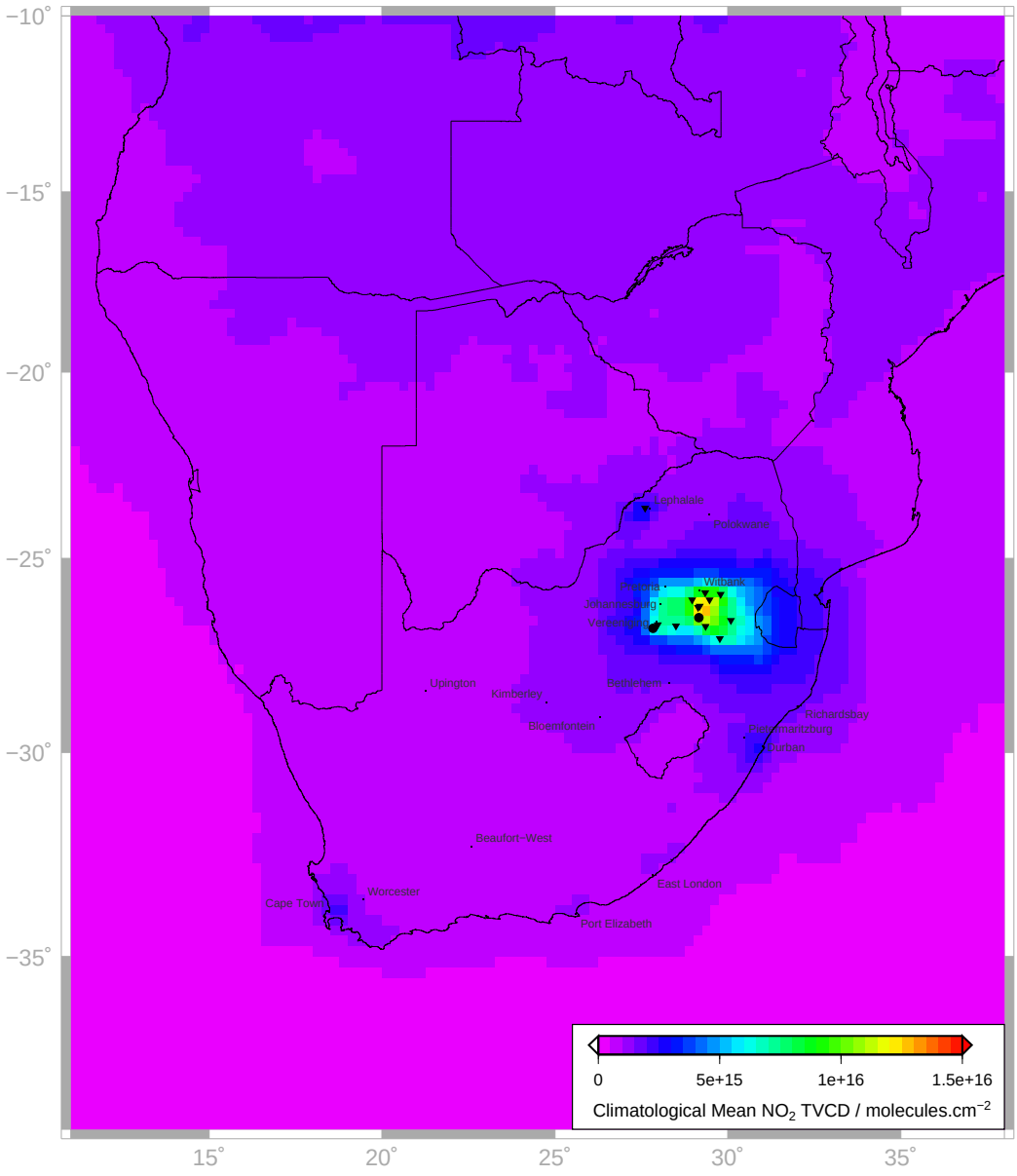


Figure 4.23: Mean tropospheric $NO_2$ from OMI level 3 data, with a correction applied to fill in days of missing data with the climatological value derived from a polynomial fit.

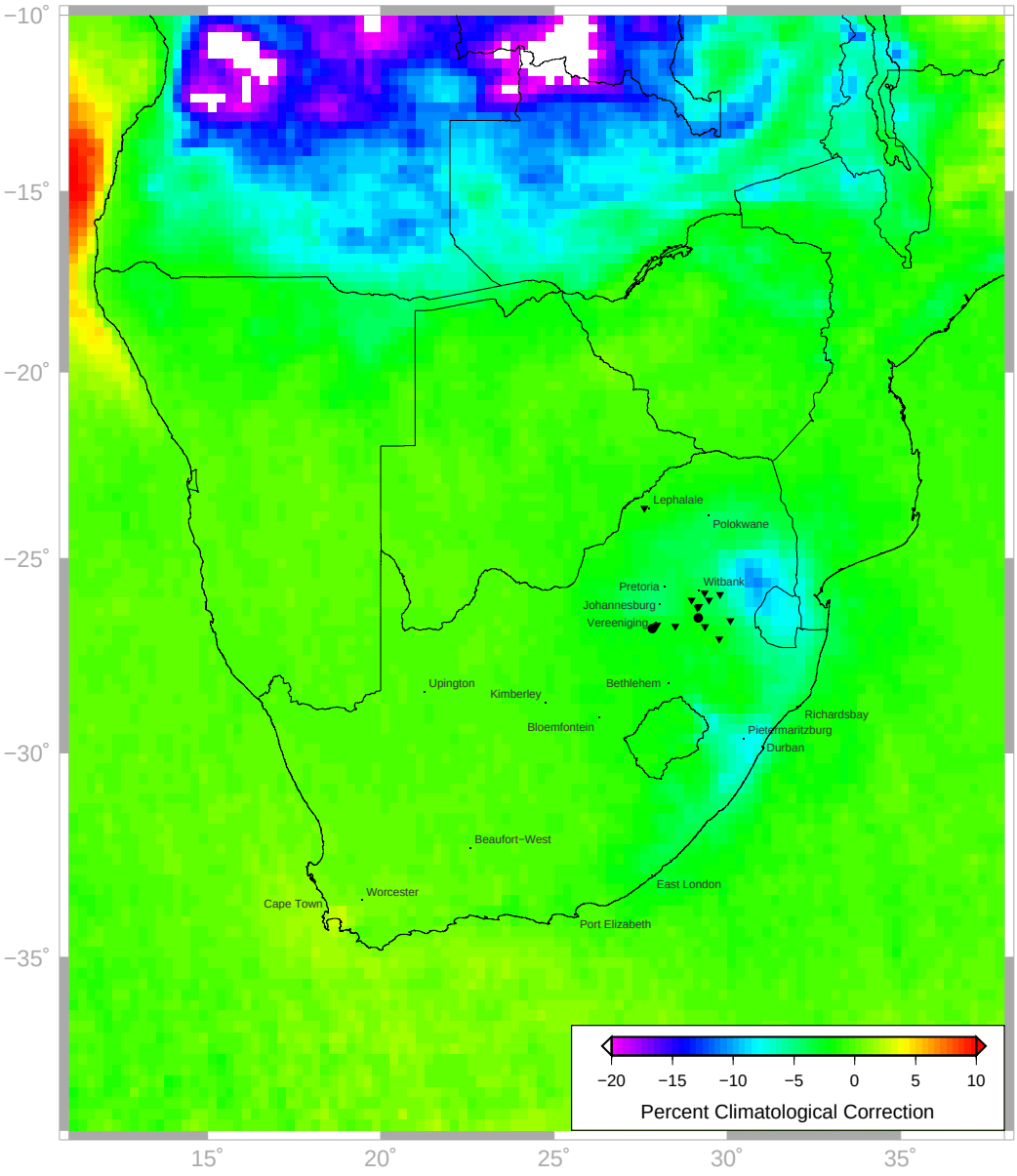


Figure 4.24: The percentage change between the mean in Figure 4.2 on page 93 and the corrected mean in Figure 4.23.

# Chapter 5

# Conclusions

Several flights were conducted using a research aircraft fitted with a nadir-viewing imaging DOAS instrument, in-situ $NO_y$ instrument, and an aerosol size spectrometer. Two flight strategies were followed: 1. A grid pattern to characterize the horizontal distribution of $NO_2$ on a regional scale 2. A straight line track with vertical profiles performed at either end, to characterize the vertical profile of aerosols and trace gases, and follow the track of the OMI and SCIAMACHY satellite instruments .

Four research questions were posed, these are addressed here.

1. Can source apportionment be done on a regional scale using high-resolution measurements of $NO_2$ vertical column densitites?

The first flight strategy has been demonstrated to allow identification of sources and apportioning of emissions. By inspection of the $NO_2$ Vertical Column Density (VCD) measurements plotted on a map, plumes can be traced to their origin. This technique depends on stable conditions and simple topography, which inhibit mixing of the plume with surrounding air. $NO_2$ flux has been estimated at 10 tons.hr$^{-1}$ 10 km downwind of Majuba power station, and 36 tons.hr$^{-!}$ the same distance downwind of the refinery at Secunda. Flux estimates for the Highveld as a whole of 395 tons.hr$^{-1}$ and 405 tons.hr$^{-1}$, were made using aircraft and satellite measurements respectively. It should be acknowledged that the errors in these estimates are likely to be very high.

2. Can plume observations by airborne DOAS be used to determine reaction rates?

Since there are multiple reaction pathways for the removal of $NO_2$ from the atmosphere, and of the species participating in these reactions, passive DOAS can only observe $NO_2$, reaction rates cannot be determined by airborne DOAS. By observing the change in $NO_2$ flux as a plume is advected downwind, conclusions can be drawn regarding the direction of the dominant reaction. Increasing $NO_2$ flux within a few hundred metres of the point of emission has been attributed to conversion of NO to $NO_2$ (Heue *et al.* 2008*a*), further downwind it appears that $NO_2$ is destroyed, most probably by reaction with the $OH$ radical.

3. Are satellite measurements of $NO_2$ over the Highveld subject to systematic biases, and what are the likely sources of such biases?

A sensitivity study using a radiative transfer model and a simple model of aerosols in the atmosphere showed that the shape of the aerosol profile has a significant effect on the Air-Mass Factor (AMF) for airborne DOAS measurements. Errors that might arise in $NO_2$ VCD from the use of an inappropriate AMF arising from incorrect profile shape are up to 167 percent in the worst case. Similar errors might be expected in satellite measurements, however, current satellite products include a sophisticated calculation of the AMF. Direct comparison of airborne iDOAS $NO_2$ measurements with satellite products from three different satellites show that a better match is found with OMI than with SCIAMACHY or GOME-2. This appears to be related to the spatial resolution of the satellite instruments. SCIAMACHY and GOME-2 with their larger pixel sizes give lower magnitudes of $NO_2$ VCD than OMI. Agreement between OMI and the airborne DOAS in general is good, although one should bear in mind that they suffer from the same sources of error. A complimentary technique for validation of $NO_2$ vertical column densities would be to use a $NO_2$ instrument with a photolytic converter to make in-situ measurements of the column.

Regions of increasing and decreasing trends were found in close proximity to each other on the Highveld. The cities of Johannesburg and Pretoria, as well as a region between Secunda and Witbank, and a region extending east of Witbank show a decreasing trend of $NO_2$ between January 2005 and December 2013. A region of increasing trend was found to the south-west of Secunda, extending west to the Vaal Triangle and east to Tutuka power station. An increasing trend was also found over the approximate locus of the plume leaving the Highveld over the Indian Ocean.

These adjacent areas of decreasing trend close to sources, and increasing trend downwind, can be explained as an artefact arising from an unexpected

effect of radiative transfer on the AMF, provided several conditions are met: 1. plume dispersion is such that the vertical profile of $NO_2$ and aerosols changes from an exponential decrease with height to a block-shaped profile 2. there is an elevated layer of $NO_2$ and aerosols about 2200 m above the surface 3. the surface elevation is around 1500 m 4. there is a steady increase in aerosol optical thickness over time. The first three conditions are easily demonstrated to be true, or have been observed in the present study and documented in the literature. The last is worthy of further investigation, since this aerosol effect on the AMF affecting the analysis of long term trends is in contrast to the literature (van der A *et al.* 2006).

A correction to the nine-year mean $NO_2$ was made. This was based on the precept that the mean is biased towards dry-season values, due to less cloud cover affecting the frequency of satellite measurements. Over the region of the Highveld with a high density of coal-fired power stations and the large urban complex of Johannesuburg, the effect of this correction was reduce the mean by around five percent. A similar correction factor was found over much of the sub-continent. Corrections in areas to the north-west of Swaziland, and around Durban and Pietermaritzburg were greater, between -8 percent to -10 percent. Cape Town required a positive correction of four percent. Corrections of -15 percent were made to a large area of Angola and Zambia. Isolated areas within these two countries required a reduction in the mean values of $NO_2$ of more that 20 percent.

4. What features can be identified in the satellite record, associated with known sources of $NO_2$?

Analysis of the satellite $NO_2$ record from nine years of OMI measurements found an area of high mean $NO_2$ over the Highveld, similar to previous studies. A higher mean $NO_2$ VCD was found around Matimba power station compared to the surrounding area. The areas around the urban centers of Durban and Pietermaritzburg, as well as East London, Port Elizabeth and greater Cape Town were also found to have enhancements in mean $NO_2$ VCD compared to their surroundings.

The amplitude of seasonal variation in $NO_2$ VCD is found to be highest around the eastern Highveld and the city of Johannesburg. The area of increased amplitude extends to the east of the Highveld, which is attributed to predominantly easterly transport of $NO_2$ from the Highveld. Durban is also found to have high seasonal variability, with the other urban centres of Cape Town, Port Elizabeth and East London showing greater variability than their surroundings. Matimba power station near to Lephalale appears

to have an area of higher variability associated with it. A large area of the Kalahari and Namib deserts have very low variability. A seasonal signature of biomass burning can be found by comparing winter maxima with the summer maxima: high winter maxima, which have no corresponding high summer maximum are attributed to biomass burning.

The trend in $NO_2$ VCD was analysed over the nine year period. Trends in areas surrounding the Highveld have been discussed above in relation to the previous research question. Other regions with identifiable trends are the cities of Cape Town and Durban, both with decreasing trends. The area immediately around Matimba power station has a decreasing trend, further to the south-east, an increasing trend.

Analysis of the day of the seasonal peak in $NO_2$ measured by the satellite revealed several patterns. A signature of biomass burning was found corresponding to that in the fire count data. From northern Angola, where the peak in fire counts is in June and July, through Namibia, Botswana and Zimbabwe, where the peak is in August and September, a gradient in the day of peak $NO_2$ is found approximately matching the fire data. This gradient stops at the border with South Africa, where a steeper gradient in the opposite direction is attributed to anthropogenic influence. The Kalahari and Namib deserts form a contiguous region of peak $NO_2$ around May, while the arid Karoo region's peak is in September.

The presence of a "hotspot" of $NO_2$ over the Highveld is confirmed. Without the use of a chemical transport model, a technique that is typically used for calculation of a top-down inventory using satellite measurements, emissions can be estimated and sources identified. A more sophisticated treatment of aerosols in the calculation of an air-mass factor, which is shown in the literature to be warranted, will require an in-situ climatology of aerosol size distributions and optical properties.

# Appendix A

# Table of Julian Days

Table A.1: Julian day table for non-leap years

| | | | | | | | | | | | | | |
|---|---|---|---|---|---|---|---|---|---|---|---|---|---|
| **1** | 1 Jan | **55** | 24 Feb | **109** | 19 Apr | **163** | 12 Jun | **217** | 5 Aug | **271** | 28 Sep | **325** | 21 Nov |
| **2** | 2 Jan | **56** | 25 Feb | **110** | 20 Apr | **164** | 13 Jun | **218** | 6 Aug | **272** | 29 Sep | **326** | 22 Nov |
| **3** | 3 Jan | **57** | 26 Feb | **111** | 21 Apr | **165** | 14 Jun | **219** | 7 Aug | **273** | 30 Sep | **327** | 23 Nov |
| **4** | 4 Jan | **58** | 27 Feb | **112** | 22 Apr | **166** | 15 Jun | **220** | 8 Aug | **274** | 1 Oct | **328** | 24 Nov |
| **5** | 5 Jan | **59** | 28 Feb | **113** | 23 Apr | **167** | 16 Jun | **221** | 9 Aug | **275** | 2 Oct | **329** | 25 Nov |
| **6** | 6 Jan | **60** | 1 Mar | **114** | 24 Apr | **168** | 17 Jun | **222** | 10 Aug | **276** | 3 Oct | **330** | 26 Nov |
| **7** | 7 Jan | **61** | 2 Mar | **115** | 25 Apr | **169** | 18 Jun | **223** | 11 Aug | **277** | 4 Oct | **331** | 27 Nov |
| **8** | 8 Jan | **62** | 3 Mar | **116** | 26 Apr | **170** | 19 Jun | **224** | 12 Aug | **278** | 5 Oct | **332** | 28 Nov |
| **9** | 9 Jan | **63** | 4 Mar | **117** | 27 Apr | **171** | 20 Jun | **225** | 13 Aug | **279** | 6 Oct | **333** | 29 Nov |
| **10** | 10 Jan | **64** | 5 Mar | **118** | 28 Apr | **172** | 21 Jun | **226** | 14 Aug | **280** | 7 Oct | **334** | 30 Nov |
| **11** | 11 Jan | **65** | 6 Mar | **119** | 29 Apr | **173** | 22 Jun | **227** | 15 Aug | **281** | 8 Oct | **335** | 1 Dec |
| **12** | 12 Jan | **66** | 7 Mar | **120** | 30 Apr | **174** | 23 Jun | **228** | 16 Aug | **282** | 9 Oct | **336** | 2 Dec |
| **13** | 13 Jan | **67** | 8 Mar | **121** | 1 May | **175** | 24 Jun | **229** | 17 Aug | **283** | 10 Oct | **337** | 3 Dec |
| **14** | 14 Jan | **68** | 9 Mar | **122** | 2 May | **176** | 25 Jun | **230** | 18 Aug | **284** | 11 Oct | **338** | 4 Dec |
| **15** | 15 Jan | **69** | 10 Mar | **123** | 3 May | **177** | 26 Jun | **231** | 19 Aug | **285** | 12 Oct | **339** | 5 Dec |
| **16** | 16 Jan | **70** | 11 Mar | **124** | 4 May | **178** | 27 Jun | **232** | 20 Aug | **286** | 13 Oct | **340** | 6 Dec |
| **17** | 17 Jan | **71** | 12 Mar | **125** | 5 May | **179** | 28 Jun | **233** | 21 Aug | **287** | 14 Oct | **341** | 7 Dec |
| **18** | 18 Jan | **72** | 13 Mar | **126** | 6 May | **180** | 29 Jun | **234** | 22 Aug | **288** | 15 Oct | **342** | 8 Dec |
| **19** | 19 Jan | **73** | 14 Mar | **127** | 7 May | **181** | 30 Jun | **235** | 23 Aug | **289** | 16 Oct | **343** | 9 Dec |
| **20** | 20 Jan | **74** | 15 Mar | **128** | 8 May | **182** | 1 Jul | **236** | 24 Aug | **290** | 17 Oct | **344** | 10 Dec |
| **21** | 21 Jan | **75** | 16 Mar | **129** | 9 May | **183** | 2 Jul | **237** | 25 Aug | **291** | 18 Oct | **345** | 11 Dec |
| **22** | 22 Jan | **76** | 17 Mar | **130** | 10 May | **184** | 3 Jul | **238** | 26 Aug | **292** | 19 Oct | **346** | 12 Dec |
| **23** | 23 Jan | **77** | 18 Mar | **131** | 11 May | **185** | 4 Jul | **239** | 27 Aug | **293** | 20 Oct | **347** | 13 Dec |
| **24** | 24 Jan | **78** | 19 Mar | **132** | 12 May | **186** | 5 Jul | **240** | 28 Aug | **294** | 21 Oct | **348** | 14 Dec |
| **25** | 25 Jan | **79** | 20 Mar | **133** | 13 May | **187** | 6 Jul | **241** | 29 Aug | **295** | 22 Oct | **349** | 15 Dec |
| **26** | 26 Jan | **80** | 21 Mar | **134** | 14 May | **188** | 7 Jul | **242** | 30 Aug | **296** | 23 Oct | **350** | 16 Dec |
| **27** | 27 Jan | **81** | 22 Mar | **135** | 15 May | **189** | 8 Jul | **243** | 31 Aug | **297** | 24 Oct | **351** | 17 Dec |
| **28** | 28 Jan | **82** | 23 Mar | **136** | 16 May | **190** | 9 Jul | **244** | 1 Sep | **298** | 25 Oct | **352** | 18 Dec |
| **29** | 29 Jan | **83** | 24 Mar | **137** | 17 May | **191** | 10 Jul | **245** | 2 Sep | **299** | 26 Oct | **353** | 19 Dec |
| **30** | 30 Jan | **84** | 25 Mar | **138** | 18 May | **192** | 11 Jul | **246** | 3 Sep | **300** | 27 Oct | **354** | 20 Dec |
| **31** | 31 Jan | **85** | 26 Mar | **139** | 19 May | **193** | 12 Jul | **247** | 4 Sep | **301** | 28 Oct | **355** | 21 Dec |
| **32** | 1 Feb | **86** | 27 Mar | **140** | 20 May | **194** | 13 Jul | **248** | 5 Sep | **302** | 29 Oct | **356** | 22 Dec |
| **33** | 2 Feb | **87** | 28 Mar | **141** | 21 May | **195** | 14 Jul | **249** | 6 Sep | **303** | 30 Oct | **357** | 23 Dec |
| **34** | 3 Feb | **88** | 29 Mar | **142** | 22 May | **196** | 15 Jul | **250** | 7 Sep | **304** | 31 Oct | **358** | 24 Dec |
| **35** | 4 Feb | **89** | 30 Mar | **143** | 23 May | **197** | 16 Jul | **251** | 8 Sep | **305** | 1 Nov | **359** | 25 Dec |
| **36** | 5 Feb | **90** | 31 Mar | **144** | 24 May | **198** | 17 Jul | **252** | 9 Sep | **306** | 2 Nov | **360** | 26 Dec |
| **37** | 6 Feb | **91** | 1 Apr | **145** | 25 May | **199** | 18 Jul | **253** | 10 Sep | **307** | 3 Nov | **361** | 27 Dec |
| **38** | 7 Feb | **92** | 2 Apr | **146** | 26 May | **200** | 19 Jul | **254** | 11 Sep | **308** | 4 Nov | **362** | 28 Dec |
| **39** | 8 Feb | **93** | 3 Apr | **147** | 27 May | **201** | 20 Jul | **255** | 12 Sep | **309** | 5 Nov | **363** | 29 Dec |
| **40** | 9 Feb | **94** | 4 Apr | **148** | 28 May | **202** | 21 Jul | **256** | 13 Sep | **310** | 6 Nov | **364** | 30 Dec |
| **41** | 10 Feb | **95** | 5 Apr | **149** | 29 May | **203** | 22 Jul | **257** | 14 Sep | **311** | 7 Nov | **365** | 31 Dec |
| **42** | 11 Feb | **96** | 6 Apr | **150** | 30 May | **204** | 23 Jul | **258** | 15 Sep | **312** | 8 Nov | | |
| **43** | 12 Feb | **97** | 7 Apr | **151** | 31 May | **205** | 24 Jul | **259** | 16 Sep | **313** | 9 Nov | | |
| **44** | 13 Feb | **98** | 8 Apr | **152** | 1 Jun | **206** | 25 Jul | **260** | 17 Sep | **314** | 10 Nov | | |
| **45** | 14 Feb | **99** | 9 Apr | **153** | 2 Jun | **207** | 26 Jul | **261** | 18 Sep | **315** | 11 Nov | | |
| **46** | 15 Feb | **100** | 10 Apr | **154** | 3 Jun | **208** | 27 Jul | **262** | 19 Sep | **316** | 12 Nov | | |
| **47** | 16 Feb | **101** | 11 Apr | **155** | 4 Jun | **209** | 28 Jul | **263** | 20 Sep | **317** | 13 Nov | | |
| **48** | 17 Feb | **102** | 12 Apr | **156** | 5 Jun | **210** | 29 Jul | **264** | 21 Sep | **318** | 14 Nov | | |
| **49** | 18 Feb | **103** | 13 Apr | **157** | 6 Jun | **211** | 30 Jul | **265** | 22 Sep | **319** | 15 Nov | | |
| **50** | 19 Feb | **104** | 14 Apr | **158** | 7 Jun | **212** | 31 Jul | **266** | 23 Sep | **320** | 16 Nov | | |
| **51** | 20 Feb | **105** | 15 Apr | **159** | 8 Jun | **213** | 1 Aug | **267** | 24 Sep | **321** | 17 Nov | | |
| **52** | 21 Feb | **106** | 16 Apr | **160** | 9 Jun | **214** | 2 Aug | **268** | 25 Sep | **322** | 18 Nov | | |
| **53** | 22 Feb | **107** | 17 Apr | **161** | 10 Jun | **215** | 3 Aug | **269** | 26 Sep | **323** | 19 Nov | | |
| **54** | 23 Feb | **108** | 18 Apr | **162** | 11 Jun | **216** | 4 Aug | **270** | 27 Sep | **324** | 20 Nov | | |

# References


Baidar, S., Oetjen, H., Coburn, S., Dix, B., Ortega, I., Sinreich, R. and Volkamer, R., 2013: The CU Airborne MAX-DOAS instrument: vertical profiling of aerosol extinction and trace gases, *Atmospheric Measurement Techniques*, 6 (3), 719–739.

Balashov, N. V., Thompson, A. M., Piketh, S. J. and Langerman, K. E., 2014: Surface ozone variability and trends over the South African Highveld from 1990 to 2007, *Journal of Geophysical Research: Atmospheres*, , 2014, 4323–4342.

Beirle, S., (2008), 'Personal communication'.

Beirle, S., Boersma, K. F., Platt, U., Lawrence, M. G. and Wagner, T., 2011: Megacity emissions and lifetimes of nitrogen oxides probed from space., *Science (New York, N.Y.)*, 333 (6050), 1737–9.

Beirle, S., Huntrieser, H. and Wagner, T., 2010: Direct satellite observation of lightning-produced NO¡sub¿x¡/sub¿, *Atmospheric Chemistry and Physics*, 10 (22), 10965–10986.

Boersma, K. F., Eskes, H. J., Dirksen, R. J., van der A, R. J., Veefkind, J. P., Stammes, P., Huijnen, V., Kleipool, Q. L., Sneep, M., Claas, J., Leitão, J., Richter, A., Zhou, Y. and Brunner, D., 2011: An improved tropospheric NO¡sub¿2¡/sub¿ column retrieval algorithm for the Ozone Monitoring Instrument, *Atmospheric Measurement Techniques*, 4 (9), 1905–1928.

Bogumil, K., Orphal, J., Homann, T., Voigt, S., Spietz, P., Fleischmann, O., Vogel, a., Hartmann, M., Kromminga, H., Bovensmann, H., Frerick, J. and Burrows, J., 2003: Measurements of molecular absorption spectra with the SCIAMACHY pre-flight model: instrument characterization and reference data for atmospheric remote-sensing in the 2302380 nm

region, *Journal of Photochemistry and Photobiology A: Chemistry*, 157 (2-3), 167–184.

Bovensmann, H., Burrows, J. P., Buchwitz, M., Frerick, J., Noel, S., Rozanov, V., Chance, K. V. and Goede, A. P. H., 1999: SCIAMACHY : Mission Objectives and Measurement Modes, *Journal of the Atmospheric Sciences*, 56 (2), 127–150.

Bracher, A., Bovensmann, H., Bramstedt, K., Burrows, J., Clarmann, T. V., Eichmann, K.-U., Fischer, H., Funke, B., Gil-López, S., Glatthor, N., Grabowski, U., Höpfner, M., Kaufmann, M., Kellmann, S., Kiefer, M., Koukouli, M., Linden, a., López-Puertas, M., Tsidu, G. M., Milz, M., Noel, S., Rohen, G., Rozanov, a., Rozanov, V., Savigny, C. V., Sinnhuber, M., Skupin, J., Steck, T., Stiller, G., Wang, D.-Y., Weber, M. and Wuttke, M., 2005: Cross comparisons of O3 and NO2 measured by the atmospheric ENVISAT instruments GOMOS, MIPAS, and SCIAMACHY, *Advances in Space Research*, 36 (5), 855–867.

Broccardo, S., Heue, K.-P., Walter, D., Ross, K. E., Piketh, S. J. and Platt, U., 2008: Airborne Imaging DOAS: a Bridge from Satellite to In-Stack Measurements, *International Global Atmospheric Chemistry*, Annecy.

Buchwitz, M., Rozanov, V. V. and Burrows, J. P., 2000: A near-infrared optimized DOAS method for the fast global retrieval of atmospheric CH4, CO, CO2, H20, and N20 total column amounts from SCIAMACHY Envisat-1 nadir radiances, *Journal of Geophysical Research*, 105 (D12), 15231–15245.

Bucsela, E., Celarier, E., Wenig, M., Gleason, J., Veefkind, J. P., Boersma, K. F. and Brinksma, E. J., 2006: Algorithm for NO/sub 2/ vertical column retrieval from the ozone monitoring instrument, *IEEE Transactions on Geoscience and Remote Sensing*, 44 (5), 1245–1258.

Burrows, J. P., Weber, M., Buchwitz, M., Rozanov, V. V., Ladstatter-Weisenmayer, A., Richter, A., DeBeek, R., Hoogen, R., Bramstedt, K., Eichmann, K., Eisinger, M. and Perner, D., 2000: The Global Ozone Monitoring Experiment (GOME): Mission Concept and First Scientific Results, *Journal of the Atmospheric Sciences*, 56 (1), 151–175.

Bussemer, M., (1993): Der Rink-Effekt: Ursachen und Einflus auf die Spektroskopische Messung stratospharisher Spurenstoffe, PhD thesis: University of Heidelberg.

Campbell, J. R., 2003: Micropulse lidar observations of tropospheric aerosols over northeastern South Africa during the ARREX and SAFARI 2000 dry season experiments, *Journal of Geophysical Research*, 108 (D13), 1–19.

Collett, K. S., Piketh, S. J. and Ross, K. E., 2010: An assessment of the atmospheric nitrogen budget on the South African Highveld, *South African Journal of Science*, 106 (5/6), 1–9.

Cosijn, C. and Tyson, P. D., 1996: Stable discontinuities in the atmosphere over south africa, *South African Journal of Science*, 92, 381–386.

Dix, B., (2007): Spectroscopic Measurements of Atmospheric Trace Gases on Long-Distance Flights, PhD thesis: Ruperto-Carola University of Heidelberg, Germany.

Dix, B., Brenninkmeijer, C. A. M., Frieß, U., Wagner, T. and Platt, U., 2009: Airborne multi-axis DOAS measurements of atmospheric trace gases on CARIBIC long-distance flights, *Atmospheric Measurement Techniques*, 2, 639–652.

Duncan, B. N., Yoshida, Y., de Foy, B., Lamsal, L. N., Streets, D. G., Lu, Z., Pickering, K. E. and Krotkov, N. a., 2013: The observed response of Ozone Monitoring Instrument (OMI) NO2 columns to NOx emission controls on power plants in the United States: 20052011, *Atmospheric Environment*, 81 (2), 102–111.

Garstang, M., Tyson, P. D., Swap, R. J., Edwards, M., Kallberg, P. and Lindesay, J. A., 1996: Horizontal and vertical transport of air over southern Africa, *Journal of Geophysical Research*, 101 (D19), 23721–23736.

General, S., Pöhler, D., Sihler, H., Bobrowski, N., Frieß, U., Zielcke, J., Horbanski, M., Shepson, P. B., Stirm, B. H., Simpson, W., Weber, K., Fisher, C. and Platt, U., 2014: The Heidelberg Airborne Imaging DOAS Instrument (HAIDI) a novel imaging DOAS device for 2-D and 3-D imaging of trace gases and aerosols, *Atmospheric Measurement Techniques*, 7, 3459–3485.

Ghude, S. D., Fadnavis, S., Beig, G., Polade, S. D. and van der A, R. J., 2008: Detection of surface emission hot spots, trends, and seasonal cycle from satellite-retrieved NO 2 over India, *Journal of Geophysical Research*, 113 (D20), 1–13.

Ghude, S. D., Lal, D. M., Beig, G., van der A, R. J. and Sable, D., 2010: Rain-Induced Soil NO x Emission From India During the Onset of the Summer Monsoon: A Satellite Perspective, *Journal of Geophysical Research*, 115 (D16), 1–9.

Giglio, L., Csiszar, I. and Justice, C. O., 2006: Global distribution and seasonality of active fires as observed with the Terra and Aqua Moderate Resolution Imaging Spectroradiometer (MODIS) sensors, *Journal of Geophysical Research*, 111 (G2), G02016.

Gottwald, M., Bovensmann, H., Lichtenberg, G., Noel, S., von Bargen, A., Slijkhuis, S., Piters, A., Hoogeveen, R., von Savigny, C. and Buchwitz, M., 2006: *SCIAMACHY, Monitoring the Changing Earth's Atmosphere*, DLR.

Grainger, J. and Ring, J., 1962: Anomalous Fraunhofer line profiles, *Nature*, 193, 762.

Greenblatt, G., Orlando, J., Burkholder, J. and Ravishankara, A. R., 1990: Absorption measurements of Oxygen between 330nm and 1140nm, *Journal of Geophysical Research*, 95, 18577–18582.

Hains, J. C., Boersma, K. F., Kroon, M., Dirksen, R. J., Cohen, R. C., Perring, A. E., Bucsela, E., Volten, H., Swart, D. P. J., Richter, A., Wittrock, F., Schoenhardt, A., Wagner, T., Ibrahim, O. W., van Roozendael, M., Pinardi, G., Gleason, J. F., Veefkind, J. P. and Levelt, P., 2010: Testing and improving OMI DOMINO tropospheric NO 2 using observations from the DANDELIONS and INTEX-B validation campaigns, *Journal of Geophysical Research*, 115 (D5), 1–20.

Herman, J., Cede, A., Spinei, E., Mount, G., Tzortziou, M. and Abuhassan, N., 2009: NO 2 column amounts from ground-based Pandora and MFDOAS spectrometers using the direct-sun DOAS technique: Intercomparisons and application to OMI validation, *Journal of Geophysical Research*, 114 (D13), D13307.

Heue, K., Brenninkmeijer, C. A. M., Baker, A. K., Rauthe-Schöch, A., Walter, D., Wagner, T., Hormann, C., Sihler, H., Dix, B., Frieß, U., Platt, U., Martinsson, B. G., van Velthoven, P. F. J., Zahn, A. and Ebinghaus, R., 2011: SO2 and BrO observation in the plume of the Eyjafjallajokull volcano 201 : CARIBIC and GOME-2 retrievals, *Atmospheric Chemistry and Physics*, 11, 2973–2989.

Heue, K., Brenninkmeijer, C. A. M., Wagner, T., Mies, K., Dix, B., Frieß, U., Martinsson, B. G., Slemr, F. and van Velthoven, P. F. J., 2010: Observations of the 2008 Kasatochi volcanic SO2 plume by CARIBIC aircraft DOAS and the GOME-2 satellite, *Atmospheric Chemistry and Physics*, 10, 4699–4713.

Heue, K.-P., (2005): Airborne Multi Axis DOAS instrument and measurements of two-dimensional tropospheric trace gas distributions, PhD thesis: University of Heidelberg.

Heue, K.-P., Richter, A., Bruns, M., Burrows, J. P., Platt, U., Pundt, I., Wang, P. and Wagner, T., 2005: Validation of SCIAMACHY tropospheric NO 2 -columns with AMAXDOAS measurements, *Atmospheric Chemistry and Physics*, 5, 1039–1051.

Heue, K.-P., Riede, H., Walter, D., Brenninkmeijer, C. a. M., Wagner, T., Frieß, U., Platt, U., Zahn, a., Stratmann, G. and Ziereis, H., 2014: CARIBIC DOAS observations of nitrous acid and formaldehyde in a large convective cloud, *Atmospheric Chemistry and Physics*, 14 (13), 6621–6642.

Heue, K.-P., Wagner, T., Broccardo, S. P., Piketh, S. J., Ross, K. E., Platt, U. and Africa, S., 2006: Direct Observation of Two-Dimensional Trace Gas Distributions with and Airborne Imaging DOAS Instrument, *18th ESA Symposium on European Rocket and Balloon Programs and Related Research*, number 1, European Space Agency.

Heue, K.-P., Wagner, T., Broccardo, S. P., Walter, D., Piketh, S. J., Ross, K. E., Beirle, S. and Platt, U., 2008*a*: Direct observation of two dimensional trace gas distribution with an airborne Imaging DOAS instrument, *Atmospheric Chemistry and Physics Discussions*, 8, 11879–11907.

Heue, K.-P., Wagner, T., Broccardo, S. P., Walter, D., Piketh, S. J., Ross, K. E., Beirle, S. and Platt, U., 2008*b*: Direct observation of two dimensional trace gas distributions with an airborne Imaging DOAS instrument, *Atmospheric Chemistry and Physics*, 8 (22), 6707–6717.

Hilboll, a., Richter, A., Rozanov, a., Hodnebrog, O., Heckel, a., Solberg, S., Stordal, F. and Burrows, J. P., 2013: Improvements to the retrieval of tropospheric NO¡sub¿2¡/sub¿ from satellite stratospheric correction using SCIAMACHY limb/nadir matching and comparison to Oslo CTM2 simulations, *Atmospheric Measurement Techniques*, 6 (3), 565–584.

Jaeglé, L., 2004: Satellite mapping of rain-induced nitric oxide emissions from soils, *Journal of Geophysical Research*, 109 (D21), D21310.

Josipovic, M., Kollonige, D. W., Burger, R. P., Thompson, A. M., Johan, P., Zyl, P. G. V., Venter, A. D., Jaars, K., Martins, D. K. and Laakso, L., 2013: A comparison of surface NO2 mixing ratios and total column observations at a South African site, *IUAPPA*, number 2, Cape Town.

Kazahaya, R., Mori, T., Kazahaya, K. and Hirabayashi, J.-i., 2008: Computed tomography reconstruction of SO 2 concentration distribution in the volcanic plume of Miyakejima, Japan, by airborne traverse technique using three UV spectrometers, *Geophysical Research Letters*, 35 (13), 2–7.

KNMI, (2012), 'Background information about the Row Anomaly in OMI'.

Kraus, S. G., (2006): DOASIS: A framework design for DOAS, PhD thesis: University of Mannheim.

Krotkov, N. A., Carn, S. A., Krueger, A. J., Bhartia, P. K. and Yang, K., 2006: Band Residual Difference Algorithm for Retrieval of SO 2 From the Aura Ozone Monitoring Instrument ( OMI ), *IEEE Transactions on Geoscience and Remote Sensing*, 44 (5), 1259–1266.

Kühl, S., Pukite, J., Deutschmann, T., Platt, U. and Wagner, T., 2008: SCIAMACHY limb measurements of NO2, BrO and OClO. Retrieval of vertical profiles: Algorithm, first results, sensitivity and comparison studies, *Advances in Space Research*, 42 (10), 1747–1764.

Kurucz, R., Furenlid, I., Brault, J. and Testerman, L., (1984): Solar flux atlas from 296 to 1300 nm, Technical report: National Solar Observatory, Sunspot, NM.

Lamsal, L. N., Martin, R. V., van Donkelaar, a., Celarier, E. a., Bucsela, E. J., Boersma, K. F., Dirksen, R., Luo, C. and Wang, Y., 2010: Indirect validation of tropospheric nitrogen dioxide retrieved from the OMI satellite instrument: Insight into the seasonal variation of nitrogen oxides at northern midlatitudes, *Journal of Geophysical Research*, 115 (D5), 1–15.

Leitao, J., Richter, A., Vrekoussis, M., Kokhanovsky, A., Zhang, Q. J., Beekmann, M. and Burrows, J., 2010: On the improvement of NO2 satellite retrievals aerosol impact on the airmass factors, *Atmospheric Measurement Techniques*, 3, 475–493.

Levelt, P. F., Oord, G. H. J. V. D., Dobber, M. R., Mälkki, A., Visser, H., Vries, J. D., Stammes, P., Lundell, J. O. V. and Saari, H., 2006: The Ozone Monitoring Instrument, *IEEE Transactions on Geoscience and Remote Sensing*, 44 (5), 1093–1101.

Levy, R. C., Remer, L. A., Mattoo, S., Kaufman, Y. J. and Systems, S., (2009): Algorithm for Remote Sensing of Tropospheric Aerosol over Dark Targets from MODIS : Collections 005 and 051 : Revision 2 ; Feb 2009, Technical report: NASA.

Lin, J.-T., Martin, R. V., Boersma, K. F., Sneep, M., Stammes, P., Spurr, R., Wang, P., Van Roozendael, M., Clémer, K. and Irie, H., 2014: Retrieving tropospheric nitrogen dioxide from the Ozone Monitoring Instrument: effects of aerosols, surface reflectance anisotropy, and vertical profile of nitrogen dioxide, *Atmospheric Chemistry and Physics*, 14 (3), 1441–1461.

Lourens, A., Butler, T., Beukes, J. P., van Zyl, P. G., Beirle, S., Wagner, T., Heue, K.-P., Pienaar, J. J., Fourie, G. D. and Lawrence, M. G., 2012: Re-evaluating the NO 2 hotspot over the South African Highveld, *South African Journal of Science*, 108 (2), 1–6.

Martin, R. V., 2003: Global inventory of nitrogen oxide emissions constrained by space-based observations of NO 2 columns, *Journal of Geophysical Research*, 108 (D17), 1–12.

Martin, R. V., 2004: Evaluation of GOME satellite measurements of tropospheric NO 2 and HCHO using regional data from aircraft campaigns in the southeastern United States, *Journal of Geophysical Research*, 109 (D24), D24307.

Martin, R. V., 2008: Satellite remote sensing of surface air quality, *Atmospheric Environment*, 42 (34), 7823–7843.

Martin, R. V., Chance, K. V., Jacob, D. J., Kurosu, T. P., Spurr, R. J. D., Bucsela, E. J., Gleason, J. F., Palmer, P. I., Bey, I., Fiore, A. M., Li, Q., Yantosca, R. M. and Koelemeijer, R. B., 2002: An improved retrieval of tropospheric nitrogen dioxide from GOME, *Journal of Geophysical Research*.

Melamed, M. L., Langford, a. O., Daniel, J. S., Portmann, R. W., Miller, H. L., Eubank, C. S., Schofield, R., Holloway, J. and Solomon, S., 2008:

Sulfur dioxide emission flux measurements from point sources using airborne near ultraviolet spectroscopy during the New England Air Quality Study 2004, *Journal of Geophysical Research*, 113 (D2), D02305.

Noël, S., Bovensmann, H., Wuttke, M., Burrows, J., Gottwald, M., Krieg, E., a.P.H. Goede and Muller, C., 2002: Nadir, limb, and occultation measurements with SCIAMACHY, *Advances in Space Research*, 29 (11), 1819–1824.

Piketh, S. J., Swap, R. J., Maenhaut, W., Annegarn, H. J. and Formenti, P., 2002: Chemical evidence of long-range atmospheric transport over southern Africa, *Journal of Geophysical Research*, 107 (D24), 1–13.

Platt, U. and Stutz, J., 2008: *Differential Optical Absorption Spectroscopy*, 1st edn, Springer-Verlag, Berlin, Heidelberg.

Rawlings, J. B. and Ekerdt, J. G., 2002: *Chemical Reactor Analysis and Design Fundamentals*, Nob Hill Publishing, Madison, Wisconsin.

Richter, A., (2008), 'Personal communication'.

Richter, A. and Burrows, J., 2002: Tropospheric NO2 from GOME measurements, *Advances in Space Research*, 29 (11), 1673–1683.

Richter, A., Burrows, J. P., Nüss, H., Granier, C. and Niemeier, U., 2005: Increase in tropospheric nitrogen dioxide over China observed from space., *Nature*, 437 (7055), 129–32.

Rothman, L., Rinsland, C., Goldman, a., Massie, S., Edwards, D., Flaud, J.-M., Perrin, a., Camy-Peyret, C., Dana, V., Mandin, J.-Y., Schroeder, J., Mccann, a., Gamache, R., Wattson, R., Yoshino, K., Chance, K., Jucks, K., Brown, L., Nemtchinov, V. and Varanasi, P., 1998: the Hitran Molecular Spectroscopic Database and Hawks (Hitran Atmospheric Workstation): 1996 Edition, *Journal of Quantitative Spectroscopy and Radiative Transfer*, 60 (5), 665–710.

Rozanov, a., Rozanov, V., Buchwitz, M., Kokhanovsky, a. and Burrows, J., 2005: SCIATRAN 2.0 A new radiative transfer model for geophysical applications in the 1752400nm spectral region, *Advances in Space Research*, 36 (5), 1015–1019.

Sayer, A. M., Smirnov, A., Hsu, N. C., Munchak, L. A. and Holben, B. N., 2012: Estimating marine aerosol particle volume and number from Maritime Aerosol Network data, *Atmospheric Chemistry and Physics*, 12 (18), 8889–8909.

Schaub, D., Brunner, D., Boersma, K. F., Keller, J., Folini, D., Buchmann, B., Berresheim, H. and Staehelin, J., 2007: SCIAMACHY tropospheric NO2 over Switzerland : estimates of NOx lifetimes and impact of the complex Alpine topography on the retrieval, *Atmospheric Chemistry and PhysicsAtmospheric Chemistry and Physics*, 7, 5971–5987.

Schneider, P., Lahoz, W. A. and van der A, R. J., 2015: Recent satellite-based trends of tropospheric nitrogen dioxide over large urban agglomerations worldwide, *Atmospheric Chemistry and Physics*, 15 (2), 1205–1220.

Schumann, U., 2012: *Atmospheric Physics*, Springer, Berlin, Heidelberg.

Seinfeld, J. H. and Pandis, S. N., 2006: *Atmospheric Chemistry and Physics*, 2nd edn, John Wiley and Sons.

Sioris, C., Kurosu, T. P., Martin, R. V. and Chance, K., 2004: Stratospheric and tropospheric NO2 observed by SCIAMACHY: first results, *Advances in Space Research*, 34 (4), 780–785.

Spicer, C. W., 1982: Nitrogen oxide reactions in the urban plume of Boston., *Science (New York, N.Y.)*, 215 (4536), 1095–7.

Spichtinger, N., Wenig, M., James, P., Wagner, T., Platt, U. and Stohl, A., 2001: Satellite detection of a continental-scale plume of nitrogen oxides from boreal forest fires, *Geophysical Research Letters*, 28 (24), 4579–4582.

Stohl, a., Huntrieser, H., Richter, A., Beirle, S., Cooper, O. R., Eckhardt, S., Forster, C., James, P., Spichtinger, N., Wenig, M., Wagner, T., Burrows, J. P. and Platt, U., 2003: Rapid intercontinental air pollution transport associated with a meteorological bomb, *Atmospheric Chemistry and Physics*, 3 (4), 969–985.

Swap, R. J. and Tyson, P. D., 1999: Stable discontinuities as determinants of the vertical distribution of aerosols and trace gases in the atmosphere, *South African Journal of Science*, 95, 63–71.

Thomas, G. E. and Stamnes, K., 1999: *Radiative Transfer in the Atmosphere and Ocean*, Cambridge University Press.

Toenges-Schuller, N., Stein, O., Rohrer, F., Wahner, a., Richter, A., Burrows, J. P., Beirle, S., Wagner, T., Platt, U. and Elvidge, C. D., 2006: Global distribution pattern of anthropogenic nitrogen oxide emissions: Correlation analysis of satellite measurements and model calculations, *Journal of Geophysical Research*, 111 (D5), D05312.

Tyson, P. D. and DAbreton, P., 1998: Transport and recirculation of aerosols off Southern Africamacroscale plume structure, *Atmospheric Environment*, 32 (9), 1511–1524.

Tyson, P. D., Garstang, M., Swap, R. J., Kallberg, P. and Edwards, M., 1996: An Air Transport Climatology for Subtropical Southern Africa, *International Journal of Climatology*, 16, 265–291.

van der A, R. J., Eskes, H. J., Boersma, K. F., van Noije, T. P. C., Van Roozendael, M., De Smedt, I., Peters, D. H. M. U. and Meijer, E. W., 2008: Trends, seasonal variability and dominant NO x source derived from a ten year record of NO 2 measured from space, *Journal of Geophysical Research*, 113 (D4), 1–12.

van der A, R. J., Peters, D. H. M. U., Eskes, H., Boersma, K. F., Van Roozendael, M., De Smedt, I. and Kelder, H. M., 2006: Detection of the trend and seasonal variation in tropospheric NO 2 over China, *Journal of Geophysical Research*, 111 (D12), 1–10.

Vandaele, A. C., Hermans, C., Simon, P. C., Carleer, M., Colin, R., Fally, S., Merienne, M. F., Jenouvrier, A. and Coquart, B., 1998: MEASUREMENTS OF THE NO2 ABSORPTION CROSS-SECTION FROM 42 000 cm-1 TO 10 000 cm-1 ( 238-1000 nm) AT 220 K AND 294 K, *Journal of Quantitative Spectroscopy and Radiative Transfer*, 59 (3-5), 171–184.

Veefkind, J. P., Aben, I., McMullan, K., Förster, H., de Vries, J., Otter, G., Claas, J., Eskes, H., de Haan, J., Kleipool, Q., van Weele, M., Hasekamp, O., Hoogeveen, R., Landgraf, J., Snel, R., Tol, P., Ingmann, P., Voors, R., Kruizinga, B., Vink, R., Visser, H. and Levelt, P., 2012: TROPOMI on the ESA Sentinel-5 Precursor: A GMES mission for global observations of the atmospheric composition for climate, air quality and ozone layer applications, *Remote Sensing of Environment*, 120, 70–83.

Vountas, M., Rozanov, V. and Burrows, J., 1998: Ring Effect: Impact of Rotational Raman Scattering on Radiative Transfer in EarthS Atmosphere, *Journal of Quantitative Spectroscopy and Radiative Transfer*, 60 (6), 943–961.

Weatherhead, E. C., Reinsel, G. C., Tiao, G. C., Meng, X.-l., Choi, D., Cheang, W.-k., Keller, T., DeLuisi, J., Wuebbles, D. J., Kerr, J. B., Miller, A. J., Oltmans, S. J. and Frederick, J. E., 1998: Factors affecting the detection of trends : Statistical considerations and applications to

environmental data, *Journal of Geophysical Research*, 103 (D14), 17149–17161.

Wenig, M., Spichtinger, N., Stohl, a., Held, G., Beirle, S., Wagner, T., Jähne, B. and Platt, U., 2003: Intercontinental transport of nitrogen oxide pollution plumes, *Atmospheric Chemistry and Physics*, 3 (2), 387–393.

Zien, A. W., Richter, A., Hilboll, A., Blechschmidt, A. and Burrows, J. P., 2014: Systematic analysis of tropospheric NO 2 long-range transport events detected in GOME-2 satellite data, *Atmospheric Chemistry and Physics*, 14, 7367–7396.